Load Sharing Mechanism of Micropiled-Raft Foundations in Sand

Farhad Nabizadeh

A Thesis

In the Department

of

Building, Civil, and Environmental Engineering

Presented in Partial Fulfilment of the Requirements

For the Degree of

Doctor of Philosophy (Civil Engineering) at

Concordia University

Montreal, Quebec, Canada

May 2023

CONCORDIA UNIVERSITY

SCHOOL OF GRADUATE STUDIES

This is to certify that the thesis prepared

By: Farhad Nabizadeh

Entitled: Load Sharing Mechanism of Micropiled-Raft foundations in Sand

and submitted in partial fulfillment of the requirements for the degree of

Doctor Of Philosophy (Civil Engineering)

complies with the regulations of the University and meets the accepted standards with respect to originality and quality.

Signed by the final examining committee:

______________________________ Chair
Dr. Ahmed Kishk

______________________________ External Examiner
Dr. Mohamed Meguid

______________________________ Examiner
Dr. Attila Zsaki

______________________________ Examiner
Dr. Gerard Gouw

______________________________ Examiner
Dr. Biao Li

______________________________ Thesis Supervisor
Dr. Adel Hanna

Approved by ______________________________
Dr. Mazdak Nik-Bakht, Graduate Program Director

5/3/2023 ______________________________
Dr. Mourad Debbabi, Dean
Gina Cody School of Engineering and Computer Science

Abstract

Load-sharing mechanism of Micropiled raft foundations in sand

Farhad Nabizadeh
Concordia University,2023

Micropiled-Raft (MPR) foundations are economical and easy to install. In this study, the load-sharing mechanism of micropiled-raft foundations in sand was examined. A series of experimental tests were performed on small-scale models in sand with different relative densities. The effects of micropile spacing and relative density of the sand on the overall load-settlement behavior and the load-sharing mechanism were examined.

The experimental test results served to validate a series of numerical models, which were employed to produce data for a wide range of governing parameters. The effects of the micropile spacing ratio, the relative density of the sand, and the thickness of the raft were examined. While the raft stiffness only marginally affects the overall load-settlement behavior, yet, the load sharing is impacted.

Finally, the Poulos-Davis-Randolph (PDR) method was evaluated against the data produced by the numerical models. It was concluded that the PDR method was occasionally capable of determining the axial stiffness of the MPR with an acceptable range of error, however in general, it overestimated the axial stiffness of the MPRs. Thus, a modification factor was proposed which was validated by the present experimental results.

ACKNOWLEDGEMENTS

First and foremost, I would like to praise and thank God, the Almighty, who has granted immeasurable blessing, knowledge, and opportunity to the writer, so that I have been finally able to accomplish the thesis.

As my thesis supervisor, I would like to express my deepest gratitude to Dr. Adel Hanna. He has been a tremendous support and help to me, and I cannot thank him enough. The success of this dissertation would have never been possible without his vast knowledge, great experience, and remarkable visions. I am thankful to the technical staff at Concordia University, including Mr. Luc Demers, and Mr. Mark Elie, for the technical assistance.

I would like to thank my wife (Samila) and son (Sam) who supported me and provided me with a calm and pleasant environment during my study. I would also like to extend my deepest gratitude to my mother, Parivash, for her emotional and financial support during my studies.

To My Family

& To the Soul of my Beloved Father

Hadi

Table of Contents

List of Figures

List of tables

List of Symbols

- Br = *Breath of raft*
- C_c = *Coefficient of curvature*
- C_{ps} = *Coefficient of pile spacing*
- C_u = *Coefficient of uniformity*
- d = *Pile diameter*
- DAS = *Data acquisition system*
- D_r = *Relative density*
- e = *Void ratio*
- E = *Modulus of elasticity*
- e_{max} = *Maximum void ratio*
- e_{min} = *Minimum void ratio*
- E_r = *Elastic modulus of raft*
- E_S = *Elastic modulus of soil*
- FE = *Finite Elements*
- G = *Shear modulus*
- G_S = *Specific gravity of soil solids*
- K_p = *Stiffness of pile group*
- K_{pr} = *Stiffness of piled raft*
- K_r = *Stiffness of raft*
- K_{rs} = *Raft-soil stiffness ratio*
- L = *Pile length*
- L_r = *Length of raft*
- LVDT = *Linear vertical displacement transducer*
- M = *Pile installation method coefficient*
- OCR = *Over consolidation ratio*
- OD = *Outer diameter*
- PDR = *Poulos-Davis-Randolph Method*
- P_p = *Ultimate capacity of piles in a piled raft footing*
- R = *Raft (shallow footing)*
- r_m = *Influence radius of pile*
- S = *Pile spacing*
- tr = *Thickness of raft*
- USCS = *Unified soil classification system*
- VEE = *Visual engineering environment*
- W = Settlement (displacement)
- W_P = Settlement of pile
- W_R = *Settlement of raft*
- W_{PR} = *Settlement of piled raft*
- X = *Raft share in a piled raft foundation*
- α_{rp} = *Pile-raft interaction factor proposed by Randolph (1983)*
- γ = *Shear strain*
- γ_{max} = *Maximum dry unit weight*
- γ_{min} = *Minimum dry unit weight*
- δ = *Friction angle between soil particles and sand paper*
- ε= *Normal strain*
- ν_r = *Poisson ratio of raft*
- ν_s = *Poisson ratio of soil*
- η_{PG} = *Pile group efficiency*
- σ= *Normal stress*
- τ = *Shear stress*
- ϕ = *Soil friction angle*
- 2D = *Two dimensional*
- 3D = *Three dimensional*

CHAPTER 1. INTRODUCTION

1.1.General

Pile raft foundations are built by combining the piles with a raft. Piles help the raft to carry larger loads under smaller settlements. Piled foundations are described as such by Atkinson (2007) when their depth exceeds their breadth by three times.

Recently, in some projects depending on the condition, the designers substitute the conventional piles with micropiles. Known also as Minipiles, pin piles, needle piles, and root piles, micropiles are a deep foundation element constructed of the small-diameter pile. There has been rapid growth in the application of micropiles since the mid-1980s in the United States (Bruce et al., 1997).

The concept of MPR systems is similar to piled rafts, which are composite structures consisting of three components: soil, raft, and piles. There are three types of soil-structure interactions in this system, i.e., pile-soil, pile-soil-pile, and raft-soil interaction (Fig. 1.1). These interactions have been studied by researchers. Yet, these researches were mainly focused on the piled-raft foundations with conventional piles which behave differently from micropiles. Micropiles, unlike traditional piles, heavily rely on their skin friction to provide the bearing mechanism, and their slenderness ratio is larger.

Among the researchers, perhaps the most practical design approach belongs to Poulos (2001). This approach, known as PDR, is a combination of three different studies by Poulos himself, Davis, and Randolph. PDR can estimate the axial stiffness of a piled-raft foundation by considering the stiffness of the component elements namely piles and rafts. Axial stiffness will enable the designers to roughly predict the load-settlement behavior of the foundation for preliminary design purposes. However, since the PDR method has originally been intended for piled-raft foundations the different behavior of micropile due to the higher skin frictions and smaller dimensions needs to be evaluated and verified.

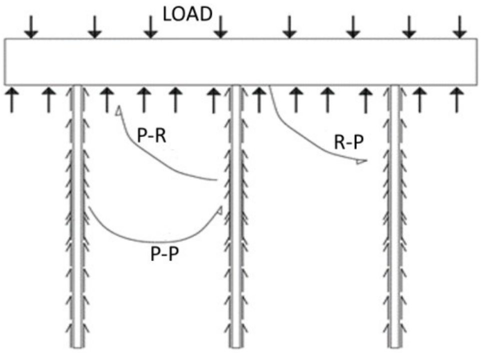

Fig. 1.1-Interaction between the MPR elements

1.2.History of micropiles

The history of micropiles goes back to the 1950s. Dr. Fernando Lizzi, who was a civil engineer with a specialty in foundation repair works, had a great role in the introduction of micropiles to the world. As a result of his efforts, micropiles started being used for the underpinning of damaged historical structures in WWII (Fig. 1.2). However, this technology did not get the recognition it deserved until the 1970s, when Americans started using it as a helpful and economical solution, especially in retrofitting projects. In 1980 FHWA published early design manuals of micropiles after extensive research. Later in the 1990s, the Intermodal Surface Transportation Efficiency Act (ISTEA) provided funding for the rehabilitation of highways which paved the way for micropiles. In the 2000s, the International Building Code and the AASHTO Bridge Design Specifications introduced design code sections for micropiles. All these developments helped micropile technology to be accepted in the construction industry.

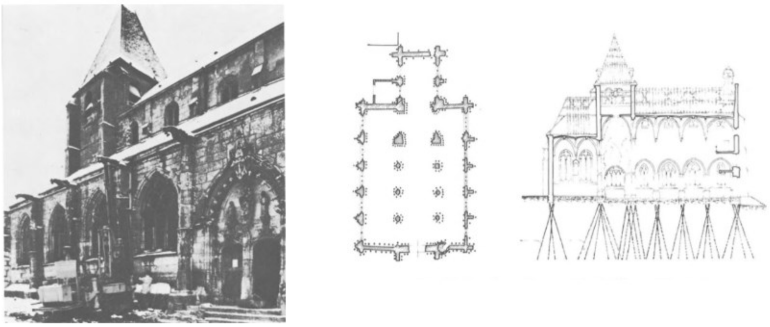

Fig. 1.2-Structure retrofitted by Lizzi; The Monumental Church of Tourney. This historic building required underpinning due to the differential settling of the foundation. (Thorburn and Littlejohn, Pg.93)

Piled-raft foundations, a raft supported on piles, emerged in the 1950s. Torre Latino Americana in Mexico City was built on a piled raft foundation. Later, the introduction of micropiles in the 1970s encouraged the designer to consider using micropiles instead of piles for supporting the rafts. However, because micropiled-rafts are not well-known to engineers, few projects have been built using them (Fig. 1.3).

Fig. 1.3-Torre Latino-Americana Mexico City (Wikipedia,2022)

1.3.Purpose of this study

In this study, the main objective is to investigate the load-settlement behavior of micropiled-raft foundations and the load-sharing mechanism between their components. The effects of soil density, micropile spacings, raft stiffness (function of the thickness) on piled raft load-settlement behavior, and load-sharing mechanism between piles and rafts in non-cohesive soil will be examined. Moreover, the accuracy of the PDR (Polous, Randolph, Davis,2001) method will be investigated.

1.4.Thesis outline

This thesis consists of the following chapters:

1. Chapter 2 covers the literature available on various subjects including piled rafts, micropiles, and micropiled-rafts. Some of the previous studies on piled rafts and micropiles along with MPRs are reviewed. Available design methods and design recommendations by FHWA (2009) are also explained.
2. Chapter 3 describes the experimental program, including the experimental setup, and instruments used for measuring loads and settlement
3. Chapter 4 introduces the results of the tests conducted, with emphasis on the effects of soil relative densities, raft stiffness, and micropile spacing on the behavior of micropiled-rafts.
4. In chapter 5, detailed 3D FEM models were developed, including the geometry, boundary conditions, meshing elements, as well as adjustment factors.
5. In Chapter 6, the results of the parametric study of the numerical model were presented, in the form of load-settlement curves. The load-sharing mechanism, reduction in the overall settlement, differential settlement, contact pressure, micropiles skin friction, and bending moment underneath the rafts were presented and examined.
6. In chapter 7, an analysis of the parametric study is presented to evaluate the PDR method for estimating the axial stiffness of the MPR foundations. A correction factor is proposed to modify the axial stiffness proposed in the PDR method. Also, formulas were suggested to determine the load-sharing proportions for each element in a MPR foundation.
7. Chapter 8 covers the conclusion and recommendations for future work.

CHAPTER 2. LITERATURE REVIEW

2.1.General

Micropiles are smaller versions of piles (D<15cm) that have been used in the construction industry for many years. Micropiles transfer the structural load through unsuitable soil layers to suitable load-bearing layers. They first appeared in the 1950s. Lizzi (1950) was the first engineer who utilized them to repair damaged Italian structures during WWII. The main advantage was that the small size of the equipment allowed easy underpinning of pre-existing foundations even in limited access situations (Bruce, et al., 1995)The main load-transferring function of micropiles is through the shaft resistance. The end bearing capacity is not taken into account due to the small diameter of micropiles making this value negligible compared to the shaft resistance.

Micropiles are used in a variety of applications: (1) to serve as the main foundation system for static and dynamic loading; (2) to upgrade an existing foundation system; and (3) to stabilize slopes and reinforce the soil by improving the shearing resistance of soils (Bruce, et al., 1995).

The benefits of using micropiles over traditional piles are: 1) minimal noise and vibration 2) minimal spoil 3) installation in confined spaces 4) lightweight machinery for installation 5) reduced needed overall length because of higher skin fiction produced by grouting 6) higher production rates 7) and ability to work in compression and tension.

2.2.Construction of micropiles

A. Types of micropiles

Micropiles are mainly built by the cast-in-place method, where a hole is bored to accommodate the prefabricated micropile. Recent developments have led to the development of micropiles as a faster alternative where digging holes isn't possible due to soil type, such as sand. Micropiles' primary purpose is for retrofitting projects with insufficient headroom to install conventional piles or when those piles will damage the building due to vibration or their larger dimensions. They appeared in the '60s in Italy. Italy had suffered from World War II, and the structures needed huge amounts of repairs. Conventional piles were not suitable due to their larger sizes and the importance of the ancient building, which required more attention in terms of allowable vibrations.

Classification of micropiles, as suggested by FHWA, is based on the type of the design applications or based on the method of grouting. Type *A* refers to micropiles that are placed under gravity load, and no additional load is applied. Normal grouts are poured around the micropile after the placement, but no pressure is employed, and the grout flows just under its weight. Type *B* is those where neat cement grout is placed into the hole under pressure as the temporary drill casing is drawn back. The variety of injection pressure typically ranges from 0.5 to 1 MPa, which prevents hydrofracturing from happening.

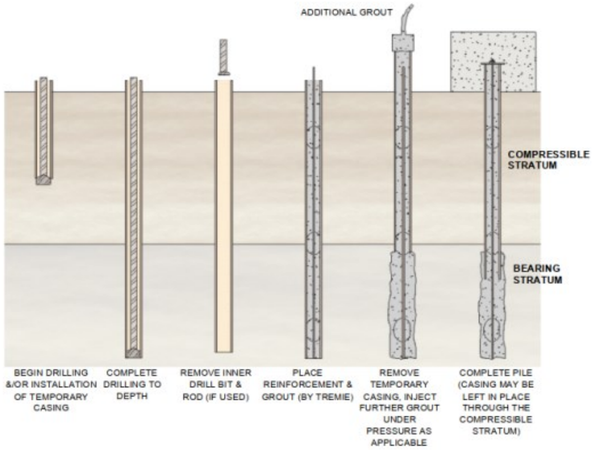

Fig. 2.1--Micropile construction sequence (FHWA,2005)

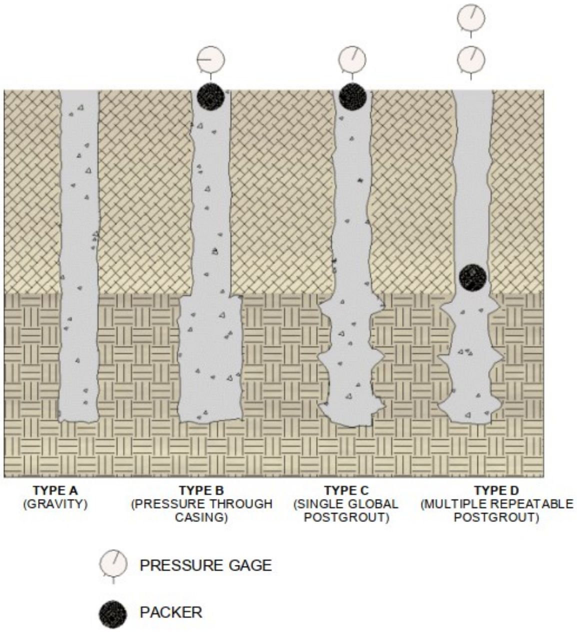

Fig. 2.2- Micropile classification (FHWA,2005)

The third type, C, which appears to be common in France, only has a two-step grouting procedure. In the first step, similar to Type A, under the gravity head, the first part of the grout is poured, and then before it gets hardened, the second step takes place in which, with a pressure of at least 1 MPa, the second grout is injected (no packer is used). Type D micropiles resemble type C with a minor difference in the applied injection pressure which is higher and usually between 2 to 8 MPa (Bruce, et al., 1997) .

Another classification method is based on the function that a micropile will provide after installation. Case 1 micropile elements are to be loaded directly on the pile head, but Case 2, sometimes called reticulated micropiles, denote micropiles that circumscribe and reinforce the soil internally, turning it into a reinforced mass that will take the loads.

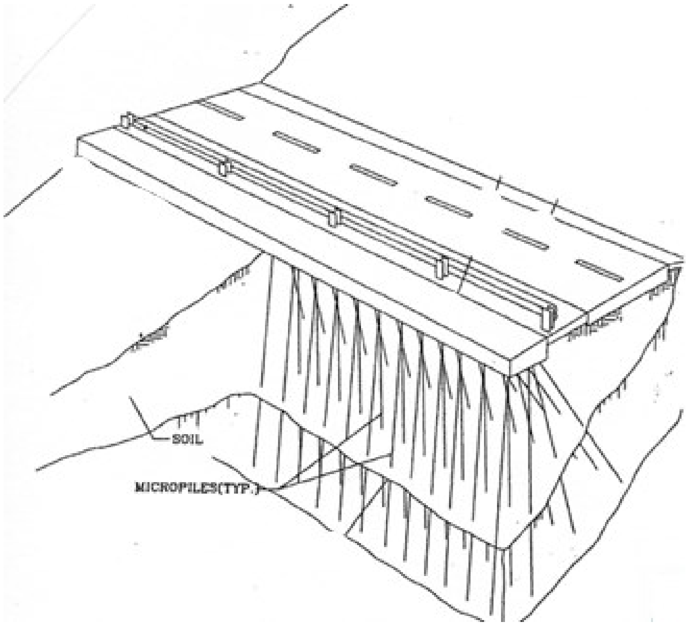

Fig. 2.3-Reticulated micropiles (https://sjc.ac.in/,2021)

B. Designing micropiles

FHWA (2005) covers two design aspects, i.e., geotechnical and structural design. In the geotechnical capacity design of micropiles, due to the small size, the tip-bearing capacity is neglected. The main load-bearing element is, therefore, skin resistance. FHWA (2005) explains that the allowable geotechnical capacity PG-allow is dominated by the bond strength between grout and ground (Equation 2.1).

$$P_{G-allow} = \frac{\alpha_{bond}.\pi.D_b.L_b}{SF}$$

Equation 2.1

Here:

- *L_b represents the bond length*
- *D_b is the diameter of the drilled hole*
- *α_{bond} is the grout-to-ground bonding strength (Values of α_{bond} have been given in the FHWA manual (2005) (*Table 2.1*).*

If micropiles are to serve in a group, their bearing capacity under axial loading follows the same pattern as pile groups, where a factor called *group efficiency factor* determines the overall bearing capacities of the micropiles all combined. If the micropiles are placed at a distance greater than 3d, then the capacity will be the sum of their individual capacities. However, if the distance is smaller because of the interaction between the closely spaced micropiles the capacity factor is less than unity (FHWA, 2005).

The structural design of micropiles has also been explained in FHWA, and apart from the regulations defining the needed spacing between micropiles; selection of micropiles length; selection of micropile cross-section, and selection of micropile type; the main expression for the bearing capacity has been given as follows (Equation 2.2):

$$P_{c-allowable} = [0.4f_c' \times A_c + 0.47 \times F_{y-steel}(A_{bar} + A_{\text{casing}})]$$

Equation 2.2

$P_{c\text{-}allowable}$ = allowable compression load;
f'_c = unconfined compressive strength of grout (typically a 28-day strength);
A_{grout} = area of grout in micropile cross section (inside casing only, discount grout outside the casing);
$F_{y\text{-}steel}$ = yield stress of steel;
A_{bar} = cross-sectional area of steel reinforcing bar (if used); and
A_{casing} = cross-sectional area of steel casing.

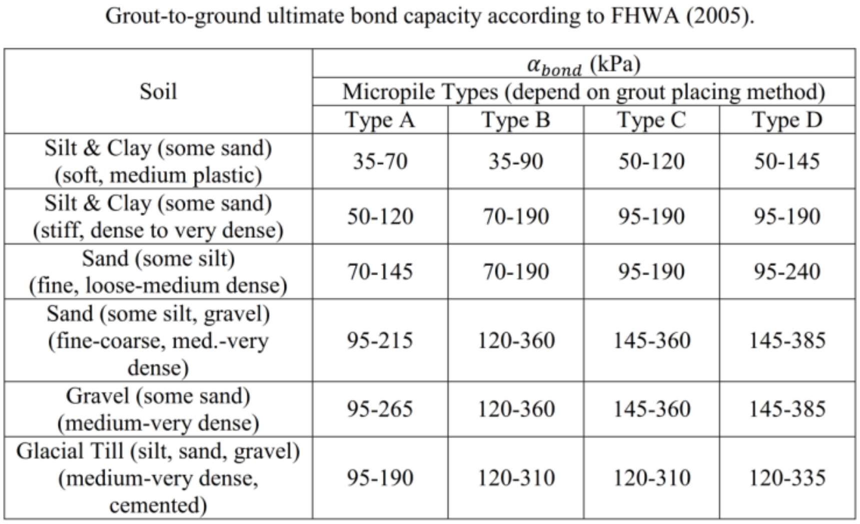

Grout-to-ground ultimate bond capacity according to FHWA (2005).

Soil	α_{bond} (kPa)			
	Micropile Types (depend on grout placing method)			
	Type A	Type B	Type C	Type D
Silt & Clay (some sand) (soft, medium plastic)	35-70	35-90	50-120	50-145
Silt & Clay (some sand) (stiff, dense to very dense)	50-120	70-190	95-190	95-190
Sand (some silt) (fine, loose-medium dense)	70-145	70-190	95-190	95-240
Sand (some silt, gravel) (fine-coarse, med.-very dense)	95-215	120-360	145-360	145-385
Gravel (some sand) (medium-very dense)	95-265	120-360	145-360	145-385
Glacial Till (silt, sand, gravel) (medium-very dense, cemented)	95-190	120-310	120-310	120-335

Table 2.1- Grout to ground ultimate bond capacity (FHWA,2005)

2.3. Previous Researches

In a piled raft, piles are connected to the raft/mat foundation instead of isolated pile caps. Piles stiffen the raft and control the amount of settlement that may occur in the form of total and differential settlement. When piles are placed in compressible soil, there would be a gradual transfer of the total load to the raft and a reduction in the load carried by the piles. The soil beneath the raft then gets compressed, causing a partial load transfer back to the piles. This process continuously occurs until a balanced condition appears (Rao, 2011).

Because of this changing load transfer, the two main elements, piles, and rafts are often designed so that piles can carry the whole loading, while the raft is designed to carry a portion of the total load due to the subsequent load transfer process. The main parameters influencing the behavior of a piled raft are listed below as presented by (Clancy, et al., 1996).

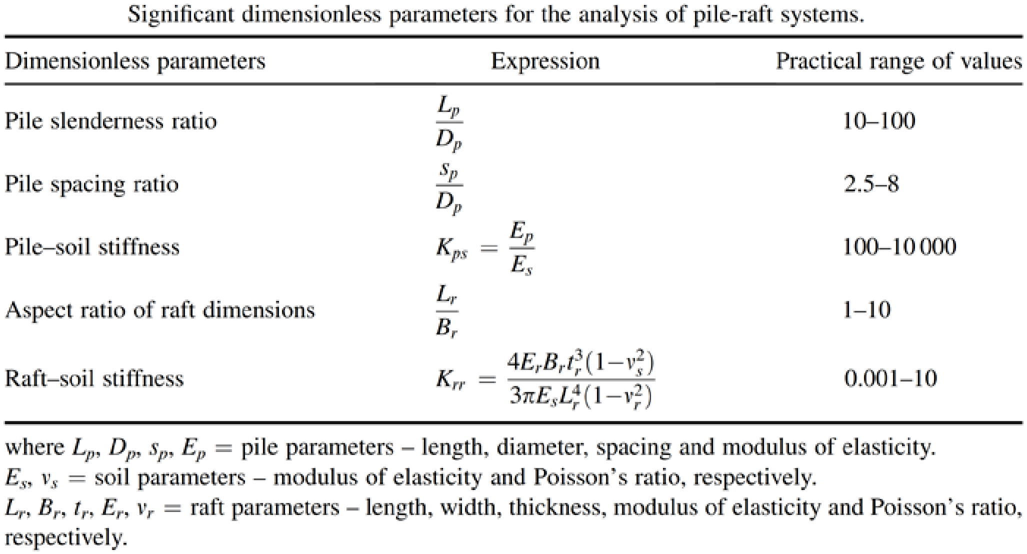

Significant dimensionless parameters for the analysis of pile-raft systems.

Dimensionless parameters	Expression	Practical range of values
Pile slenderness ratio	$\frac{L_p}{D_p}$	10–100
Pile spacing ratio	$\frac{s_p}{D_p}$	2.5–8
Pile–soil stiffness	$K_{ps} = \frac{E_p}{E_s}$	100–10 000
Aspect ratio of raft dimensions	$\frac{L_r}{B_r}$	1–10
Raft–soil stiffness	$K_{rr} = \frac{4E_r B_r t_r^3 (1-\nu_s^2)}{3\pi E_s L_r^4 (1-\nu_r^2)}$	0.001–10

where L_p, D_p, s_p, E_p = pile parameters – length, diameter, spacing and modulus of elasticity.
E_s, ν_s = soil parameters – modulus of elasticity and Poisson's ratio, respectively.
L_r, B_r, t_r, E_r, ν_r = raft parameters – length, width, thickness, modulus of elasticity and Poisson's ratio, respectively.

Table 2.2-Dimensionless parameters for the analysis of pile-raft systems

There are three different design approaches for analyzing piled rafts. Randolph defined them as follows (Randolph, 1994):

- The "conventional approach," in which the piles are designed as a group to carry the major part of the load while making some allowance for the contribution of the raft, primarily to ultimate load capacity.
- "Creep piling," in which the piles are designed to operate at a working load at which significant creep starts to occur at the pile-soil interface, typically at 70-80% of the ultimate load capacity.
- Differential settlement control, in which the piles are located at specific points only to reduce the differential settlement

Based on the time and the technical requirements of a project, one can decide on the required accuracy of the calculations and then either perform a preliminary design or use a detailed design. Preliminary design can be done based on the vertical loading, lateral loading, moment loading, and load-settlement behavior of the system. Detailed design is mainly done by the application of computer-based analysis. These analyses are conducted via rigorous methods or methods in which some of the elements of the system have been simplified (Hemsley, 1999).

A. Simplified Methods (Analytical)

According to Deka (2014), Simplified methods include those of Poulos and Davis, Randolph, Burland, Hemsley, and Poulos. All methods involve several simplifying assumptions (Ripunjoy, 2014). Here, the aim is to provide the designer with simple and practical calculations which can meet the requirements yet with acceptable accuracy. These approaches are to be performed manually without complicated modeling and computers.

1. Davis and Poulos Method (1972):

Their study initially aimed to determine the required number of piles needed to eliminate the excessive settlement of a raft with a desirable safety factor against failure (Bearing capacity is assumed to be sufficient). The authors based their calculations on the assumption that a single pile equipped with a pile cap is located in the distance "S" from another pile with the same specifications and they are under point loads. Also, they assumed that both pile and the cap are rigid and the soil is an ideal elastic semi-infinite mass.

Each pile is divided into "n" cylinders of length δ =L/n. A uniform shear force acts around the surface of these elements and on the circular base (tip). Pile caps are also divided into donut-shaped elements (ν elements). According to the authors, the following expression can be used to determine the soil displacement at the midpoint of any given element "i."

$$\rho_i = \frac{d}{E_s}(\sum_{j=1}^{n}(I_{ij} + I_{ij})p_J + p_b(I_{ib} + I_{ib}) + \sum_{k=1}^{n} p_{ck}(I_{ik} + I_{ik})$$

Equation 2.3

The factors identified as "I" in the equation are influence factors for vertical displacements at the different elements (piles and raft) due to either shear stress or vertical stress being applied in the soil body or on the surface. These influence factors are obtained by double integration of the Mindlin equation. However, for the last term in Equation 2.3, the Boussinesq equation must be used as it applies to the situations where a surface point loading has caused the vertical displacement, which needs to be calculated.

It is allowed to equate the soil displacements to the uniform displacement of the piles. Doing that enables us to obtain (n+ν+1) equations which, along with the vertical equilibrium equations, can be solved. The authors then defined an interaction factor to facilitate the analysis.

$$\alpha_r = \frac{\mathit{additional}\text{ settlement due to an adjacent unit}}{\text{settlement of a single unit}}$$

Equation 2.4

When used in conjunction with the curves relating α_r to dimensionless s/d (spacing to diameter) and values of d_c/d, we can see that interaction increases as d_c/d increases, but for larger L/d the d_c/d becomes smaller.

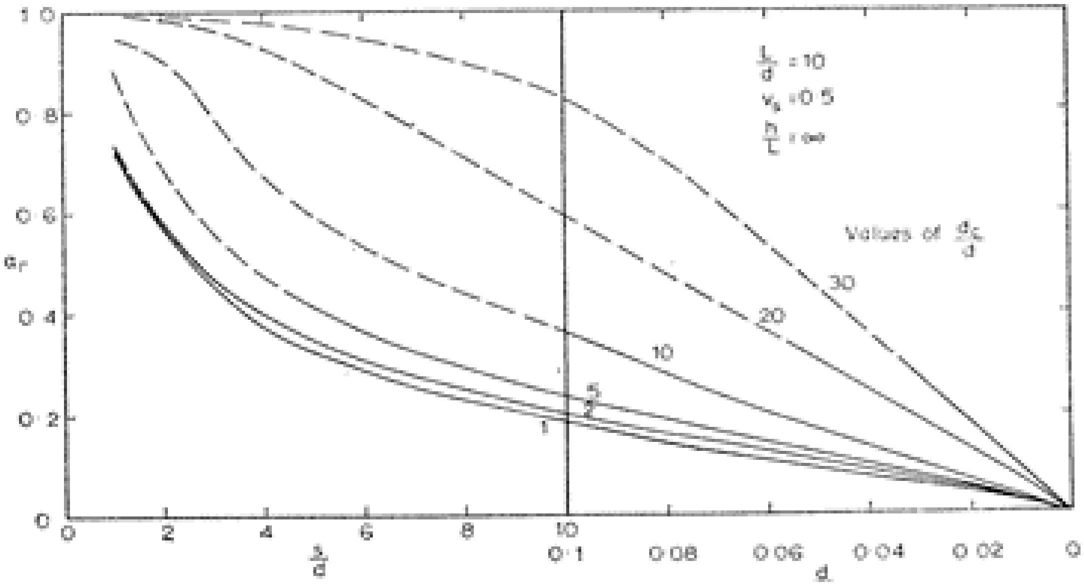

Fig. 2.4-Interaction Factor_ Davis and Poulos (72)

The authors stated that generalization of the above calculation would be logical, so a piled-raft system can be assumed to consist of several pile-cap units, each having an equivalent value of d_c/d, so the area occupied by a unit is the same as that occupied by a typical portion of the cap. The following formula is used for calculating the settlement of a typical unit "i":

$$p_i = p_1\Big(\sum_{\substack{j=1 \\ j\neq i}}^{m} Pj\alpha_{rij} + P_i\Big)$$

Equation 2.5

Where $\bar{\rho}_1$ *can be expressed as* $(\alpha_{rij}=\alpha_r)$

$$\bar{\rho}_1 = F_R . \rho_1$$

(Equation 2.6)

ρ1 is the settlement of a free-standing pile under unit load, and F_R is the ratio of settlement of pile-cap units to the settlement of a free-standing pile. The preceding equation (Equation 2.5)can provide "m" equations for the k piles which together with the equilibrium equation, $P_g=\sum p_j$ are to be solved for two limiting cases of 1) equal displacement of each unit (corresponding to a rigid raft) and 2) equal load in each unit, the final result can be simplified as a settlement ratio of Rs:

$$R_s = \frac{\text{Settlement of system}}{Settlement \text{ of single pile carrying the same average load}}$$

Equation 2.7

And the settlement of the pile-raft foundation is given by:

$$S = R_s \frac{P_G}{m} \rho_1$$

Equation 2.8

For immediate settlements, ρ_1 is the immediate settlement per unit load, of a single pile, and for total final settlements, ρ_1 is the corresponding total final settlement per unit load. ('*m*' is the quantity of the pile cap units.

2. Poulos / PDR Method (2001):

In 2001 *Poulos,* in another paper, summarized solutions from other authors into a single paper combining those solutions into a three-step method to analyze and design a piled raft.

The *first stage* involves a preliminary approximate solution. For assessing vertical bearing capacity, the ultimate load capacity can generally be taken as the lesser of the following two values: (a) the sum of the ultimate capacities of the raft plus all the piles (b) the ultimate capacity of a block containing the piles and the raft, plus that of the portion of the raft outside the margin of the piles. To estimate the load-settlement behavior, one can use *Randolph's* simplified approach and compute the overall stiffness of the piled raft from:

$$K_{pr} = \frac{K_{PG} + k_r(1 - \alpha_{rp})}{1 - \alpha_{rp}^2 K_{\mathrm{r}} K_{PG}}$$

Equation 2.9

Where

K_{pr} = stiffness of piled raft;
K_{PG} = stiffness of the pile group;
K_r = stiffness of the raft alone
α_{rp} = raft – pile interaction factor

The proportion of the load carried by the raft to the total load applied is given as a factor termed "X" and is calculated by the following expression (α_{cp} has been used in the original paper instead of α_{rp}):

$$P_r/P_t = K_r(1 - \alpha_{cp})/K_p + K_r(1 - \alpha_{cp})$$

Equation 2.10

$$\alpha_{cp} = 1 - \frac{ln(\frac{r_c}{r_0})}{\xi}$$

Equation 2.11

The stiffness of the raft and the pile group (P_r) can be estimated from elasticity theory as has been proposed by the other authors. The pile group stiffness can be obtained from equations proposed by *Poulos & Davis* (1980), *Fleming et al.* (1992), or *Poulos* (1989). The pile-raft interaction α_{cp} is a function of r_c (pile cap radius); r_0 (radius of the pile), and $\zeta = \ln(r_m/r_0)$. Based on the equations above, a tri-linear load settlement is defined. The total applied load, P_1, at which the pile capacity is reached, is given by:

$$P_1 = \frac{P_{up}}{1-X}$$

Equation 2.12

Where P_1 =ultimate load capacity of the piles in the group; and X = proportion of load taken by the piles defined in the equation given above. P_{up} is the ultimate load capacity of the piles in the group. After this point (point A in Fig. 2.5), the foundation system is only as stiff as the raft alone (Kr), and this holds until the ultimate load capacity of the piled raft system is reached (point B). But to work out the load-settlement curve for a raft with various numbers of piles, the aid of a computer spreadsheet or mathematical program has been recommended.

In the *second stage,* a more detailed design is performed by analyzing the maximum column load (concentrated loading) that a raft can take without needing a pile below the load. To determine whether a pile beneath the column is necessary, four conditions must be examined. These consist of:

- Maximum moment criterion
- Maximum shear criterion
- Maximum contact pressure criterion
- Local settlement criterion

In the *last stage*, the detailed design must be done. The original paper focused on six more dominant methods and studied them in order to propose a better method for design purposes. As reported by the author, these include:

- Poulos and Davis (1980)
- *Randolph* (1994)
- Strip on springs analysis, using the program GASP (*Poulos*,1991)
- Plate on springs approach, using the program GARP (*Poulos*, 1994a)
- Finite element and boundary element method of *Ta & Small* (1996)
- Finite element and boundary element method of *Sinha* (1996)

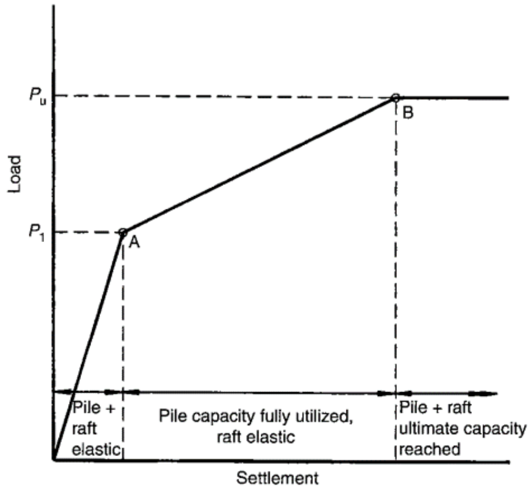

Fig. 2.5-Simplified curve for preliminary analysis -PDR (2001)

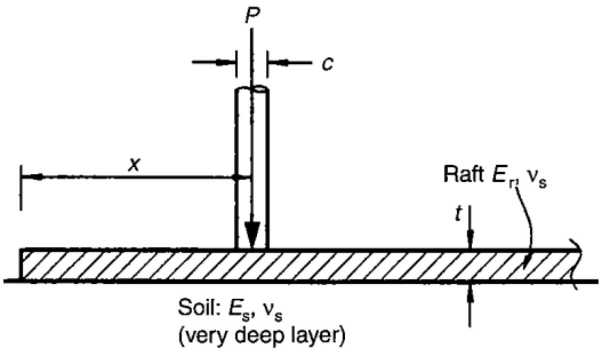

Fig. 2.6-Definition of the problem for an individual column load- PDR (2001)

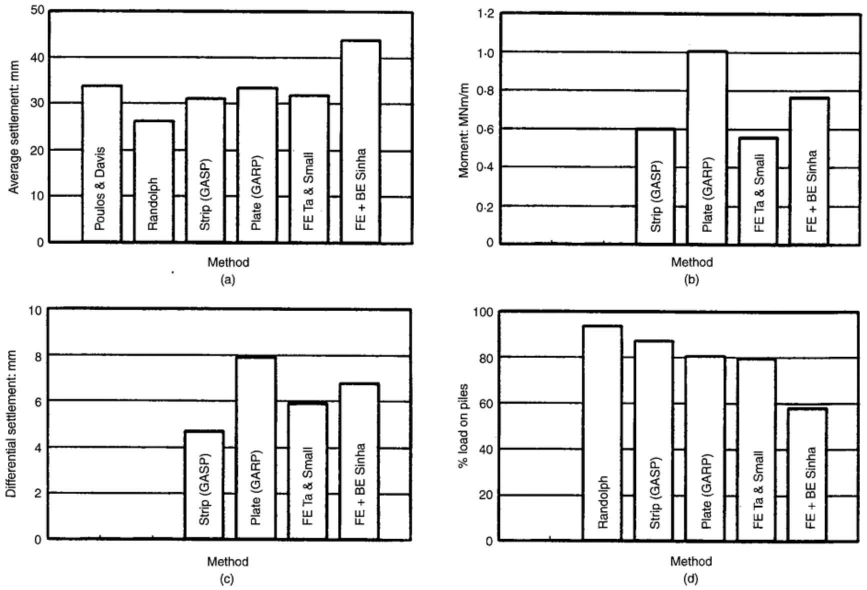

Fig. 2.7-Comparative results for hypothetical example _PDR (2001)

Fig. 2.7 compares these methods as presented in the original paper. We can see that the results are in fair agreement. The rest of the study then focused on the effect of some parameters on the results. That is to say that the author using the computer program GARP (*Poulos*,1994a), investigated the impact of the number of piles, type of loading, raft thickness, and applied load level.

B. Approximate Methods

These methods use some simplifications to reduce the workload of the computers used for the analysis, usually by modeling the pile-raft system as a combination of a plate or a series of strips supported by springs in place of the piles.

1. The strip on Spring Method:

The method replaces a section of the raft with a strip, and piles are represented by springs. When applying loads to a foundation, all possible interactions taking place, such as piles, rafts, and subsoil, are taken into account.

Poulos (GASP,1991): In 1991, he prepared a program named GASP based on the idea of modeling a strip footing (beams) equipped with piles. However, this model could be extended to cover piled-raft foundations as well. The boundary element was used to model the raft while the piles were replaced with springs. The piles' responses were to be obtained by the simplified methods of other authors. The contact pressure below the raft, therefore, consisted of the usual evenly distributed pressure in addition to the higher pressure at the connecting points of piles to the raft. Fig. 2.8 presents a schematic section of the problem.

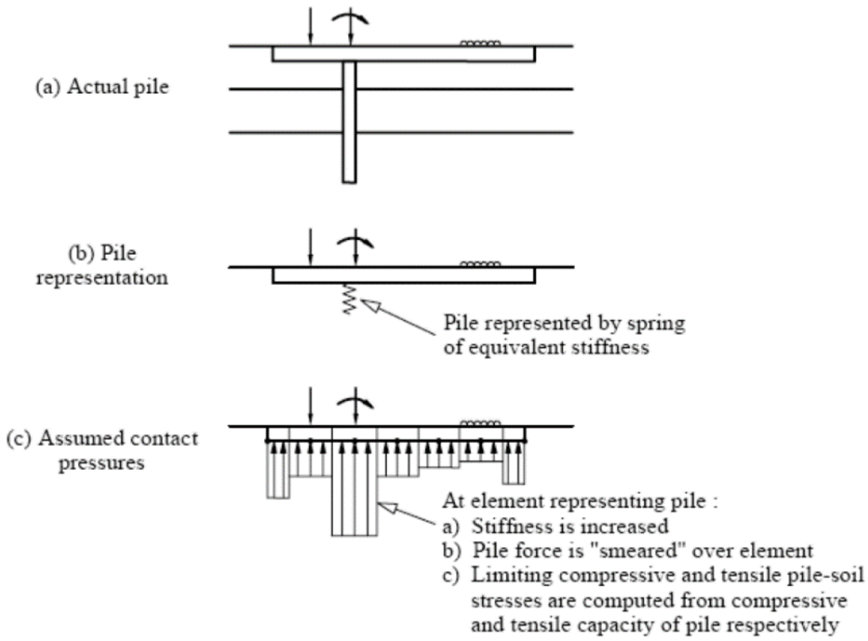

Fig. 2.8-Modeling of piles strip foundation via GASP

GASP made allowance for all the usual components and interactions, including raft-raft, pile-pile, raft-pile, and vice versa, and a representative strip section is then analyzed to obtain the settlements and moments due to the applied loading on that strip section plus the settlement caused by the section outside (Deka, 2014). The author reports a good agreement between the results obtained from the models and the real observations. There are some limitations to his method, which are discussed later.

2. Plate on Spring Method:

This approach represents the raft by a series of plate footings, and the piles are represented by springs of appropriate stiffness.

Poulos (1993_GARP): He suggested a method of simplification by modeling the raft as a thin plate and the piles as springs with calculated stiffness. The approximations involved are similar to those employed in the program GASP for piled strips. The analysis is based on elastic theory but considers the important non-linear features of the system: the development of limiting pressures below the raft and of the ultimate load capacity of the piles. In this paper, the raft is discretized into elements and nodes, and some equations are developed for its vertical settlement caused by bending moments, and soil contact pressures.

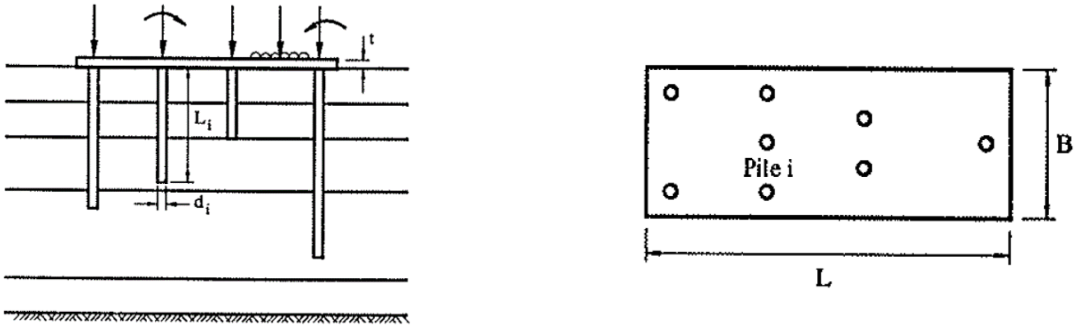

Fig. 2.9--Definition of piled raft problem
_GARP (93)

The equation of plate bending is expressed in incremental finite difference form as follows:

$$[D_p]\{\Delta\rho_r\} = \frac{\{\Delta q\} - \{\Delta p\}}{D}$$

Equation 2.13

Where [D] is the matrix of finite difference coefficient, $\{\Delta\rho_r\}$ represents the vector of incremental raft displacement, $\{\Delta q\}$ is the vector of incrementally applied loading on the raft, $\{\Delta\rho\}$ is the vector of incremental contact pressure between the underside of raft and soil and D is the bending stiffness of the plate. Assuming soil displacement behaves elastically, the vertical soil settlement can be caused by two main sources, namely, contact pressure and free-field movements of the soil.

$$\{\Delta\rho_s\} = [I_s]\{\Delta\rho\} + \{\Delta S_0\}$$

Equation 2.14

In the expression above$\{\Delta\rho_s\}$ is the vector of incremental soil displacements, and $[I_s]$ can be gained from Boussinesq or Mindlin solutions. The piles, as shown in Fig. 2.8, are modeled by springs.

Russo (1998): Russo developed his approximate numerical method in 1998. In his approach, the raft is modeled as a plate and piles as interacting linear or non-linear springs. The soil is modeled as an elastic layer, and all the displacements were calculated by Boussineq's formula. A hyperbolic load-settlement curve was applied to the piles for modeling the non-linear behavior.

The lumped stiffness of the soil springs is to be calculated from the closed-form solutions for the settlement of a uniformly loaded rectangular area at the boundary of a homogeneous elastic half-space.

In the next step, FEM has been implemented by means of four rectangular node elements. The governing equation of the raft bending would be as follows since it behaves elastically.

$$D \times \nabla^4 \omega(x, y) = q(x, y)$$
Equation 2.15

Where ω(x, y) is the unknown vertical displacement of the raft, q(x, y) is the applied load, and D is the bending stiffness. it can be found by:

$$D = \frac{E_r \times t^3}{12 \times (1 - \nu_r^2)}$$
Equation 2.16

can be rewritten in the form as $[K_r] \times \{\omega_r\} = \{q\}$ where $[K_r]$ and $\{\omega\}$ are, respectively, the stiffness matrix and the vector of the unknown nodal displacements of the raft, while $\{q\}$ denotes the vector of the nodal forces or moments acting on the raft. As for modeling the piles and soil behavior, *Boussinesq's* expression was used for the soil, and since piles were assumed to be nonlinear, the springs representing them were analyzed by the analytical expression of *Chin's* hyperbola.

To verify the results generated by the model, some parameters were compared against some known solutions. For example, we can see in Fig. 2.10 (below) that a decent agreement exists between the raft-soil stiffness and soil settlement relation computed by NAPRA and the *Wardle and Fraser* estimation (raft has been considered alone with no piles).

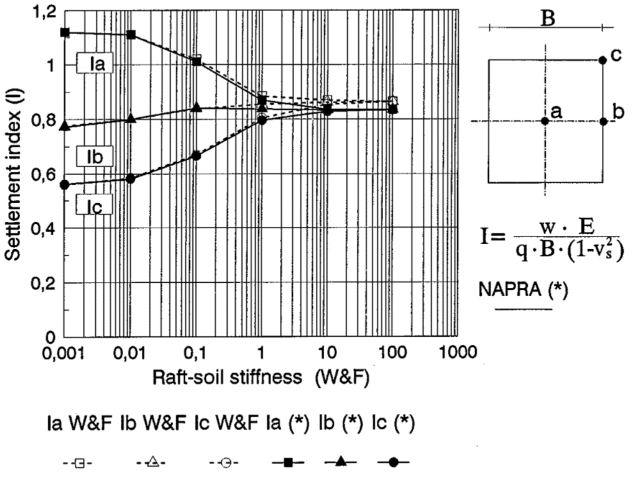

Fig. 2.10-Comparison between solutions for an unpiled raft_ Russo (98)

.

C. Rigorous methods

These methods are mainly based on the use of computer programs. As stated by Poulos (2001), they can be classified into three main groups:

- Boundary element methods, in which both the raft and the piles within the system are discretized and based on the elastic theory (e.g., Butterfield and Banerjee, 1971; Brown and Wiesner, 1975; Kuwabara, 1989; Sinha, 1997)
- Methods combining boundary elements for the piles and finite element analysis for the raft (e.g., Hain and Lee, 1978; Ta and Small, 1996; Franke et al., 1994; Russo and Viggiani,1998)
- Simplified finite element analyses usually involve the representation of the foundation system as a plane strain problem (Desai,1974) or an axisymmetric problem (Hooper, 1974),

Brown and Wiesner (1975): In 1975, Brown and Wiesner modeled the foundation system via a strip supported by some piles on the center line. Their method employed BEM (Boundary Element method) method.

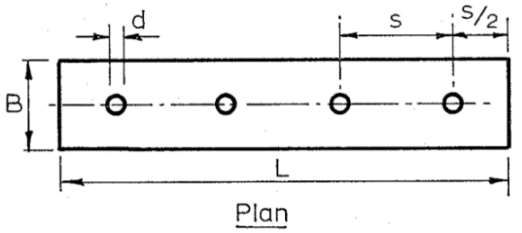

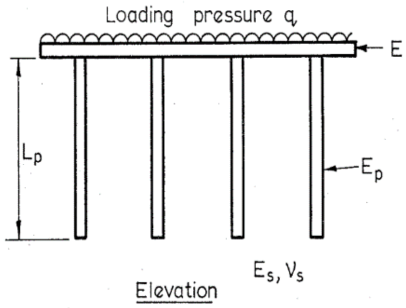

Fig. 2.11-The type of the problem considered _Brown and Wiesner (75)

They assumed the interaction stresses on the exterior surface of a pile to consist of zones of uniform vertical stress and one zone of normal stress at the base of the pile. Using the technique described by Poulos and Davis (1968) for integrating Mindlin's expression, the following equation can give the interaction stress on every zone of the footing and the piles in addition to the soil displacement at the center of every zone of the footing and piles caused by that stress.

$$I = \frac{1+v}{8\pi(1-\nu)E_s}[\frac{Z_1^2}{R_1^3} + \frac{3-4\nu}{R_1} + \frac{5-12\nu+8\nu^2}{R} + \frac{(3-4\nu)z^2-2cz+2c^2}{R^3} + \frac{6cz^2(z-c)}{R^5}]$$

Equation 2.17

$$R^2 = z^2 + a^2 + r^2 - 2ra\cos\theta$$

$$R^2{}_1 = z^2{}_1 + a^2 + r^2 - 2ra\cos\theta$$
Equation 2.18

The integration presented in Equation 2.17 with respect to "r" can be carried out analytically, but numerical methods must be used for solving the integration with respect to θ. According to Mattes and Poulos (1969), other relations can be established if the piles are considered as simple compression members and application of simple bending theory for the strip foundation. The soil and pile displacements are equated at the center of each zone, and the vertical equilibrium equation is used to determine the interaction stresses. Bending moments and settlements of the footing are calculated from these stress values.

The authors extended the study by looking into some important factors and showed that:

(1) Percentage of the total load taken by piles: it was shown in the graph (Fig. 2.12) that for a given s/d if the Kp increases, the share of the load carried by the piles increases as well.

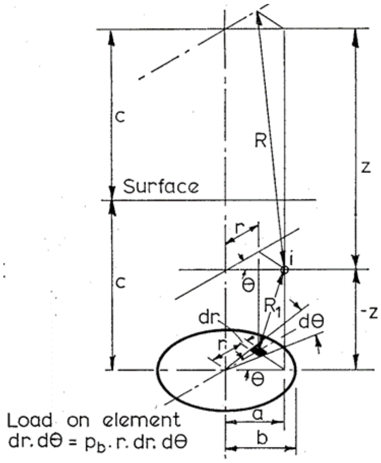

Fig. 2.12-Integration of Mindlin's equation _Brown and Wiesner (75)

.

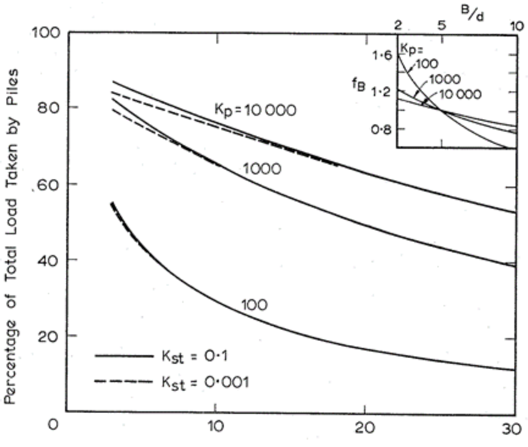

Fig. 2.13--The percentage load taken by piles_ Brown and Wiesner (75)

(2) Maximum footing displacement: the authors were able to define the following equations that can give f_L (correction factor for a change in strip length) for the range 15<L/d<150

$$f_L = 0.063\alpha^3 - 0.44\alpha^2 + 1.158\alpha + 0.222, \quad K_p=100$$
$$f_L = 0.035\alpha^3 - 0.305\alpha^2 + 1.120\alpha + 0.150, \quad K_p=1000$$
$$f_L = 0.034\alpha^3 - 0.294\alpha^2 + 1.134\alpha + 0.126, \quad K_p=10000$$

Equation 2.19

(3) Maximum differential displacement: based on the graphs presented in Fig. 2.14, the differential displacement for the footings was not dependent on the quantity of the piles.

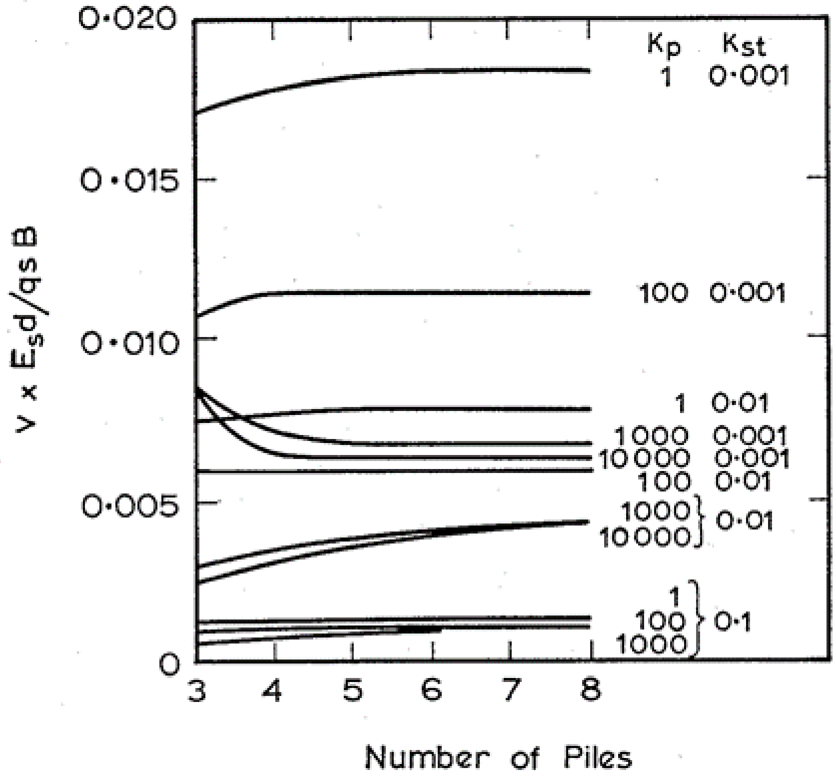

Fig. 2.14-Differential displacement for a footing with L/d=50, B/d=5- Brown and Wiesner (75)

Griffiths et al. (1991): They conducted a finite element analysis with a computer program. The piles were modeled via rod elements and the raft by 'thin plate' elements. Three major interactions were considered in the study, i.e., pile-soil-pile, pile-soil-raft, and raft-soil-raft. Mindlin's (1936) elastic continuum solution was used to model the pile group to provide interaction effects between pile nodes.

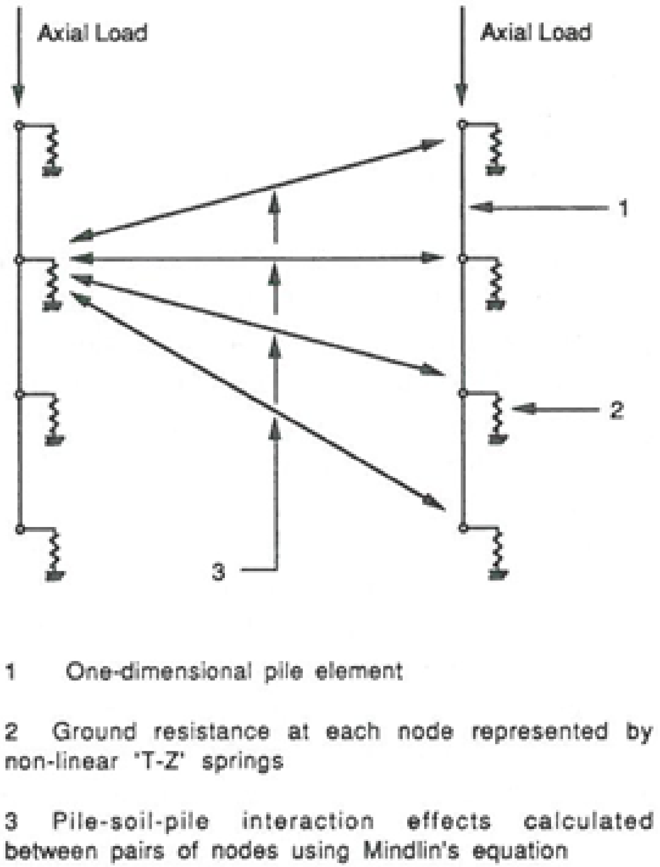

Fig. 2.15--Representation of piles and soil_-Griffiths et al. (91)

The study employed four-node quadrilateral isoparametric plate bending elements with three degrees of freedom at each node, a transverse displacement, and two rotations. In light of the possibility of transverse displacement, the plate should be considered as a thick element. The connected nodes shared vertical freedom.

A soil spring stiffness simulation was carried out using Giroud's method (1968). The raft-soil-raft interaction, the raft-soil-pile interaction, and the pile-soil-raft interaction are defined in conjunction with Mindlin's expressions.

The study showed that the load pile-stiffness ratio is the main factor determining the average displacements and load-sharing mechanism. When compared to Randolph's approximate method of the piled raft, the results confirmed that the load distribution between piles and rafts varies with pile stiffness.

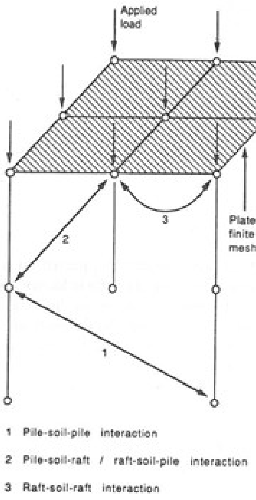

Fig. 2.16-Full pile group analysis, including raft-soil-pile interaction_ Griffiths et al. (91)

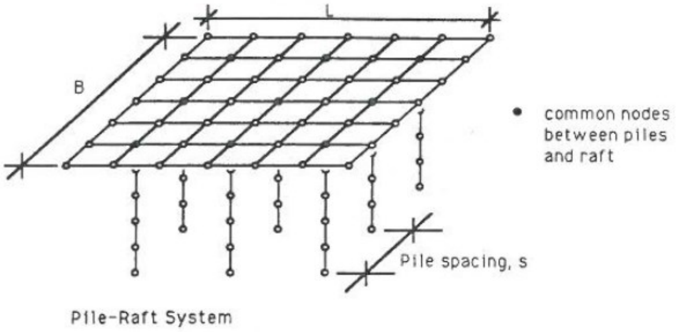

Fig. 2.17-Pile raft system_ Griffiths et al. (91)

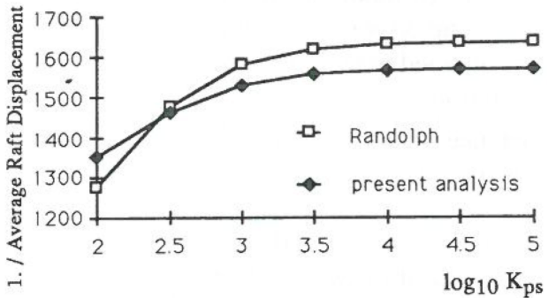

Fig. 2.18- Overall stiffness of pile-raft foundation_ Griffiths et al. (91)

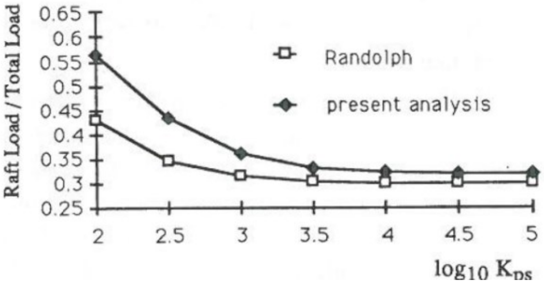

Fig. 2.19- Proportion of total load carried by raft_ Griffiths et al. (91)

Clancy and Randolph (1993): These two authors used a hybrid method to investigate piled rafts performance and mechanism. The finite element method was employed for analyzing a raft while connected piles were modeled by rods. The analytical approach computed the soil reactions. They combined the two parts of the analysis on the basis of displacement compatibility at the base of the piles. Mindlin's theory was used for determining the interaction between the piles through the boundary element method with a difference in the approach as the original method involved integration, but here no integration was needed since the forces were considered to be lumped at each pile node. Spring replaced the soil response for each node raft with Giroud's solution.

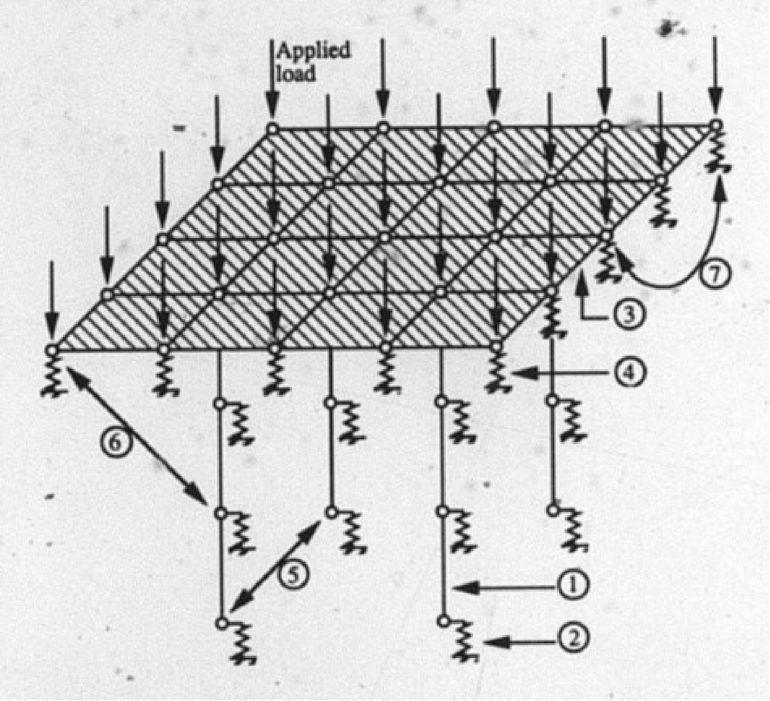

Fig. 2.20-Numerical representation of piled raft_ Clancy and Randolph (96)

- One-dimensional pile element
- Ground resistance at each pile node is represented by non-linear 'T—Z' springs
- Two-dimensional plate-bending finite element raft mesh
- Ground resistance at each raft node is represented by an equivalent spring
- Pile-soil-pile interaction effects calculated between pairs of nodes using Mindlin's equation
- Pile-soil-raft interaction
- Raft-soil--raft interaction

Two essential factors, i.e., α_{pr} and α_{rp}, were introduced to evaluate the interaction of the two components of the foundation. So, the general equation can be expressed in the form:

$$\begin{bmatrix} \frac{1}{k_p} & \frac{\alpha_{pr}}{k_r} \\ \frac{\alpha_{rp}}{k_p} & \frac{1}{k_r} \end{bmatrix} \begin{Bmatrix} P_p \\ P_r \end{Bmatrix} = \begin{Bmatrix} \omega_p \\ \omega_r \end{Bmatrix} \qquad \text{Equation 2.20}$$

Where:

ω_p = average displacement of the pile group in the combined foundation
ω_r = average displacement of a raft in the combined foundation
P_p = total load carried by pile group in combined foundation-
P_r = total load carried by raft in the combined foundation
k_p = overall stiffness (P/ω) of pile group in isolation
k_r = overall stiffness (P/ ω) of raft in isolation

α_{rp} = *interaction factor of a pile group on the raft*
α_{pr} = *interaction factor of a raft on pile group*

For a rigid raft, $\omega_p = \omega_r$, and the overall pile-raft displacement will subsequently be referred to as ω_{pr}. The overall stiffness of the pile-raft system (k_{pr}) is calculated as follows:

$$k_{PR} = \frac{(p_p+p_r)}{\omega_{pr}} = \frac{[k_p+k_r(1-2\alpha_{rp})]}{[1-\left({k_r}/{k_p}\right)\alpha_{rp}^2]} \qquad \text{Equation 2.21}$$

Two α_s are found to be: $\alpha_{rp} = 1 - {\ln(n)}/{\ln\left(\frac{2r_m}{d}\right)}$ and $\alpha_{pr} = \alpha_{rp}\, {k_r}/{k_p}$

The method studied in this paper turns out to be accurate for the single pile units but less accurate as the size of the pile group increases. This, however, can be addressed by an appropriate interaction factor as suggested by the authors.

Ruel and Randolph (2002): Performed tests with 259 different piled raft configurations utilizing three-dimensional elastoplastic finite element analysis. The pile positions, the pile number, the pile length, the raft-soil stiffness ratio, and the load distribution on the raft varied.

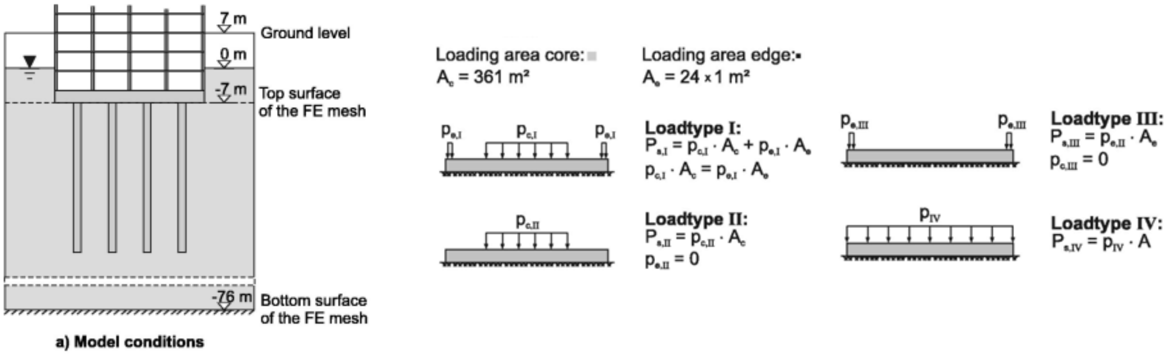

Fig. 2.21-System configurations and load configurations for parametric study_ Ruel and Randolph (2002)

Their parametric study showed that a foundation optimized design depends on the soil conditions, load configuration, and load level. Nevertheless, they concluded that generalizing the results presented in their paper to all possible cases was impracticable. The important findings of the study are:

- With longer piles, smaller settlements are achieved than with more piles for the same total pile length

- the average settlement is the only parameter that is reduced compared to the unpiled raft, due to the installation of piles, at least for all configurations studied in the scope of this research work
- With increasing load levels, the overall stiffness of a piled raft decreases, so differential settlements are more affected by raft-soil stiffness ratio and load configuration than average settlements.

D. Experimental Methods

These methods are those investigations performed either on a field study basis and real micropile-rafts or the scaled models in the laboratory. The measuring devices are attached to the elements, and empirical relations are defined based on the outputs.

Han and Ye (2006) performed a field study on a micropiled raft comprising a square raft supported by four micropiles 150 mm in diameter and spaced at 5D. It was found that:

- Approximately 70% to 86% of the additional load applied to the raft after underpinning was transmitted by the micropiles
- load capacities of micropiles in the single-pile loading test and the underpinned foundation loading test were almost identical
- Underpinned foundation loading test micropiles yielded before the soil mobilized fully and transferred the load back to the soil.
- there was good agreement between the experimentally-gained values for the ratio of the load carried by the plate and micropiles and the estimation made by Randolph's formula:

$$P_r/(P_r + P_{pg}) = [(1-\alpha_{rpl})k_r]/[k_{pg} + (1-\alpha_{rpl})k_r] \qquad \text{Equation 2.22}$$

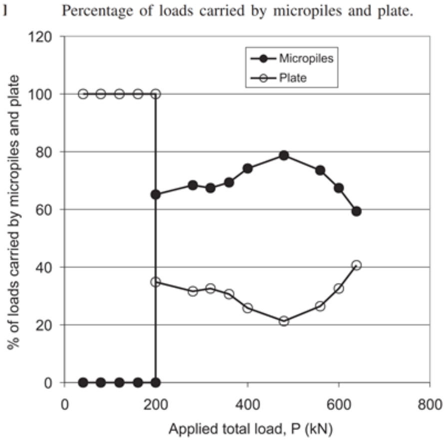

Fig. 2.22-Additional applied load_ Han, and Ye (2006)

Alnuaim et al.(2014): In 2014, another study with the help of a centrifuge machine was conducted in Newfoundland at Memorial University by Alnuaim et al. The model was made of PVC, considering the appropriate scaling calculations.

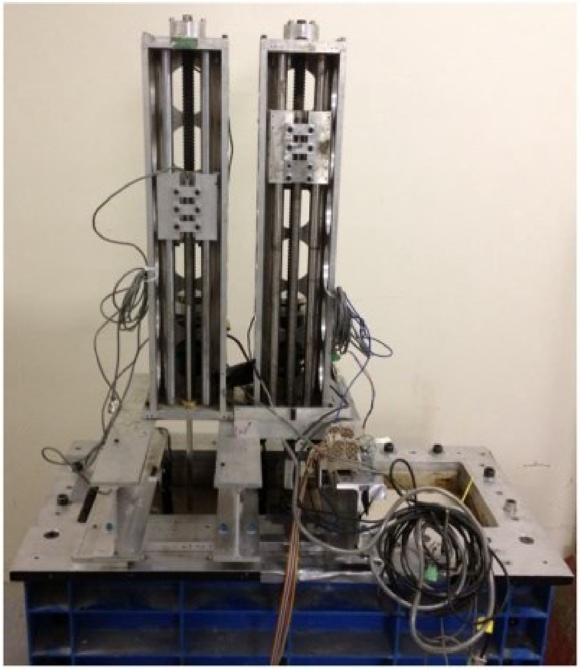

Fig. 2.23-Complete centrifuge package assembled_ Alnuaim et al (2014)

According to the authors, since no clear definition for the failure mechanism existed at the time of the test, the ultimate load was interpreted as the load corresponding to a pile head displacement equal to 10% of the pile diameter (Terzaghi, 1942). Three separate centrifuge tests were conducted: a single pile as a reference, a raft without any micropiles, and finally a micropiled-raft. The settlement-loading curve was used to define the stiffness of the whole structure. According to the study, the main outcomes of the study can be listed as 1) micropiles can increase the axial stiffness significantly 2) the prediction made by the PDR method was of decent accuracy when compared with the actual field data 3) assuming that skin friction is evenly spread on the outer surface of a micropile is not reasonable as it has the highest value in the upper segment of the micropile close to the raft and it decreases as the depth increases. 4) The contribution of end bearing resistance of the micropiles was 7%–10% of the total applied load. 5) As stated by Han and Ye, the axial load carried by a single micropile as a component of micropiled-raft is very similar to that of a single micropile.

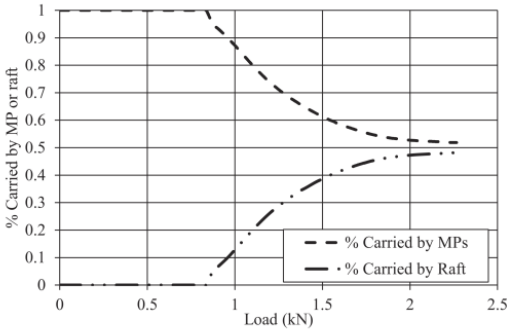

Fig. 2.24-Load sharing between micropiles and raft_ (Alnuaim et al, 2014)

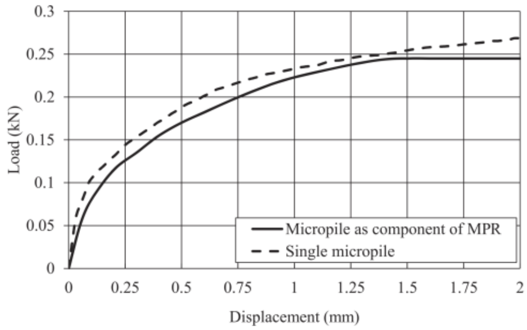

Fig. 2.25-Axial load carried by single micropile as a component of MPR Alnuaim et al (2014)

2.4.Effects of Different Parameters on Piled-Raft Performance

A. Effects of number of piles and type of loading

Previously we said that Randolph's (1994) expression could calculate the axial stiffness of a piled raft by:

$$Kpr = \frac{K_{PG}+(1+2\alpha_{rp})K_r}{1-[\alpha_{rp}{}^2(\frac{K_r}{K_{PG}})]} \qquad \text{Equation 2.23}$$

K_{PG} (Stiffness of the pile group) is given by Fleming et al.'s equation $K_{PG} = n^{1-e}K_p$ Where "n" represents the number of piles, therefore, it can safely be said that more piles will result in a larger K_{PG} and, consequently, greater K_{PR}. The study by Davis et al. proved this point and showed that the settlement of the system depends on the quantity of the piles as normally would be expected.

This is, to some extent, in line with the findings of Poulos [2000]. He concluded that general settlement decreases with the larger number of piles, and if piles are small in number, the maximum settlement for concentrated loading is larger than for uniform loading, but this difference vanishes as more piles are placed under the raft.

In terms of load distribution Poulos (Poulos, 2000) found that the more piles are included in the system, the more load is transferred to them but after a certain number, in his case 15 piles, the rate of transfer stops. The type of loading has almost no effect on the total load carried by the piles.

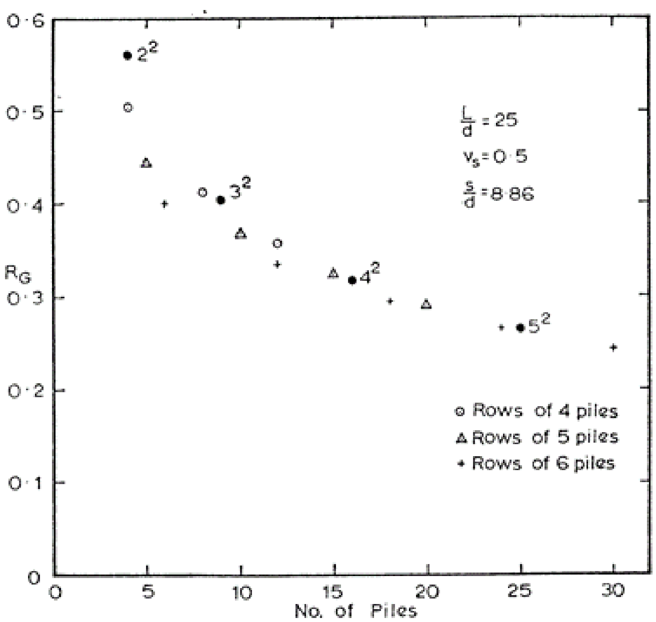

Fig. 2.26-Influence of pile arrangement(Poulos,2000)

B. Effects of Raft Thickness

As we know from Equation 2.24, the stiffness of a raft has a direct relationship with the third power of thickness. So, the slightest change in the thickness leads to a large increase in the stiffness of the raft, and consequently, as we have seen in Poulos's study, this means that a smaller differential settlement will occur. Moreover, other parameters such as the distribution of the loads and differential settlement are influenced by the stiffness and, basically, by the thickness.

$$Kf = 5.57\frac{E_r(1-\nu^2{}_s)}{E_s(1-\nu^2{}_s)}\left(\frac{S_B}{S_L}\right)^{\alpha}\left(\frac{t_r}{S_L}\right)^3$$ Equation 2.24

According to Poulos (2001), neither the maximum settlement nor the percentage of load taken by the piles is affected by the raft thickness. However, in a numerical study performed by Sinha and Hanna (Sinha, 1996) it was observed that settlement measured at the center of the raft decreased with the increase in the raft thickness up to a certain limit, after which the settlement increased with the increase in the raft thickness probably due to the self-weight of the raft. It was confirmed, that differential settlement is reduced by a thicker raft as it acts as a solid body and distributes the loading evenly between the piles leading to a smaller differential settlement.

C. Effects of Angle of Shearing Resistance and Cohesion

Fig. 2.27 shows a graph of Sinha and Hanna’s (2015) study in the form of a load-settlement curve for different angles of shearing resistance. The settlement decreases with an increase in the angle of shearing resistance from 10 to 15°.

As for the differential settlement, Fig. 2.29 shows the settlements at the center and corner points of the raft. The settlement pattern of these two points for various shearing resistance angles was similar; meaning that φ had no significant effect on the differential settlement between points within the raft.

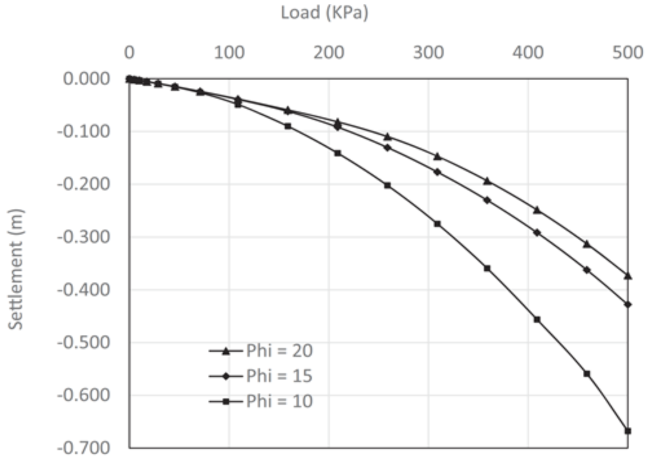

Fig. 2.27-Settlement at raft top center for different internal frictional - Sinha and Hanna (2015)

\.

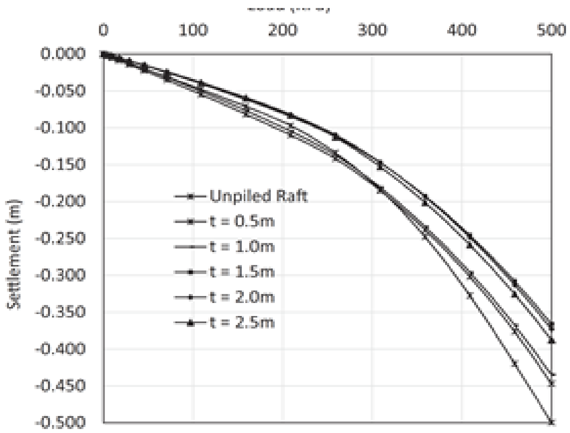

Fig. 2.28--Settlement at raft top center for different raft thicknesses Sinha and Hanna (2015)

.

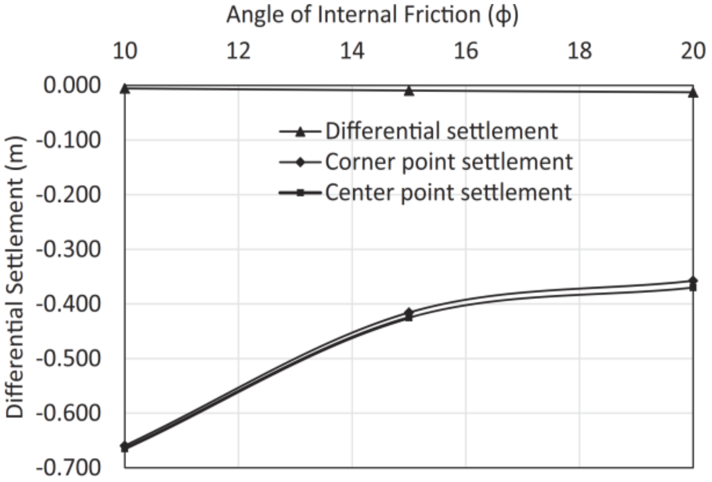

Fig. 2.29-Different settlements of the raft for different soil internal frictional angles_ Sinha and Hanna (2015)

The effects of soil cohesion c also have been studied in Sinha and Hanna's study (2015). They found that the capacity of the system increases with an increase in soil cohesion from 10 to 25 kPa. Moreover, it was observed that the soil cohesion had no significant effect on the differential settlement but increased the load-bearing capacity of the system.

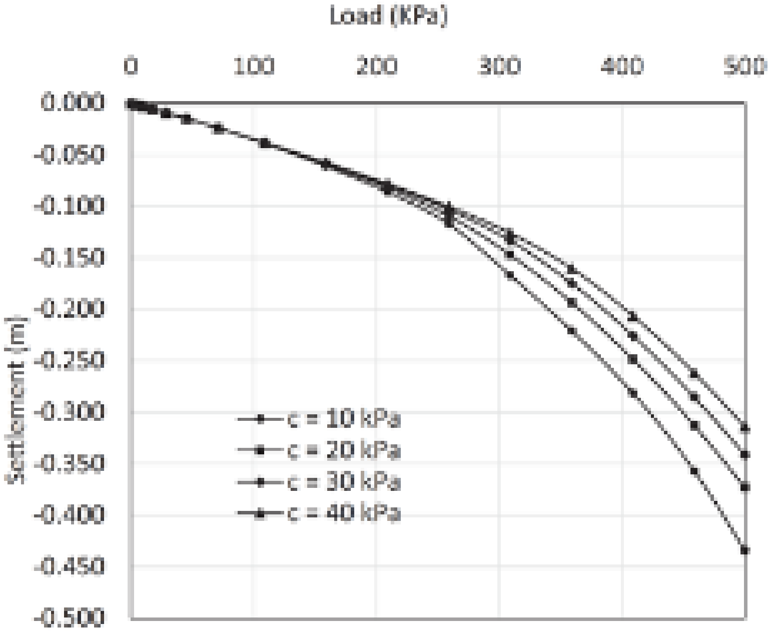

Fig. 2.30-Settlements at raft top center for different soil cohesions

D. Effects of Poisson Ratio

Brown and Wiesner (Brown, et al., 1975) observed that when Poisson's ratio of the soil is reduced from 0.5 to 0 (zero), the percentage of the load taken by the piles is increased by 20% of the total load. However, this factor, according to them does not influence the amount of differential settlement and settlement. Davis et al. (Davis, et al., 1972) report that the variation of RG (group reduction factor) with ν is linear, so interpolation might be an acceptable choice. Therefore, a settlement of the system can be calculated from the settlement of a single pile under the same conditions.

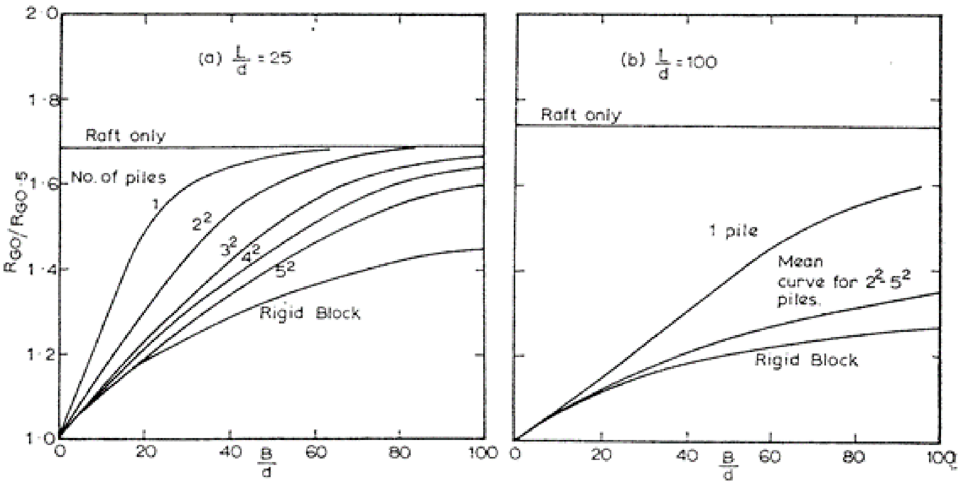

Fig. 2.31-Influence of the Poisson ration on RG_ Brown and Wiesner (75)

2.5.Discussion

It is evident from the literature review that the subject of micropiled-rafts has not received the attention it deserves as the majority of the papers were on piled rafts, whereas we know that micropiles, due to their slenderness and high grout bonding, behave differently. The insufficient number of studies on MPR foundations calls for more research. On the other hand, we know that the observed limitations cannot be overcome by using the other analysis methods dedicated to piled raft foundations because of the differences in the working mechanism of micropiles as a result of their smaller size and pressurized grouting.

This thesis will investigate the sharing mechanism of micropiled-rafts by conducting a series of experiments on small-scale models in the sand. The results will then be used to generalize the findings for different configurations of micropiles and raft thickness.

CHAPTER 3. EXPERIMENTAL STUDY

3.1.General

The experimental work of this research was conducted by compressive load tests on the small-scale model micropiled-rafts. A steel tank equipped with a reaction frame held the sand needed for the tests. Upon filling up the whole tank with the desired relative densities, D_r=30%, 45%, and 60%, the micropile part of the model was driven into the sand by means of a strain-controlled actuator until the raft touched the surface of the sand and then all the measuring instruments were turned on to measure the parameters while the raft experienced gradually increasing settlement.

Silica sand 4010 was selected to reproduce the properties of cohesionless soil on a smaller scale to avoid the scale effect as much as possible. An actuator provided the needed force along with constant rate displacement to drive the micropile and conduct the actual tests.

Three configurations of micropiles setup were tested with the difference being in the number of the micropiles and their arrangements. The necessary instruments had been mounted on the appropriate spots to measure the parameters including forces and the strains in relation to associated displacement.

3.2.Test setup

A. Sand properties

As mentioned earlier, silica sand "*4010*" was used for the experimental tests. The main reason for this choice was that the fine grading of this type could mitigate the problems of scale effect to some extent due to the smaller difference between the grain sizes and the dimensions of the model.

Fig. 3.1-A bag of Sand 4010

In order to determine the properties of the sand, standard tests were performed. ASTM C136 was the standard test for sieve analysis of fine and coarse aggregates. The resultant grading curve (Fig. 3.2) was quite in accordance with what had already been found in other studies performed on the same sand (Di Camillo, 2014).

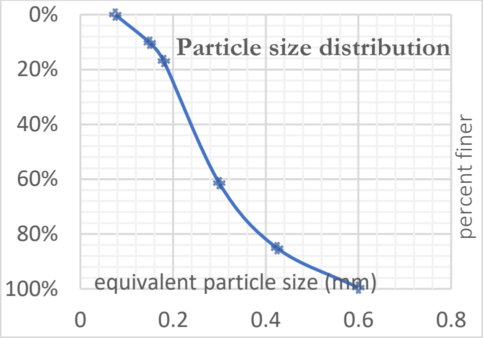

Fig. 3.2_Sand grading

As for the other specifications required from the sand sample, other tests were conducted, such as a specific gravity test, direct shear test, and relative density. Based on these tests, the important parameters can be tabulated in the following table.

Friction angle Variation with Relative Density (F. Dicamelio) (ASTM D 3080)		
Relative density	Void ratio	Friction angle
30	0.71	31.05
45	0.67	33.88
60	0.65	36.4

Table 3.1-Friction Angle Variation with Relative Density

The C_u of the sand (uniformity coefficient) based on the curve is calculated as 1.90. As for the specific gravity, a test done according to ASTM D854 evaluated it as 2.60. Also, the maximum and minimum unit weight based on the findings of other researchers on the same sand was 17.16 and 14.05 kN/m$^{3.}$

Standard	Property	Value
ASTM C136 / C136M-19	D_{10} (mm)	0.148
	D_{30} (mm)	0.210
	D_{50} (mm)	0.256
	D_{60} (mm)	0.280
	C_u	1.76
	C_c	1.00
ASTM D7263	Max unit weight (kN/m^3)	17.32
ASTM D7263	Min unit weight (kN/m^3)	14.05
ASTM D7263	Max Void ratio	0.51
ASTM D7263	Min Void ratio	0.82
ASTM D854	Specific Gravity (G_s)	2.60

Table 3.2_Sand 4010 Properties

The internal friction angle ϕ of the sand, as reported in other studies performed on the same sand, is a function of relative density. The table below summarizes this linear relationship.

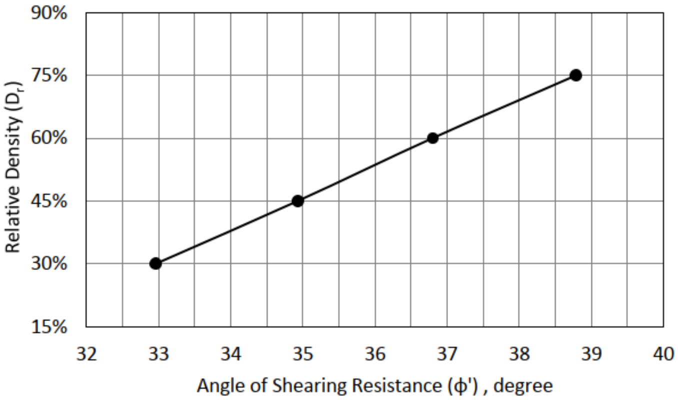

Fig. 3.3- Friction angle of sand (Alharthi, 2018)

B. Tank setup

A tank-frame arrangement filled with different homogenous relative densities was the main element in our tests. The width, length, and height of the tank were 100, 100, and 120 cm, respectively. A reaction frame on the upper half of the tank held the actuator responsible for providing the force needed for driving the models in the sand and constant displacement.

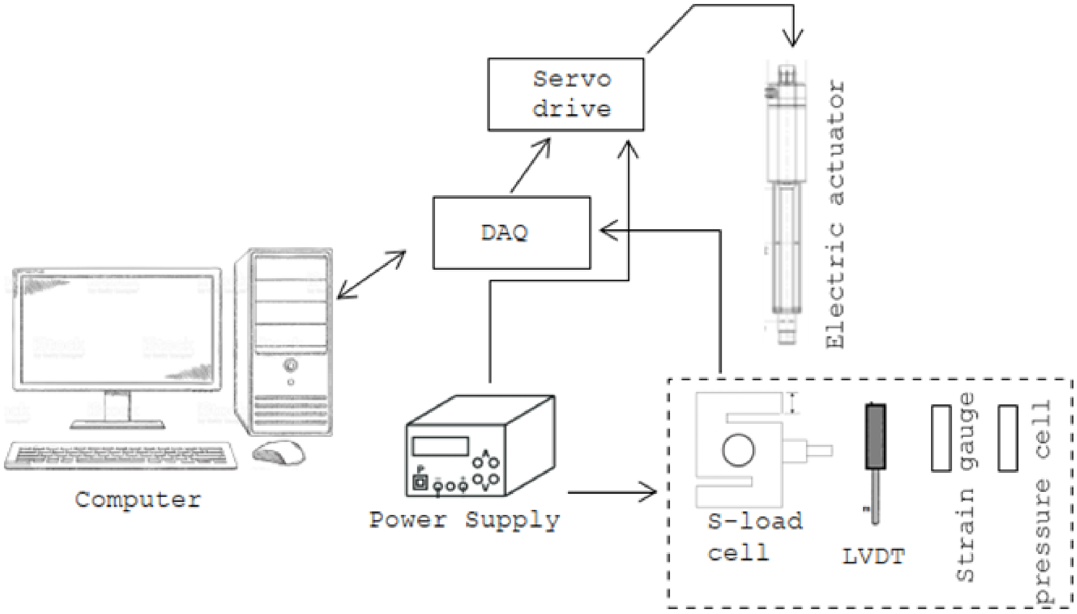

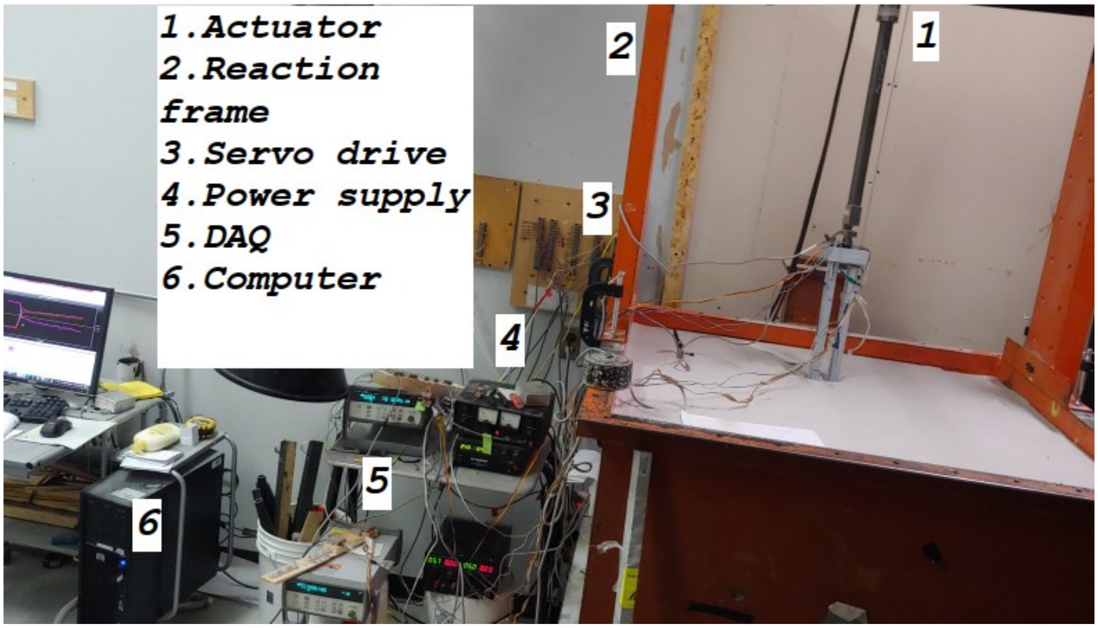

Fig. 3.4-Setup of experimental tests

C. Compaction

Three uniform relative densities were prepared for the tests, 30%, 45%, and finally 60%. Achieving this relative density was made possible by using a compaction plate. The number of the needed blows had been determined previously by Alharti and Dicamellio (Alharthi, 2018) in their tests with the same sand. The tables below show the thickness of the eight layers (15 cm) and the corresponding blows applied to produce the target relative densities.

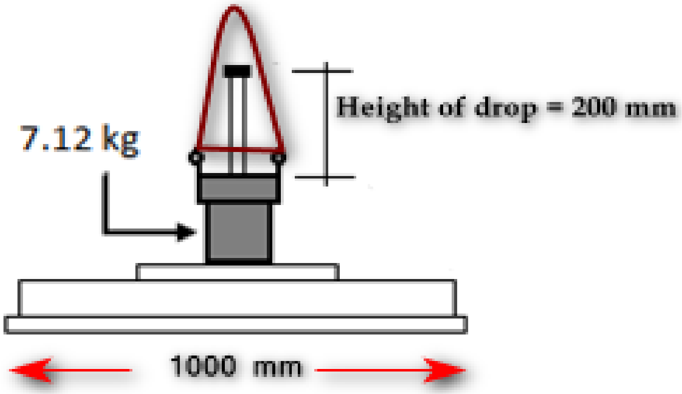

Fig. 3.5-Compaction plate

Layer No i	Layer Thickness D (mm)	Depth at mid layer d_L -	Target Relative Density D_r (%)	No. of Drops N -	Dry Unit Weight γ_d (kN/m^3)	Relative Density D_r (%)	Angle of Shearing Resistance ϕ' (degree)	Theoretical Vertical Stress $\sigma_{v\,(Th)}$ (kPa)	Measured Vertical Stress $\sigma_{v\,(M)}$ (kPa)
8	150	75	30	76	14.82	30.48	33.0	1.11	3.89
7	150	225	30	76	14.93	34.38	33.5	3.34	9.16
6	150	375	30	76	14.90	33.16	33.3	5.58	14.66
5	150	525	30	70	14.88	32.63	33.3	7.81	17.63
4	150	675	30	57	14.92	33.84	33.4	10.05	21.28
3	150	825	30	57	14.72	27.14	32.6	12.27	21.51
2	150	975	30	55	14.89	33.00	33.3	14.49	-
1	150	1125	30	55	-	-	-	-	-

Table 3.3-Test results for sand at a relative density of 30% (Alharthi, 2018)

Layer No i	Layer Thickness D (mm)	Depth at mid layer d_L -	Target Relative Density D_r (%)	No. of Drops N -	Dry Unit Weight γ_d (kN/m^3)	Relative Density D_r (%)	Angle of Shearing Resistance ϕ' (degree)	Theoretical Vertical Stress $\sigma_{v\,(Th)}$ (kPa)	Measured Vertical Stress $\sigma_{v\,(M)}$ (kPa)
8	150	75	45	183	15.34	47.77	35.3	1.15	4.68
7	150	225	45	172	15.34	47.91	35.3	3.45	12.06
6	150	375	45	170	15.23	44.38	34.8	5.74	16.61
5	150	525	45	155	15.34	47.89	35.3	8.04	20.14
4	150	675	45	110	15.27	45.72	35.0	10.33	25.59
3	150	825	45	95	15.15	41.82	34.5	12.62	29.60
2	150	975	45	92	15.23	44.30	34.8	14.89	-
1	150	1125	45	70	-	-	-	-	-

Table 3.4-Test results for sand at a relative density of 45% (Alharthi, 2018)

Layer No i	Layer Thickness D (mm)	Depth at mid layer d_L -	Target Relative Density D_r (%)	No. of Drops N -	Dry Unit Weight γ_d (kN/m^3)	Relative Density D_r (%)	Angle of Shearing Resistance ϕ' (degree)	Theoretical Vertical Stress $\sigma_{v\,(Th)}$ (kPa)	Measured Vertical Stress $\sigma_{v\,(M)}$ (kPa)
8	150	75	60	380	15.58	55.50	36.2	1.17	6.58
7	150	225	60	345	15.78	61.46	37.0	3.52	13.28
6	150	375	60	340	15.58	55.29	36.2	5.87	21.47
5	150	525	60	325	15.74	60.28	36.9	8.22	29.49
4	150	675	60	240	15.61	56.20	36.4	10.57	34.25
3	150	825	60	220	15.61	56.21	36.3	12.91	32.28
2	150	975	60	210	15.60	56.06	36.3	15.25	-
1	150	1125	60	185	-	-	-	-	-

Table 3.5-Test results for sand at a relative density of 60% (Alharthi, 2018)

D. PVC Micropiled-raft Model

Six models were built out of PVC and based on a prototype micropile (L=15m, Dia=0.15m). They were all covered in sandpaper grit 150. This coarseness rating had been determined to best represent the friction angel between concrete and sand material in a study by Di Camillo (2014). The hypothetical typical prototype micropiled-raft was designed according to the FHWA reference manual's recommended procedure. The basic PVC model had a single micropile in the center. The other models had four micropiles at different spacings (s/d=3 & 4) while the thickness of the raft was kept constant. The rest of the models were unpiled rafts. To scale down the dimensions of the prototype, the main factor to consider is the axial rigidity of the micropile, which must be respected. The length was simply worked out based on linear scaling laws.

$$\text{Length of the model (PVC Rod)} = \frac{\text{Length of the prototype micropile(15m)}}{\text{Scaling factor (n=19)}} = 0.8\text{ m}$$

Equation 3.1

Axial rigidity must be considered to calculate the diameter of a micropile, which is not as straightforward as calculating the length. As described in the book "Geotechnical Modeling," the ratio of $\frac{1}{2}\left(\frac{l}{r_0}\right)^2\left(\frac{G}{E}\right)$ must be identical for the model and the prototype (Wood, 2004). Thus, assuming that the model micropile is 80 cm long (n=19), the diameter of the model is given below.

$$d_m = \frac{l_m\sqrt{\frac{G_m}{E_m}}}{\frac{l_p}{r_p}\sqrt{\frac{G_p}{E_p}}} = \frac{0.8\sqrt{\frac{G_m}{2.9\times 10^9}}}{\frac{15}{0.15}\sqrt{\frac{G_p}{30\times 10^9}}} = 2.54\text{ cm}$$

Equation 3.2

Where letters "m" and "p" refer to the model and prototype; and G is the shear modulus of the respected materials.

The thickness of the model rafts was calculated using the solution of Fraser & Wardle (1976) in such a way that the stiffness of the raft was higher than 100 which made the resulting thickness a rigid raft. The spacing between the prototype micropiles was taken as per recommendation in FHWA, i.e., 3d and 4d.

Dimensions of the Prototype	
Length of the micropile	1500 cm
Diameter of the micropile	15 cm
Spacing between micropiles	75 cm
The thickness of the raft	35 cm
Dimensions of the model (sMPR- Single micropiled raft)	
Length of the micropile	80 cm
Diameter of the micropile	2.54 cm
Spacing between micropiles	NA
The thickness of the raft	3.2 cm
Dimensions of the model (fMPR-Four micropiled rafts)	
Length of the micropile	50 cm
Diameter of the micropile	1.58 cm
Spacing between micropiles	3d & 4d (see, below)
The thickness of the raft	3.2 cm

Table 3.6- Properties of the PVC models

.

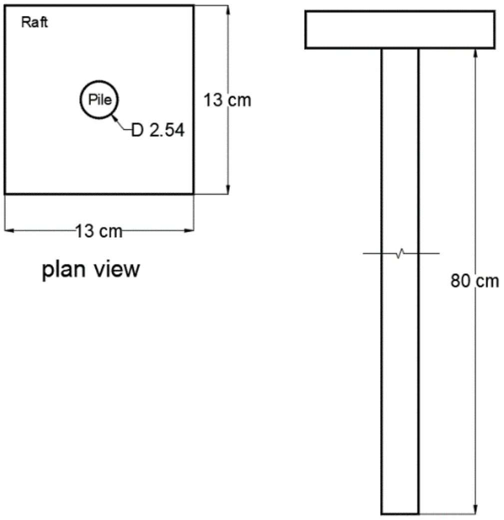

Fig. 3.6-Single micropiled-raft unit (Model A)

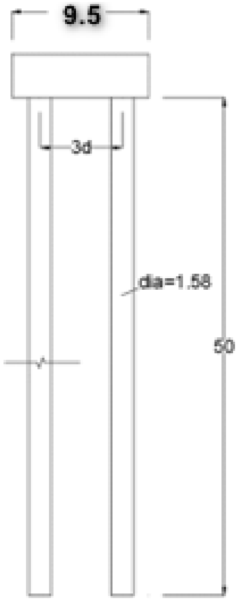

Fig. 3.7-fMPR.1 (dimensions in cm) – Model B (Spacing=3D)

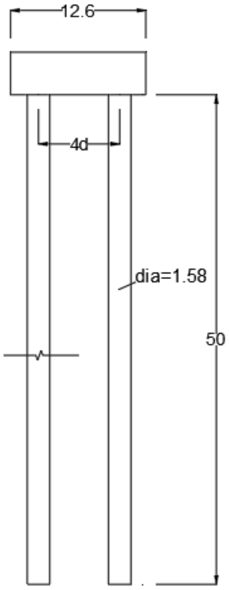

Fig. 3.8-fMPR.2 (dimensions in cm) _Model C(Spacing=4D)

.

Fig. 3.9- PVC Rod acted as Micropile

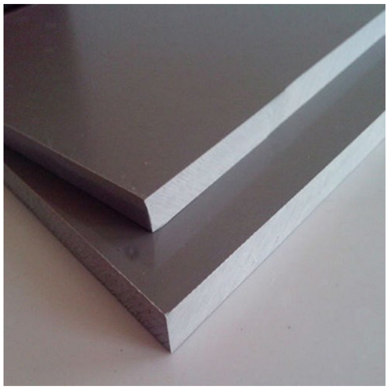

Fig. 3.10-PVC sheet acted as Raft

3.3.Instrumentations

Several instruments were implemented into the model to measure the needed paraments. A DAQ system was the heart of the system and responsible for reading all the output data from the sensors. Two DC power supplies with different output voltages also were put to use to power up the sensors.

Fig. 3.11- DAQ 34972 (Keysight,2021)

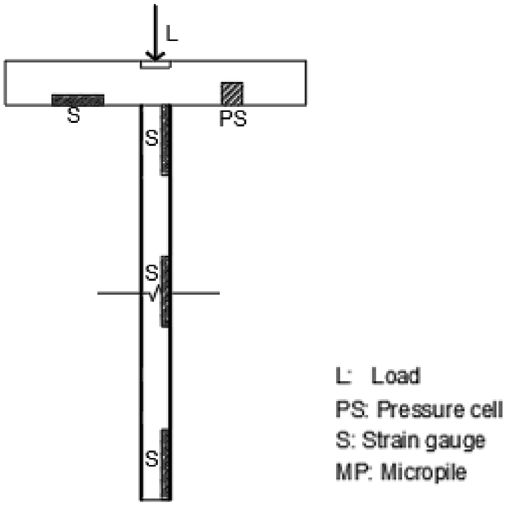

Fig. 3.12-sMPR instrumentation

The positions of the sensors on the models are shown in the picture on the right (Fig. 3.12). A sensor/strain gauge at the toe of the pile determined the micropile end-bearing capacity. A pressure transducer measured the pressure under the raft. Finally, the total load on the model was measured by an S-Load cell. Force at the top of the pile, which represents the total bearing capacity of the micropile, is calculable from the difference of total load from the loads at the micropile's toe. A strain gauge was mounted at the top of the pile (below the raft) to verify the last measurements.

A. Verification of the relative density of the compacted sand

To verify that the desired D_r of the sand has been achieved, several empty cans with known dimensions and weights were placed between the layers to assess the relative density of each layer based on the weight of the trapped soil and the sizes of the cans (Fig. 3.13).

B. Total load

An S-load cell with 8000 Kgf force capacity was installed on the end of the actuator's arm to measure the total load applied to the models. The sensor's output was connected to the DAQ, reading it every 1 second (Fig. 3.14).

Fig. 3.13-Placing density can and pressure sensors

.

Fig. 3.14-Measuring total load (S-Load cell)

C. *End bearing capacity of micropile*

The most challenging part of the instrumentation was to come up with a solution that could fit into a pipe of 1” diameter. Initially, it had been planned to use strain gauges on the tip but during the calibration process, upon more inspections, it was found that for the larger model, a pressure sensor performed better than a strain gauge for measuring the tip resistance. Finally, it was decided to use a piece of precise pipe as the housing (L=10 cm) to protect the pressure cell (Fig. 3.15)when the model was being pushed into the sand (jacked). Sensors wires ran on the PVC rod up to the top and passed through a hole in the raft. In the smaller models, i.e. four micropiled rafts, since there was no room for the sensor, strain gauges were used instead.

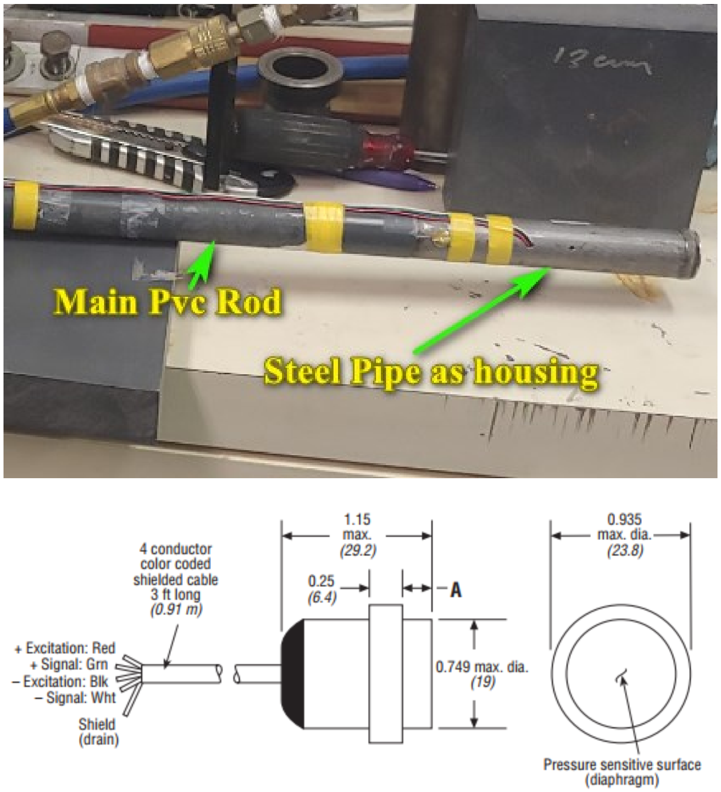

Fig. 3.15-Pressure sensor to measure the load at the toe of the micropile model

D. *Pressure under the raft*

For finding the individual load share of each element, two miniature pressure transducers from “Honeywell” were put on the bottom surface of the raft. Their size called for caution as they were fragile, but on the other hand, the results they produced were accurate thanks to little interference made by them in the contact area(Fig. 3.16).

Fig. 3.16-Pressure transducers
(the pressure under the raft)

E. *Displacement*

Unlike the failure mechanism defined for regular shallow footings in which a foundation undergoes a noticeable and large amount of tilting and sinking into the ground, the bearing capacity of the rafts in the SLS method (Serviceability Limit State) is defined based on the tolerable amount of overall and differential settlement. Therefore, capturing the exact value of the settlement at each specific moment and the correlating force is of great importance. Two LVDTs from Omega Company were responsible for measuring the settlement of the structure. They produced a curve of the settlement against the compression force.

Fig. 3.17- LVDT (Omega,2022)

F. *The total load carried by each micropile*

Even though the total load carried by the pile could be deduced solely from the difference between the total load and the sum of tip pressure and the pressure under the raft, an additional strain gauge was used to verify the readings of contact pressure.

Amongst the best strain gauges available in the market, the product of Omega company was chosen, and a 350-ohm strain gauge (SGD-1.5/120-LY11) was applied near the head of the micropile. A Wheatstone bridge manufactured by Omega was also added to the wiring to eliminate the noise to the greatest extent possible.

Fig. 3.18-The Wheatstone bridge used in the experiments (Omega,2021)

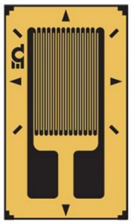

Fig. 3.19-Strain Gauge (SGD-1.5/120-LY11) (Omega,2021)

G. *Flexural strain*

The flexural strain of the raft was measured with a strain gauge installed under the raft. The strain gauge was stuck at the midpoint between the edge of the raft and the circumference of the micropile. The measured voltages then were converted to strain by applying the gauge factor, in this case, 2, which knowing the flexural modulus of elasticity, produced the values of flexure stress.

3.4.Loading Actuator

The loading system consisted of an electric cylinder Actuator. To apply a precise voltage in order to get a constant displacement from the actuator, a servo drive was used. The DAQ system along with a computer program, provided the low signals to the servo driver so that it could be converted into a power signal understandable by the actuator. The capacity of the actuator had been listed as 25 kN.

Fig. 3.20- Actuator

3.5.DAQ system

Two Data acquisition systems were responsible for recording the output data from the sensors, including the pressure sensors, instrumented piles, and also from the LVDT and controlling the precise movement of the strain-controlled actuator. Each DAQ system could take 3 card units each capable of reading 20 channels at each scan cycle. Each sensor needed a pair of channels except for strain gauges that used four channels to accommodate the 4-wire measuring technique.

Fig. 3.21-DAQ and Power supply

.

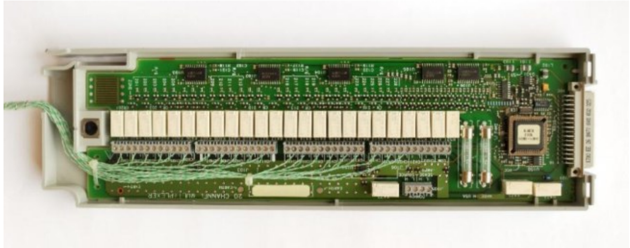

Fig. 3.22-Multiplexer (2/4-wire) Module

3.6. Calibration of the sensors

Based on the guidelines provided by the manufacturers, the recommended procedures followed for calibrating the sensors were different. For the S load cell, the sensor was calibrated with another known calibrated load cell. The actual pressure applied by the Instron machine was recorded against the voltage produced by the target sensor. This data produced a linear curve which could be used later to determine the load taken by the whole structure.

Calibration of the LVDT was performed using metal cubes with known heights. Starting with the first cube, the resulting voltage was measured. This process continued with all the other cubes to find the corresponding voltages. It produced the curve presented below.

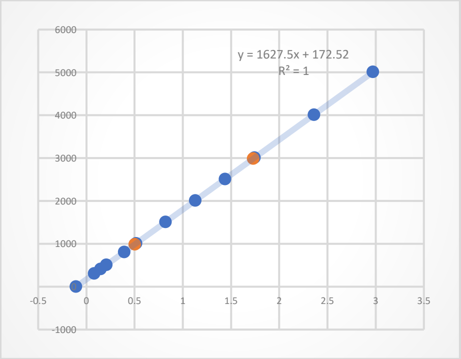

Fig. 3.23-S-load cell calibration

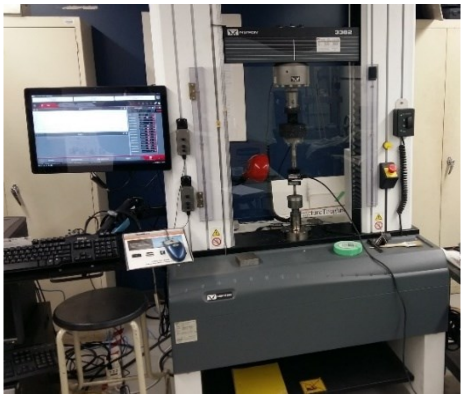

.

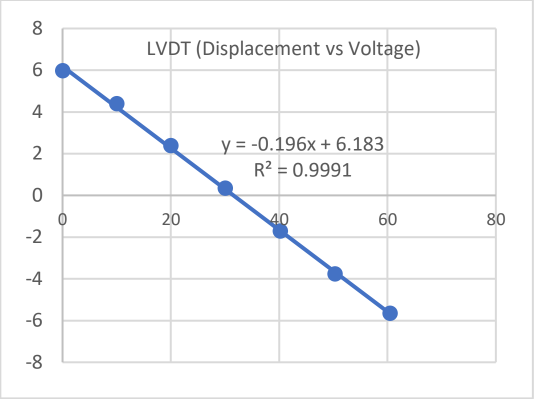

Fig. 3.24-Displacement(cm) vs Voltage(v)- LVDT calibration

.

CHAPTER 4. EXPERIMENTAL TEST RESULTS

4.1. General

In this chapter, the results of the experimental tests are presented. Table 4.1 lists these results.

Test code name	Relative density of sand	Raft Size (cm)	No of piles	MP (length/dia)(cm)	MP spacing	BC(kN)	Actual stiffness(MN/m)	PDR (MN/m)	Raft load (kN)
1	30	13×13×3.8	0	0	-	1.00	1.57		
2	45	13×13×3.8	0	0	-	1.40	2.10		
3	60	13×13×3.8	0	0	-	2.00	2.94		
4	30	9.5×9.5×3.8	0	0	-	0.60	0.70		
5	45	9.5×9.5×3.8	0	0	-	0.85	1.00		
6	60	9.5×9.5×3.8	0	0	-	1.15	1.20		
7	30	12.5×12.5×3.8	0	0	-	0.65	0.90		
8	45	12.5×12.5×3.8	0	0	-	1.10	2.00		
9	60	12.5×12.5×3.8	0	0	-	1.40	2.40		
10	30	-	1	80/2.54	-	0.52	1.95		
11	45	-	1	80/2.54	-	0.71	2.32		
12	60	-	1	80/2.54	-	1.06	2.68		
13	30	13× 13× 3.8	1	80/2.54	-	1.75	3.00		0.60
14	45	13× 13× 3.8	1	80/2.54	-	2.00	3.50		0.75
15	60	13× 13× 3.8	1	80/2.54	-	2.25	4.00		1.00
16	30	9.5×9.5×3.8	4	50/1.58	3d	1.40	3.40	3.60	0.85
17	45	9.5×9.5×3.8	4	50/1.58	3d	1.80	3.70	4.02	1.00
18	60	9.5×9.5×3.8	4	50/1.58	3d	2.50	4.90	4.41	1.20
19	30	12.5×12.5×3.8	4	50/1.58	4d	1.70	3.50	3.65	1.39
20	45	12.5×12.5×3.8	4	50/1.58	4d	2.00	3.75	4.04	1.40
21	60	12.5×12.5×3.8	4	50/1.58	4d	2.60	5.00	4.42	1.56

- All the models were covered entirely with sandpaper (Grit 150)

s/d: the ratio of micropile spacing to its diameter

Table 4.1- Experimental tests program

Due to different types of failures observed during the preliminary tests performed on unpiled rafts, which were mostly "local shear failure" and "punching shear failure," it was necessary to define a constant criterion for bearing capacity evaluation. Among the most common methods for evaluating the bearing capacity of footings, four methods were:

1. Choosing the footing stress corresponding to a limiting relative settlement value, normally s/B=0.1, as proposed by Briaud and Jeanjean (1994).
2. Determining the footing stress which corresponds to a distinctive change in the settlement. Two tangent lines are drawn from the beginning straight portion of the curve and the straight end portion of the curve. The point where these two tangents cross each other is called the point of failure. The pressure corresponding to this point is called the ultimate bearing capacity of the soil.
3. DeBeer (1970) uses the method in which the footing stress-settlement curve is created using logarithmic scales, and an intersection point defines the bearing capacity.
4. Choosing a reasonable model to fit the stress vs. settlement data and extrapolating to the asymptotic value corresponding to an upper limit of stress: referred to as the Hyperbolic Method.

Because of the micropiles' presence, the ultimate capacity was interpreted as the bearing stress corresponding to the lesser of either limiting relative settlement value (e.g., s/B=10%) (Briand and Jeanjean 1994), sometimes referred to as the 0.1 B Method, or a distinctive change in the settlement so that consistent results would be produced.

These tests were conducted on the sands with relative densities of 30%,45%, and 60%. Three different-sized models were put to the test. The rafts were instrumented with one or two pressure sensor(s) to evaluate the pressure underneath the raft. Two LVDTs mounted on a bracket measured the displacement. The total force applied to the model was measured by means of an s-load cell. The results from the unpiled rafts (Fig. 4.1) and single micropiles were used as a reference for the assessment of the results from other models, such as the single and the four micropiled-raft models.

4.2.Unpiled rafts

A. R-130 -30%

The load-displacement curve for this test shows that the foundation (an unpiled square raft with the dimension of 13 × 13 cm in the sand with D_r=30%) underwent a local shear failure. The bearing capacity from the curves can be determined as 1.00 kN. The axial stiffness from the same curve was computed and it is 1.57 MN/m. (Fig. 4.2).

B. R-130-45%

Based on the load-settlement curve of this model, it appears that the foundation (a 13×13 cm square raft in the sand with a D_r of 45%) sustained a local failure. The bearing capacity from the curves can be determined as 1.40 kN. The axial stiffness from the same curve was computed and it is 2.10 MN/m. Because of the sand's higher stiffness than the previous test, R-13-45% shows a

33% increase over R-13-30% (Fig. 4.3).

Fig. 4.1- Unpiled raft tests

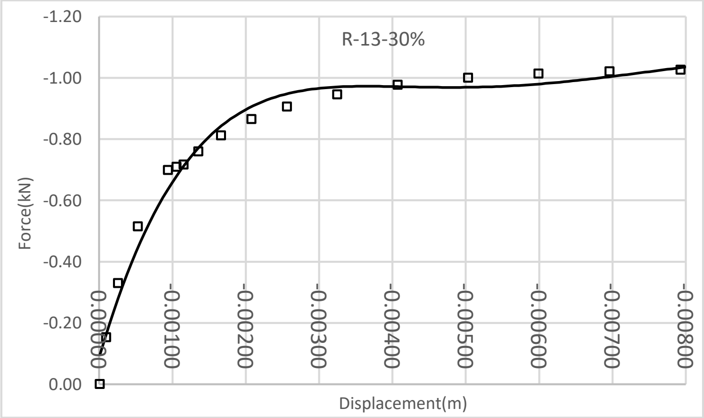

Fig. 4.2- Load-Settlement (R13-13-30%)

.

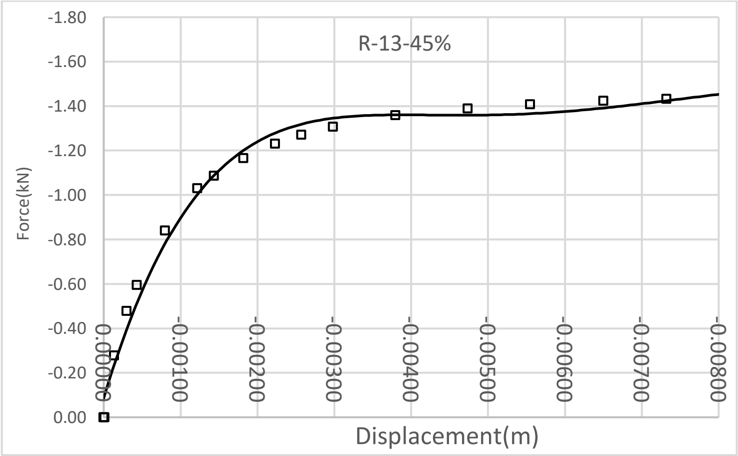

Fig. 4.3- Load-Settlement (R13-13-45%)

C. R-130-60%

The load-settlement curve of this model demonstrates that the foundation (an unpiled square raft with a dimension of 13 × 13 cm in the sand with D_r=60%) endured a local shear failure. The bearing capacity from the curves can be determined as 2.00 kN. The axial stiffness from the same curve was computed and it is 2.94 MN/m. The bearing capacity of R-130-60% increased by 40% and 87% compared to R-130-45% and R-130-30%, respectively, because of the higher stiffness of the sand.

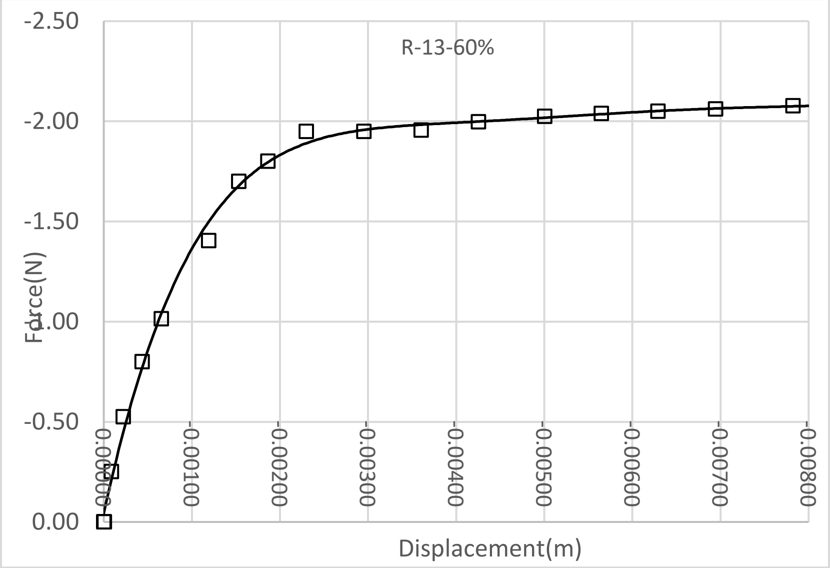

Fig. 4.4- Load-Settlement (R13-13-60%)

D. R-95-30%

For this test, the load-displacement curve shows that the foundation (a 9.5 × 9.5cm square raft in the sand with D_r=30%) underwent a local shear failure. The bearing capacity from the curves can be determined as 0.60 kN. The axial stiffness from the same curve was computed and it is 0.70 MN/m. (Fig. 4.5)

E. R-95-45%

During this test, the foundation experienced a local shear failure (Fig. 4.6). The bearing capacity from the curves can be determined as 0.85 kN. The axial stiffness from the same curve was computed and it is 1.00 MN/m.

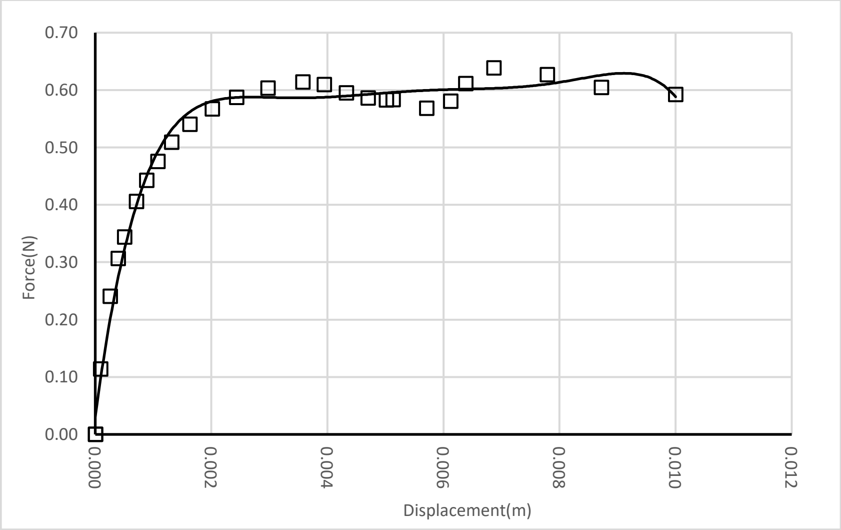

Fig. 4.5-Load vs settlement-unpiled raft (R-95-30%)

.

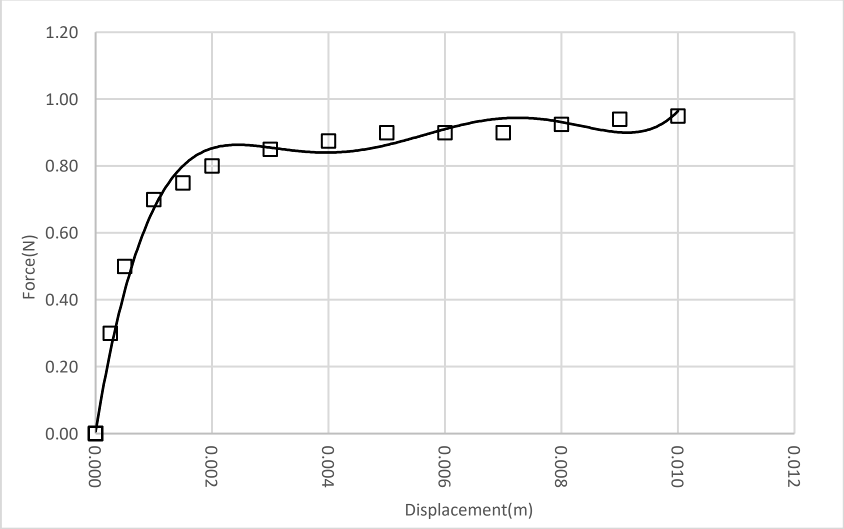

Fig. 4.6-Load vs settlement-unpiled raft (R-9.5-45%)

F. R-95-60%

For this test, the load-displacement curve showed that the foundation (a rectangular raft with a dimension of 95 by 95 cm in the dense sand, i.e., Dr=60%) collapsed under general shear (Fig. 4.7). The bearing capacity from the curves can be determined as 1.15 kN. The axial stiffness from the same curve was computed and it is 1.20 MN/m.

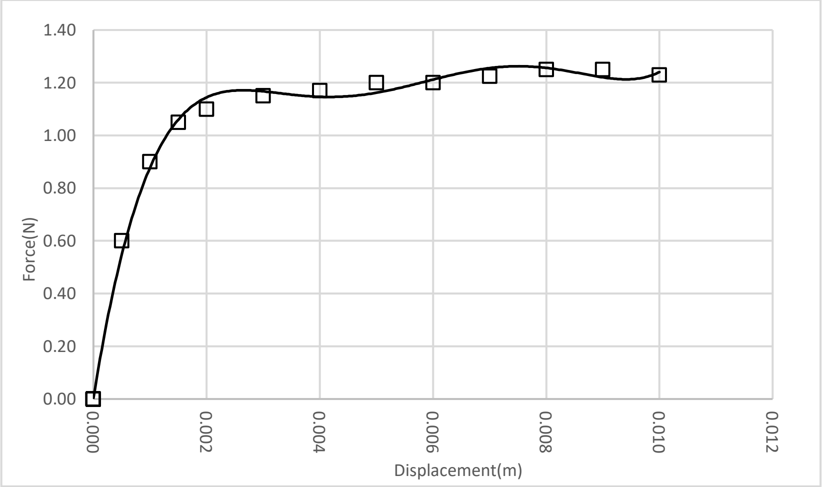

Fig. 4.7-Load vs settlement-unpiled raft (R-9.5-60%)

G. R-125-30%

In this test, the foundation (an unpiled square raft in the sand with a raft dimension of 12.5 x 12.5 cm) experienced a general shear failure (Fig. 4.8). The bearing capacity from the curves can be determined as 0.65 kN. The axial stiffness from the same curve was computed and it is 0.9 MN/m.

H. R-125-45%

The load-displacement curve for this test demonstrates that the foundation (an unpiled square raft with a dimension of 12.5 × 12.5 cm in the sand with (D_r=45%) experienced a general shear failure (Fig. 4.9). The bearing capacity from the curves can be determined as 1.10 kN. The axial stiffness from the same curve was computed and it is 2.00 MN/m.

I. R-125-60%

The load-displacement curve for this test shows that the foundation (an unpiled square raft with the dimension of 12.5 × 12.5 cm in the dense sand with D_r=60%) experienced a general shear failure (Fig. 4.10). The bearing capacity from the curves can be determined as 1.40 kN. The axial stiffness from the same curve was computed and it is 2.40 MN/m.

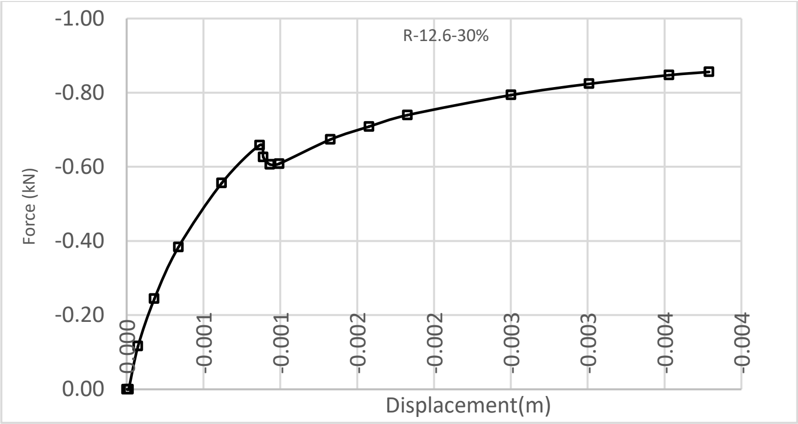

Fig. 4.8- Load vs settlement (R-12.5-30%)

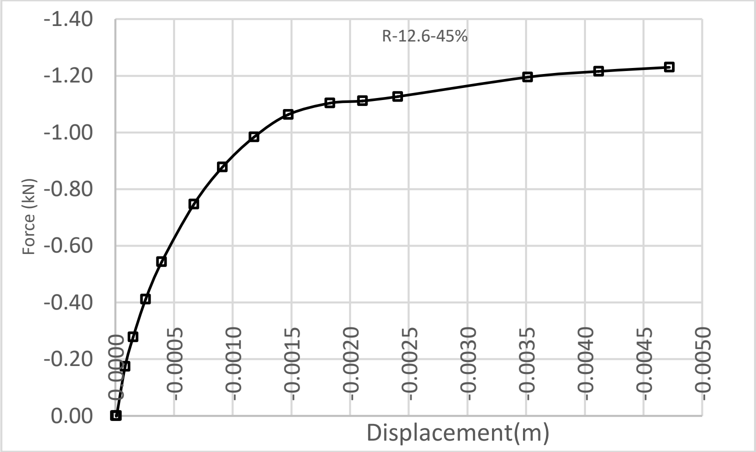

Fig. 4.9-Load vs settlement (R-12.5-45%)

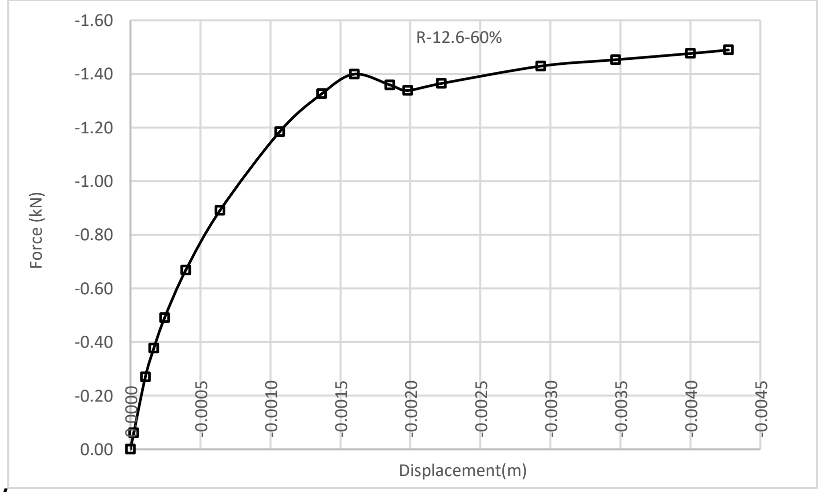

Fig. 4.10-Load vs settlement (R-12.5-60%)

4.3. Single micropile load test

To conduct this series of tests, a sand-papered PVC rod (Día= 2.54 cm & Length= 80 cm) was used. The measuring instruments were used to record the total load applied to the model and a pressure sensor to measure the pressure at the toe of the pile. A strain gauge at the midpoint of the pile was responsible for measuring the compressive strain. The results of the tests are presented below. Different values of failure points were observed corresponding with the other relative densities of the sand.

A. MP-30

The failure point of the single micropile test in the sand with 30% relative density at the settlement of 0.258 cm (10% of the micropile diameter) was found to be 0.52 kN (Fig. 4.11). The force reached 25% and 54% of the total load applied on the micropile at the toe and midpoint of the micropile, respectively. Axial stiffness was calculated to be 1.943 MN/m based on the slope of the initial part of the curve in the elastic zone. Also, the average skin friction was 5.84 kN/m^2.

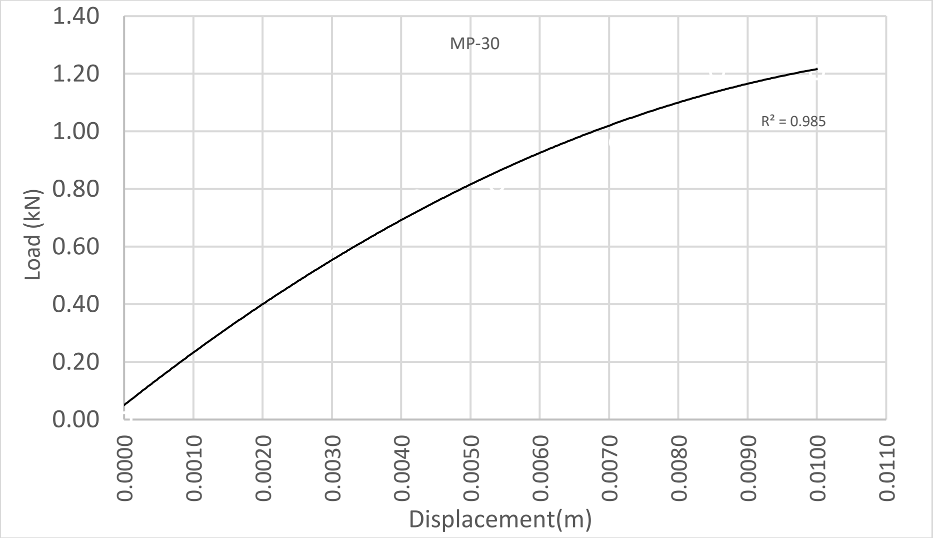

Fig. 4.11-Load vs settlement (MP-30)

B. MP-45

The failure point of the single micropile test in the sand with the relative density of 45% at 0.258 cm of settlement (10% of the micropile diameter) is computed to be 0.71 kN (Fig. 4.12). The force reached 24% and 52% of the total load applied on the micropile at the toe and midpoint of the micropile, respectively. Axial stiffness was calculated to be 2.317 MN/m based on the slope of the initial part of the curve in the elastic zone. Also, the average skin friction was 9.05 kN/m2.

C. MP-60

The failure point of a single micropile in the sand with a relative density of 60% at the settlement of 0.258 cm (10% of the micropile diameter) is measured to be 1.06 kN (Fig. 4.13). The force reached 25%, and 54% of the total load applied on the micropile at the toe and midpoint of the micropile, respectively. Axial stiffness was calculated to be 2.68 MN/m based on the slope of the initial part of the curve in the elastic zone. Also, the average skin friction was 19.65 kN/m2.

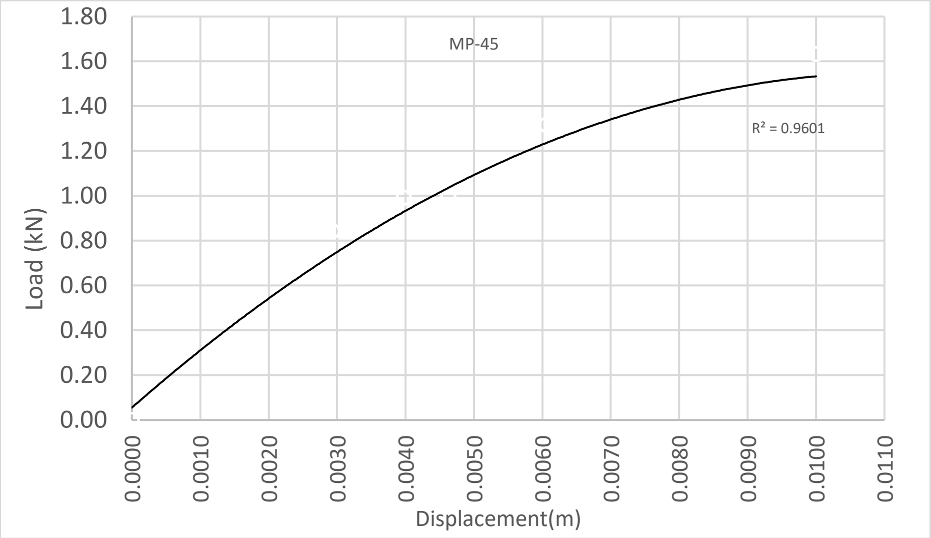

Fig. 4.12-Load vs. Settlement (MP-45)

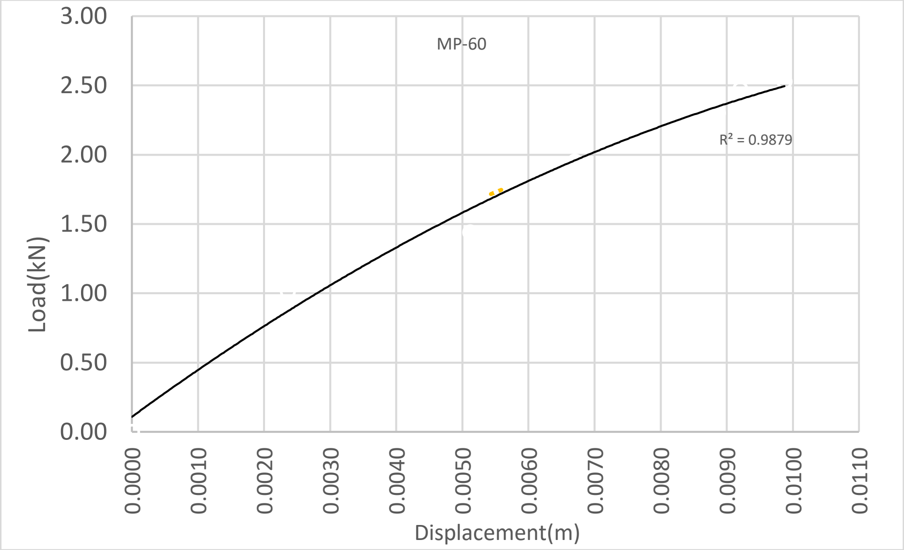

Fig. 4.13-Load vs. Settlement (MP-60)

.

4.4.Micropile as settlement reducer

Single micropiled raft load test

These tests were performed on the single-micropiled raft model. The introduction of the micropile to the raft, as explained below, increased the bearing capacity of the system for any given value of the settlement. The raft was instrumented with a pressure sensor to measure and record the pressure underneath the raft; also, two LVDTs were mounted on a bracket touching the top surface of the raft to calculate the settlement. The total force applied to the model was measured by means of an S-load cell. The micropile model had a pressure sensor on the toe and a strain gauge on the top to measure the force magnitude at these two points.

sMPR-30

The recorded data of testing the single-piled MPR in the sand with a relative density of 30% has been depicted in the form of a plot below (Fig. 4.14). In the first part of the loading process, where the soil under the foundation is still in the elastic zone, as the total force increases, the micropile, and the raft follow the same pattern. Once the total load exceeds the elastic zone, the pressure under the raft levels off, and the additional force is taken by the micropile alone.

The failure point of the single micropile test in the sand with the relative density of Dr=30% was 1.75 kN. The linear part of the curves was used to calculate the axial stiffness. It was calculated to be 3 MN/m.

sMPR-45

In the plot below, the recorded data of testing the MPR in the sand with 45% relative density have been shown. (Fig. 4.15). In the first part of the loading process, where the soil under the foundation is still in the elastic zone, as the total force increases the micropile and the raft follow the same pattern with different steepness. Once the total load goes beyond the elastic zone the pressure under the raft levels off, and the additional force is taken by the micropile alone.

The failure point of the single micropile test in the sand with the relative density of Dr=45% was 2.00 kN. The linear part of the curves was used to calculate the axial stiffness. It was calculated to be 3.5 MN/m.

sMPR-60

Following is a plot showing the data recorded from testing the single-piled MPR in the sand with a relative density of 60% (Fig. 4.16). In the first part of the loading process, where the soil under the foundation is still in the elastic zone, as the total force increases, the micropile, and the raft follow the same pattern with different steepness. Once the total load exceeds the elastic zone, the pressure under the raft levels off, and the additional force is taken by the micropile alone.

The failure point of the single micropile test in the sand with the relative density of Dr=60%

was 2.25 kN. The linear part of the curves was used to calculate the axial stiffness. It was calculated to be 4 MN/m.

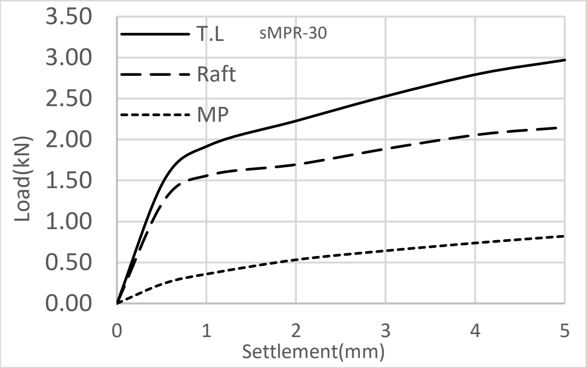

Fig. 4.14-Load-settlement single micropiled raft (Dr=30%)

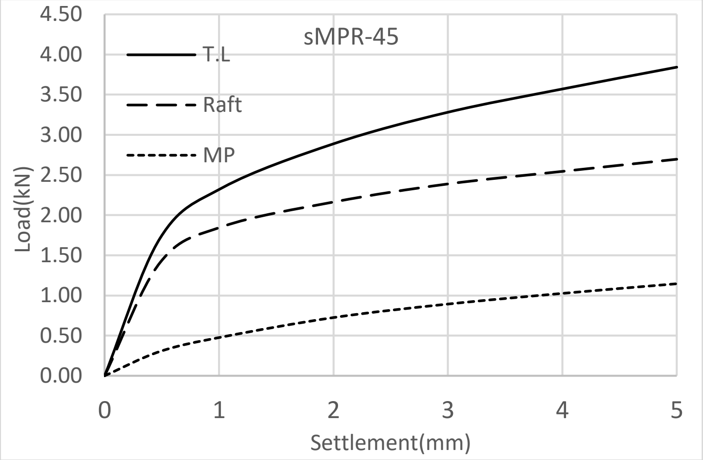

Fig. 4.15-Load-settlement single micropiled raft (Dr=45%)

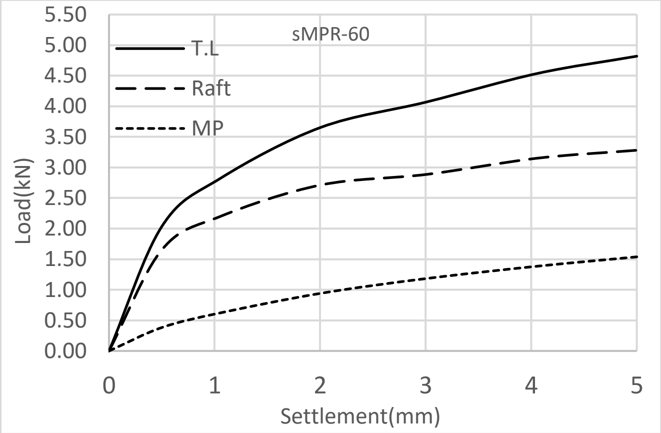

Fig. 4.16-Load-settlement single micropiled raft (Dr=60%)

4.5.Four-micropiled Rafts

Due to the large size of the model with four micropiles (with a diameter of 2.54 cm), it was decided the capacity of the actuator was not apt to carry on the tests. Therefore, two smaller models were built with smaller micropiles (Día=1.58cm, L=50cm) and with rafts size corresponding to s/d=3 and s/d=4 (Fig. 4.17).

These two models were equipped with a pressure sensor in the raft to measure the pressure underneath the raft. Three strain gauges were installed on two micropiles (PVC rods) to measure the axial force at the top, midpoint, and toe of the micropiles. The models were jacked into the sand to further replicate the effects of grout on the prototype models. As before, the total force applied on the models was measured by a S-load cell, and due to having more than a few instruments two DAQ systems along two PCs were used (Fig. 4.18) to accommodate all the measuring devices i.e., two LVDTs, a Load cell, a pressure sensor, and seven strain gauges.

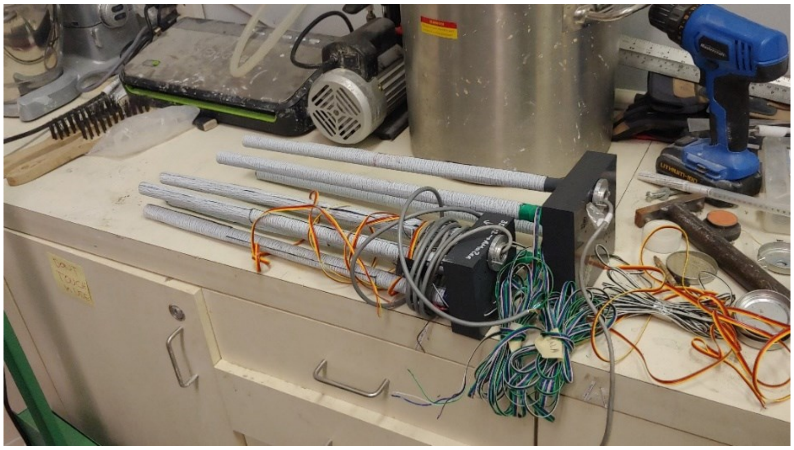

Fig. 4.17-4 Micropiled-rafts (spacings of 3d (left)and 4d(right))

Fig. 4.18- Two DAQs and three power supplies were used
to conduct the measurements

A. Four micropiled raft load test (Spacing=3D)

4MP-3d-30%

The recorded data of testing the four micropiled MPR in the sand with a relative density of 30% has been represented in the form of a plot below (Fig. 4.19). In the first part of the loading process, where the soil under the foundation is still in the elastic zone as the total force increases the micropile and the raft follow the same path with different steepness. Once the total load exceeds the elastic zone, the pressure under the raft levels off, and the additional force was taken by the micropile alone.

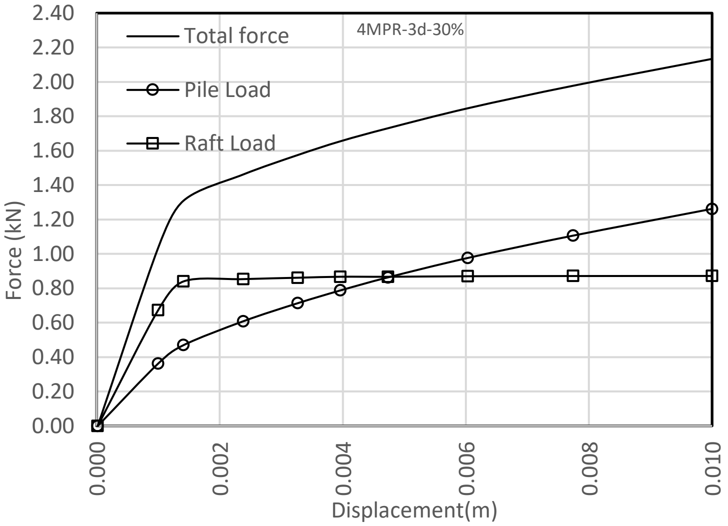

Fig. 4.19-Load vs Settlement (4 Micropiled-raft, s/d=3, Dr=30%)

Comparing the load-settlement behavior of this model against the unpiled raft (Fig. 4.5), it is evident that the introduction of the micropiles has increased the average bearing capacity by 2.75 times. The bearing capacity of the MPR based on the s=0.1d law is calculated as 1.4 kN and the axial stiffness as 3.40 MN/m.

4MP-3d-45%

The recorded data of testing the four micropiled MPR in the medium-dense sand (relative density of 45%) has been depicted in the form of a plot below (Fig. 4.20). In the first part of the loading process, where the soil under the foundation is still in the elastic zone, as the total force increases, the micropile, and the raft follow the same pattern with different steepness. Once the total load exceeds the elastic zone the pressure under the raft levels off and the additional force was taken by the micropile alone.

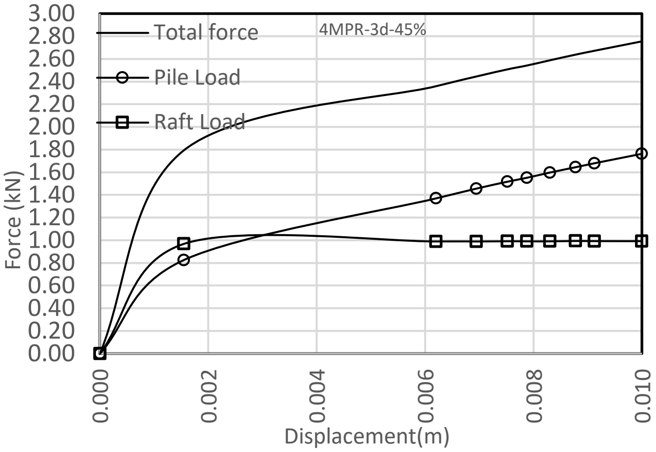

Fig. 4.20-Load vs Settlement (4 Micropiled-raft, s/d=3, Dr=45%)

Comparing the raft alone with the four-micropiled raft (Fig. 4.6), it is demonstrated that an increase of almost 2.5 times in the bearing capacity of the foundation has been gained by the inclusion of four micropiles into the foundation. The bearing capacity of the MPR based on the s=0.1d law is calculated as 1.80 kN and the axial stiffness as 3.70 MN/m.

4MP-3d-60%

The recorded data of testing the four micropiled MPR in the sand with a relative density of 60% has been depicted in the form of a plot below (Fig. 4.21). In the first part of the loading process, where the soil under the foundation is still in the elastic zone, as the total force increases the micropile and the raft follow the same pattern with different steepness. The micropile alone takes up the extra load once the total load exceeds the elastic zone.

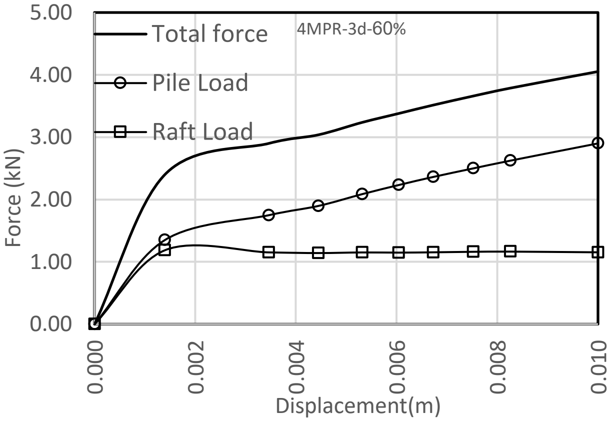

Fig. 4.21-Load vs Settlement (4 Micropiled-raft, s/d=3, Dr=60%)

Comparing the raft alone and the four-micropiled raft in the graph presented before (Fig. 4.7) demonstrated that an increase of almost 2.6 times in the bearing capacity of the foundation had been obtained by introducing four micropiles into the foundation. The bearing capacity of the MPR based on the s=0.1d law is calculated as 2.50 kN and the axial stiffness as 4.90 MN/m.

B. Four micropiled raft load test (Spacing=4D)

4MP-4d-30%

In the following plot, the test results of testing one pile of MPR (s/d=4) with a relative density of 30% are shown. (Fig. 4.22). In the first part of the loading process, where the soil under the foundation is still in the elastic zone, as the total force increases, the micropile, and the raft follow the same pattern with different steepness. Once the total load exceeds the elastic zone the pressure under the raft levels off, and the additional force was taken by the micropile alone.

Comparing the unpiled raft (R-12.5-30%) and four-micropiled raft in the graph below demonstrated that an increase of almost 2.7 times in the bearing capacity of the foundation has been obtained by introducing four micropiles into the foundation. The bearing capacity of the MPR based on the s=0.1d law is calculated as 1.70 kN and the axial stiffness as 3.50 MN/m.

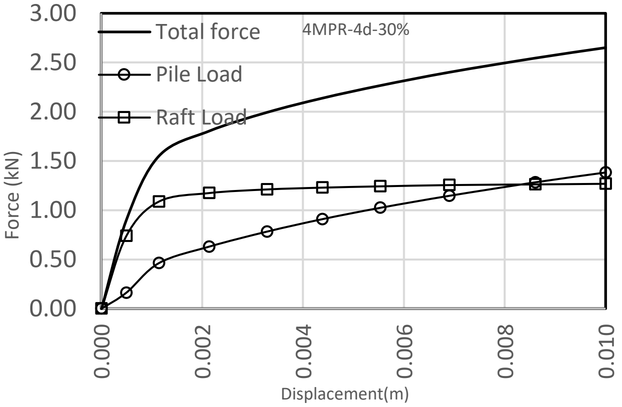

Fig. 4.22-Load vs Settlement (4 Micropiled-raft, s/d=4, Dr=30%)

4M-4d-45%

The data recorded during the testing of the four micropiled MPRs in the sand with a relative density of 60% is depicted in the plot below (Fig. 4.23). In the first part of the loading process, where the soil under the foundation is still in the elastic zone, as the total force increases, the micropile, and the raft follow the same pattern with different steepness. By the time the total load exceeds the elastic zone, the pressure under the raft level off, and the additional force was taken solely by the micropile.

Comparing the raft alone (unpiled) and the four-micropiled raft in the graph above confirmed that a rise of almost 2.33 times in the bearing capacity of the foundation has been obtained by introducing micropiles into the foundation. The bearing capacity of the MPR based on the s=0.1d law is calculated as 2 kN and the axial stiffness as 3.75 MN/m.

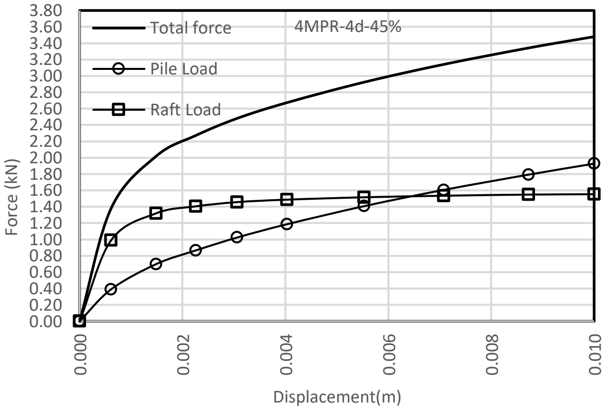

Fig. 4.23--Load vs Settlement (4 Micropiled-raft, s/d=4, Dr=45%)

4MP-4d-60%

The recorded data of testing the four micropiled MPR in the sand with a relative density of 60% has been depicted in the form of a plot below (Fig. 4.24). As the load increases, in the first part of the loading process, where the soil under the foundation is still in the elastic zone, the micropile and the raft follow the same pattern but with different steepness Once the total load exceeds the elastic zone, the pressure under the raft levels off and the additional force was taken by the micropile alone. Comparing the raft alone and the four-micropiled raft in the preceding graph demonstrated that an increase of almost 2.6 times in the bearing capacity of the foundation has been obtained by intruding four micropiles into the foundation. The bearing capacity of the MPR based on the s=0.1d law is calculated as 2.60 kN and the axial stiffness as 5.00 MN/m.

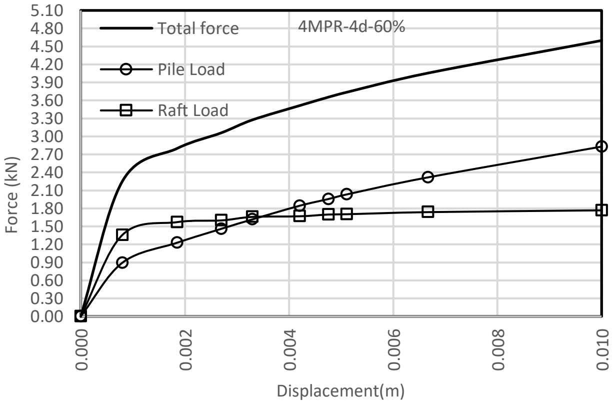

Fig. 4.24--Load vs Settlement (4 Micropiled-raft, s/d=4, Dr=60%)

4.6.Discussion of the results

Tests were carried out on different PVC models in the previous stage. These models included: single micropiles, unpiled rafts, and micropiled-rafts with s/d=3 and s/d =4. In this section, all the data gathered during the experiments were collected. Calculations were carried out to convert the raw data into the forms of tables and charts, which could be easily understood and compared.

In this chapter, the effects of two parameters on the foundation's performance and load-sharing mechanism in the model scale have been studied: soil relative density (Dr) and micropile diameter to the spacing ratios. In Chapter 7, however, the effects of raft thickness will also be added to the two parameters mentioned above.

A. Improvements in bearing capacity

This section compares the micropiled rafts against the unpiled equivalent rafts to evaluate the possible enhancement in the bearing capacity. The bearing capacity of all PVC models, including the single-micropiled raft and two four-micropiled rafts (s/d=3 & s/d=4), have been plotted along with the unpiled versions to demonstrate the differences.

The charts in (Fig. 4.25) show that the single-micropiled raft model gained 20%, 35%, and 40% more bearing capacity than the unpiled equivalent in loose, medium-dense, and dense sand, respectively.

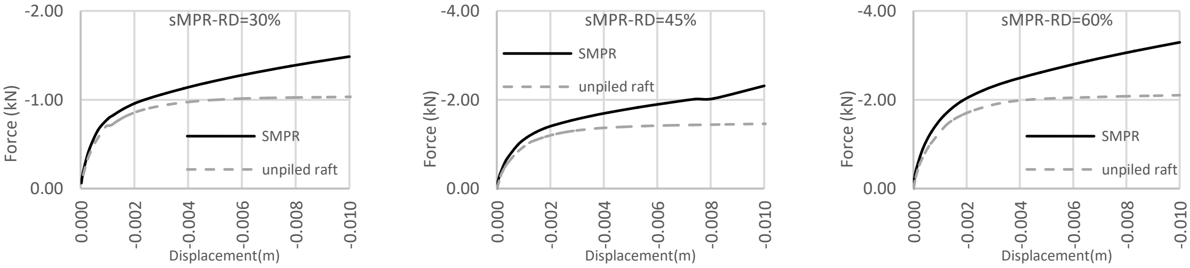

Fig. 4.25-Load settlement of **SMPR** raft vs unpiled raft (Dr=30,45,60%)

Two four-micropiled raft models (s/d=3 & s/d =4) were also put under test in three different relative densities of sand (D_r=30,45&60%). The resulting data has been compared against the unpiled equivalent rafts in Fig. 4.26.

The model with the spacing-to-diameter ratio of 3 saw a significant increase in the bearing capacity of the foundation versus the unpiled version. For loose sand (Dr=30%), at the settlements of 5 and 10 mm, this increment varied between 1.75 and 2.39 times larger. This growth ranged from 2.34 to 3.01 times in the dense sand and at the same settlement values. As expected, the medium-dense sand demonstrated the enhancement values between the loose and dense sand (1.95 times at 5 mm of settlement and 2.57 times at 10 mm).

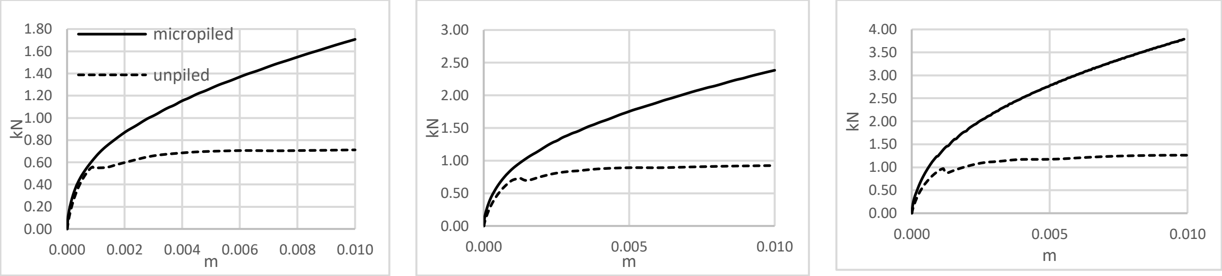

Fig. 4.26-Load settlement of Micropiled raft vs unpiled raft (s/d=3, Dr=30,45,60%)

Comparatively to the unpiled version, the MPR with a spacing-to-diameter ratio of 4 has a higher bearing capacity. This increase varied between 1.87 and 2.24-fold for loose sand (Dr=30%) at settlements of 5 and 10 mm~~.~~ In the dense sand and at the same settlement values, this rise ranged from 1.80 to 2.21 times. As anticipated, the medium-dense sand had the enhancement values between the loose and dense sands (1.80 times at 5 mm of settlement and 2.26 times at 10 mm).

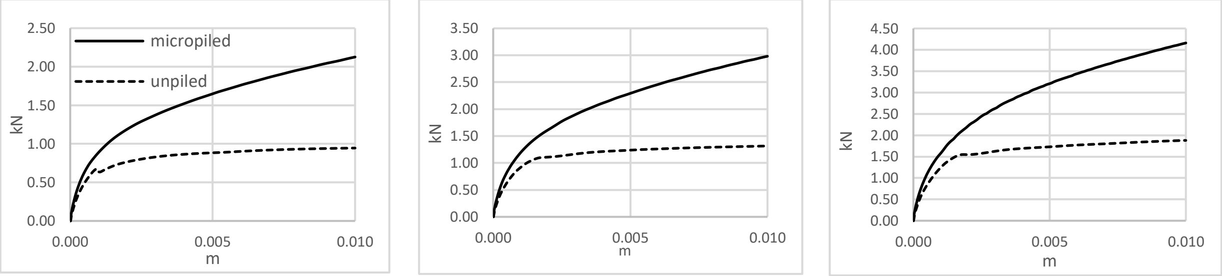

Fig. 4.27-Load settlement of Micropiled raft vs unpiled raft (s/d=4, Dr=30,45,60%)

B. Effects of relative density of the sand

The effects of different relative densities on the bearing capacity of MPRs as well as the load-sharing mechanism between the components were studied during the experimental tests. The figures shown here depict changes in the load taken by the sMPR and the MPR models. In the single-micropiled model (sMPR) (Fig. 4.30), the difference in bearing capacity of the model in the dense and loose sand is about 220%.

At S/d=3 for the MPR model, there was a 200 percent increase between loose and dense sand due to the higher density of the sand (Fig. 4.28). At the spacing-to-diameter ratio of 4, this number is slightly less, around 176%. In both cases, s/d=3 and s/d =4, the medium-dense sand results stand in between the D_r=30 and D_r=60% (Fig. 4.29).

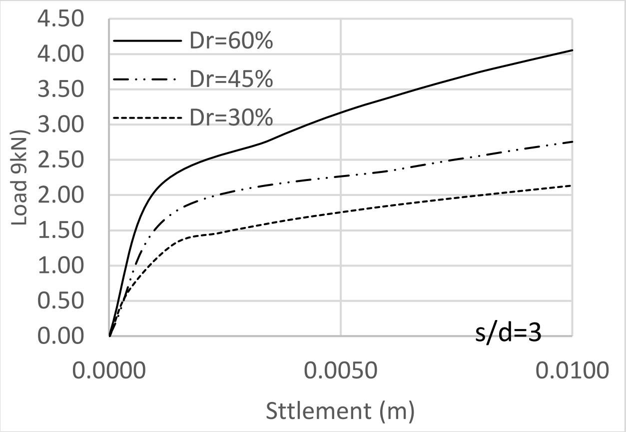

Fig. 4.28-effect of sand relative density on the load settlement behavior of the four-micropiled-raft model (s/d=3)

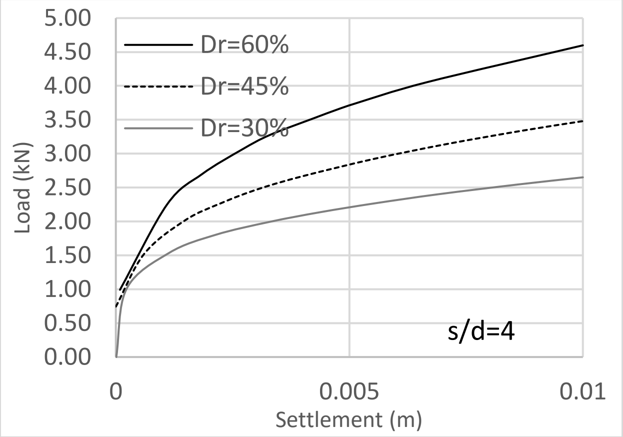

Fig. 4.29-effect of sand relative density on the load settlement behavior of the four-micropiled-raft model (s/d=4)

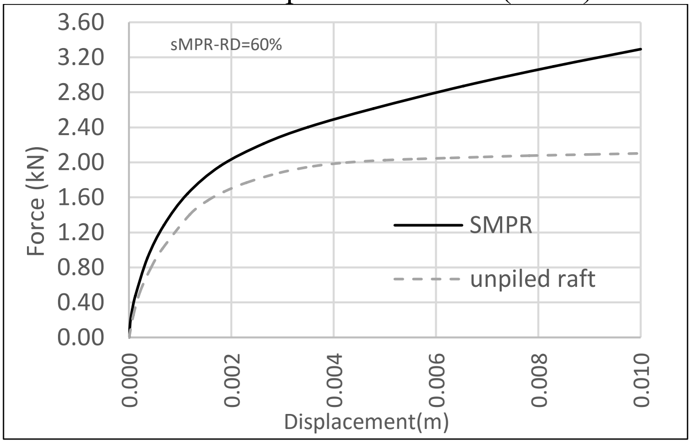

Fig. 4.30-effect of sand relative density on the load settlement behavior of the single-micropiled-raft model

C. *Effects of pile spacing*

The following graph summarizes the load-settlement behavior of the two four-micropiled raft models. As the micropile spacing increases from 3 to 4 d, so does the bearing capacity of the MPRs accordingly. This is consistent with what other researchers, including Sinha (2013) and Alnuaim (2.14), witnessed in their studies. The parametric study further investigated this behavior by considering other spacing ratios of 5,6, and 7 with the real-sized numerical prototype models.

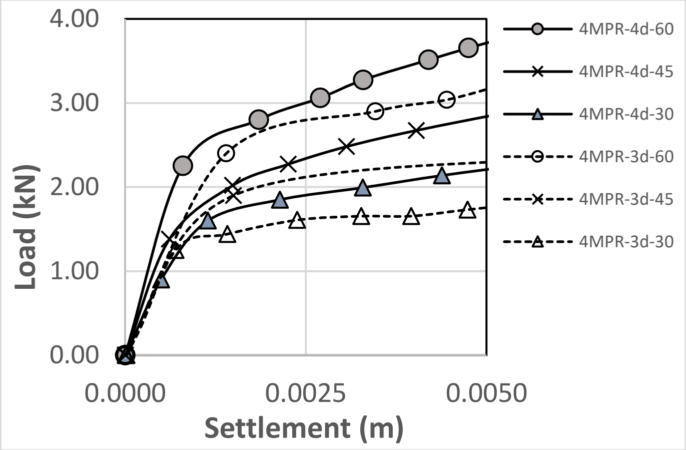

Fig. 4.31-Comparison of load taken by two four-micropiled rafts with s/d=3 & s/d=4

The maximum bending moment and contact pressure, both of which are impacted by the spacing, were investigated using a pressure sensor and a strain gauge bound underneath the raft.

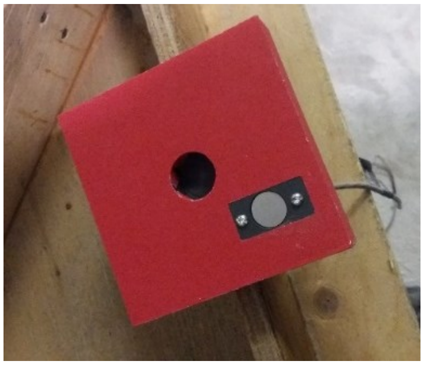

Fig. 4.32- Pressure sensor underneath the raft
(before being covered by sandpaper)

.

It is shown in the charts (Fig. 4.33 & Fig. 4.34) that the bending moment at the bottom of the raft increases almost linearly with the settlement. When the bending moment at the center of the raft case is compared to that of the raft within the MPR, it is evident that the MPR foundation experienced higher moments.

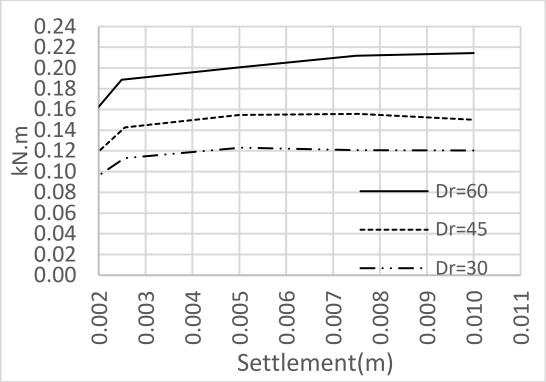

Fig. 4.33-Moment underneath the unpiled raft (s/d=3)

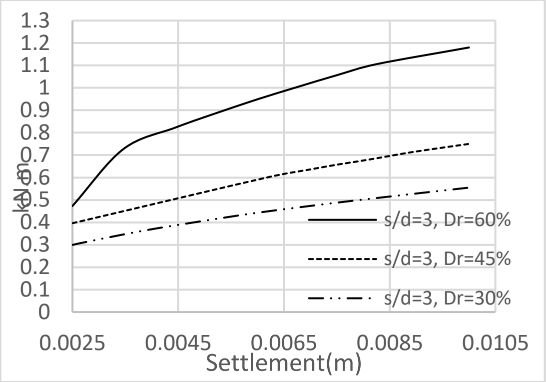

Fig. 4.34-Moment underneath the MPR (s/d=3)

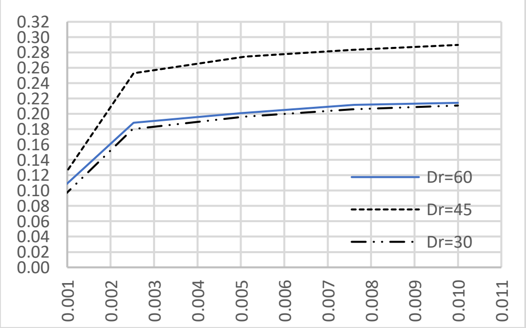

Fig. 4.35-. Moment underneath the unpiled raft (s/d=4)

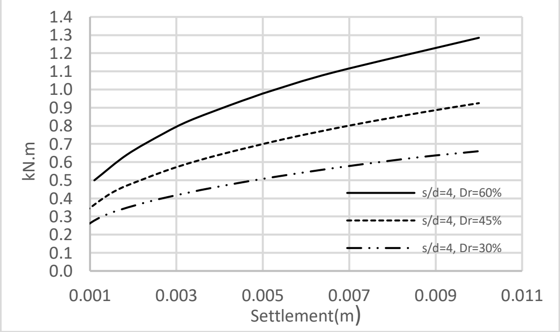

Fig. 4.36-Moment underneath the MPR (s/d=4)

The presence of the micropiles, as can be deduced from the graphs (Fig. 4.37 and Fig. 4.38), decreased the contact pressure underneath the raft by 25% for the dense sand, 20% for the medium-dense and loose sand in the case with s/d=3. Micropiles also managed to lower the contact pressure beneath the raft by 25% for dense sand and 20% for medium-dense and loose sand in the case of MPR with s/d=4 (Fig. 4.39 & Fig. 4.40).

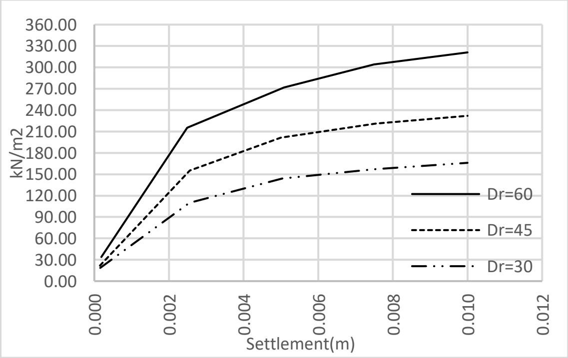

Fig. 4.37-Pressure underneath the unpiled raft (s/d=3)

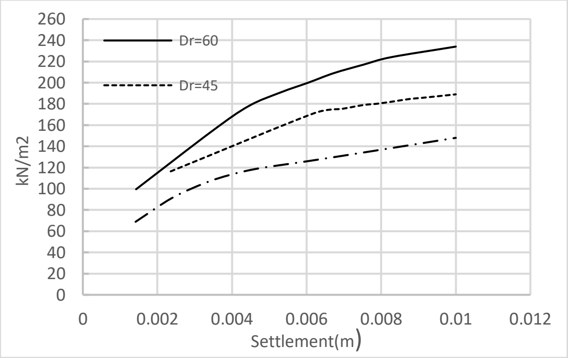

Fig. 4.38-Pressure underneath the raft (MPR, s/d=3)

.

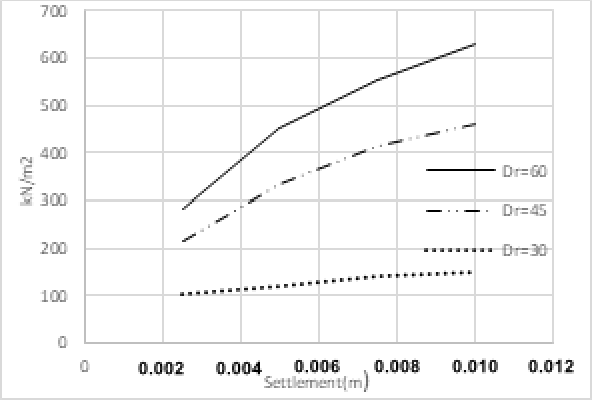

Fig. 4.39-Pressure underneath the unpiled raft (s/d=4)

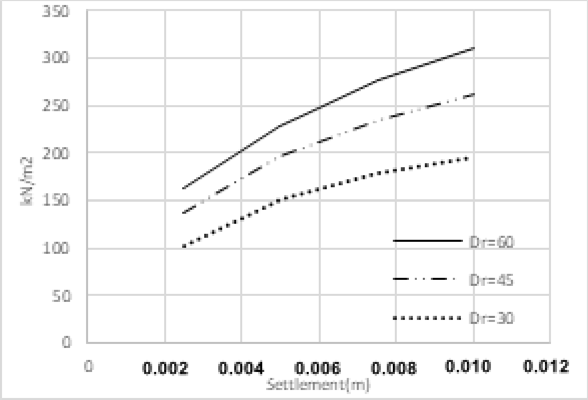

Fig. 4.40-Pressure underneath the raft (MPR, s/d=4)

D. Load sharing between the components of the MPR

The measuring devices were responsible for the measurement of the loads and displacement as well as the strain at the specific locations of the MPR model. The total load was measured by a S-Load cell, and the strain gauges installed at the said locations were used to quantify the value of the total load on top of the micropiles as well as the tip.

For s/d=3, the micropiles take the least proportion of the load in the loose sand, leaving the raft with a larger proportion of the total load to bear. As the sand density increases, so does the share of the micropiles of the total load. For example, it is shown in the loose sand (Fig. 4.41) that the micropiles took a maximum of 60% of the total load, whereas, in the dense sand, this number reaches 72%.

In the case of s/d=4, the micropiles bear the least load in the loose sand, thus the raft got to carry a greater proportion of the total load. Increasing sand density results in an increase in micropile share. This is because the higher friction angle of the denser sand provides higher skin friction. For example, in loose sand (Fig. 4.44), micropiles carry 52 percent of the total load at the maximum value of the settlement, whereas in dense sand, this number rises to 60 percent (Fig. 4.46). As shown, the load share of the micropiles for the MPRs with the spacing-to-diameter of 4 is smaller than MPRs with s/d of 3.

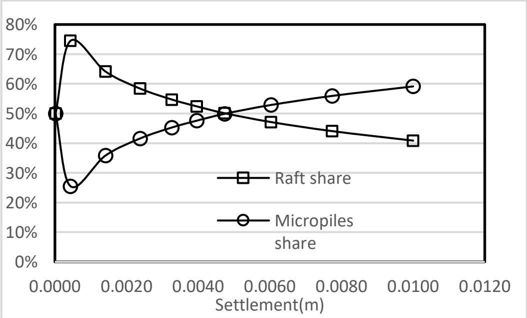

Fig. 4.41-Load sharing between the micropiles and raft (s/d=3, Dr=30%)

.

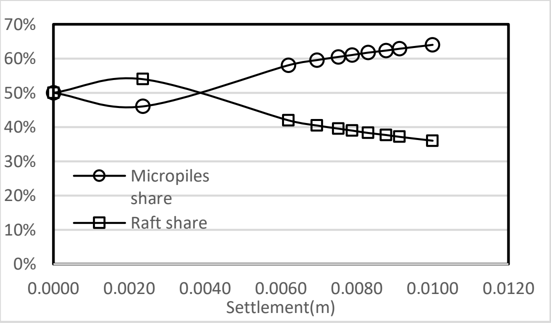

Fig. 4.42Load sharing between the micropiles and raft (s/d=3, Dr=45%)

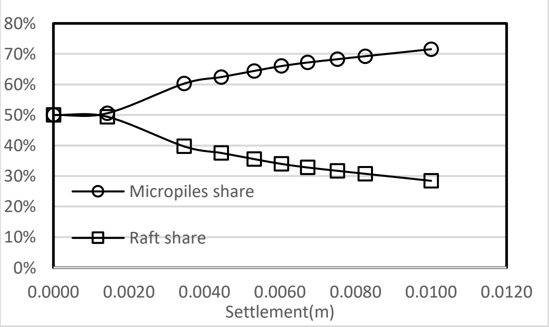

Fig. 4.43-Load sharing between the micropiles and raft (s/d=3, Dr=60%)

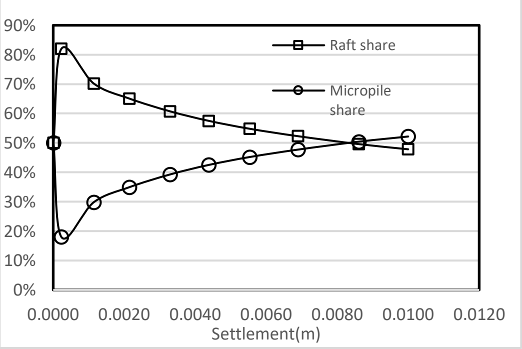

Fig. 4.44--Load sharing between the micropiles and raft (s/d=4, Dr=30%)

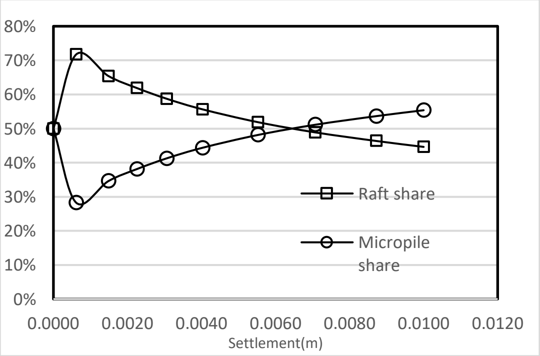

Fig. 4.45--Load sharing between the micropiles and raft (s/d=4, Dr=45%)

.

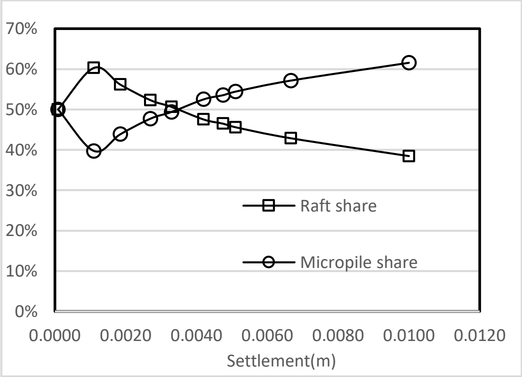

Fig. 4.46--Load sharing between the micropiles and raft (s/d=4, Dr=60%)

The load-sharing mechanism was also investigated for each micropile individually to determine how the load was distributed between the side surface and the toe of the micropile. The following table summarizes the data gathered from the measuring devices.

Total settlement (mm)	Model	Axial load (kN) at			Tip/overall load of micropile
		Top of micropile	Middle of micropile	Toe of micropile	
5	MPR model with s/d=3, in sand with Dr=30	0.138	0.067	0.045	33%
7.5		0.167	0.085	0.052	31%
10		0.191	0.099	0.057	30%
5	MPR model with s/d=3,in sand with Dr=45	0.188	0.099	0.058	31%
7.5		0.232	0.120	0.072	31%
10		0.269	0.140	0.089	33%
5	MPR model with s/d=3,in sand with Dr=60	0.300	0.153	0.107	36%
7.5		0.371	0.197	0.124	34%
10		0.431	0.228	0.138	32%
5	MPR model with s/d=4, in sand with Dr=40	0.150	0.077	0.036	24%
7.5		0.195	0.096	0.043	22%
10		0.226	0.113	0.056	25%
5	MPR model with s/d=4,in sand with Dr=45	0.175	0.091	0.044	25%
7.5		0.216	0.106	0.050	23%
10		0.252	0.126	0.063	25%
5	MPR model with s/d=4,in sand with Dr=60	0.275	0.135	0.058	21%
7.5		0.341	0.171	0.085	25%
10		0.391	0.195	0.102	26%

Table 4.2- Skin resistance and Load at the tip as a percentage of total load carried by each micropile

With s/d=3, the average value is around 32%; however, with s/d =4, the average value is 24%.

This is because, in the smaller spacing ratio, the micropiles are spaced close together causing them to act as a larger unit along with the trapped soil between the micropiles and provide a larger end-bearing capacity.

E. Verification of the experimental results and the findings in the literature review

It was necessary to validate the experimental tests' results; since the rest of the study would be built based on them. A comparison with related studies in the literature review confirms the validity of our experimental results.

The results from unpiled raft foundations were compared with Terzaghi's bearing capacity theory of shallow foundations. A maximum difference of 10% was noted between the actual bearing capacity and the calculated values. For example for the raft R-13 resting on dense sand, the bearing capacity can be computed as follows:

$$Q = q \times N_q + 0.4 \times \gamma \times B \times N_\gamma$$

$\gamma=15.7\ kN/m^3$; $B=0.13m$; $N_\gamma=93$; $N_q=140$

$Q=130.87\ kN/m_2$ *so* $BC=130.87\times0.13\times0.13=\mathbf{2.22}\ kN$

*Bearing capacity from the experiment=**2.00** kN*

Sinha (2013) in his research using 3D FEM models showed that the load share of the raft in piled-raft foundations rises as the spacing between the piles rises. This ratio was calculated and plotted in the graphs below for the two PVC four-micropiled raft models tested in the laboratory (s/d=3 and s/d =4). It is shown that the results of the experimental tests in the sand with the relative density of 30, 45, and 60 are consistent with Sinha's findings.

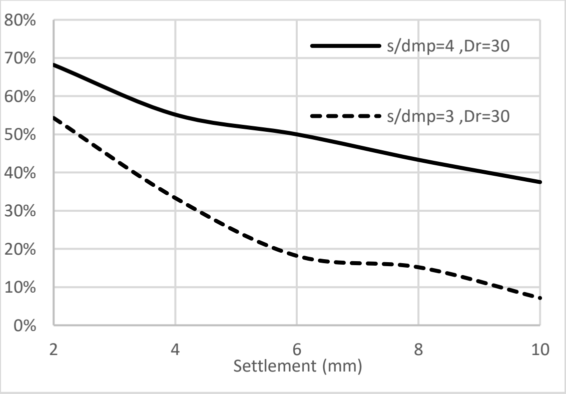

Fig. 4.47-Load share of the raft from the total load applied on the 4 micropiled MPR model (Dr=30%)

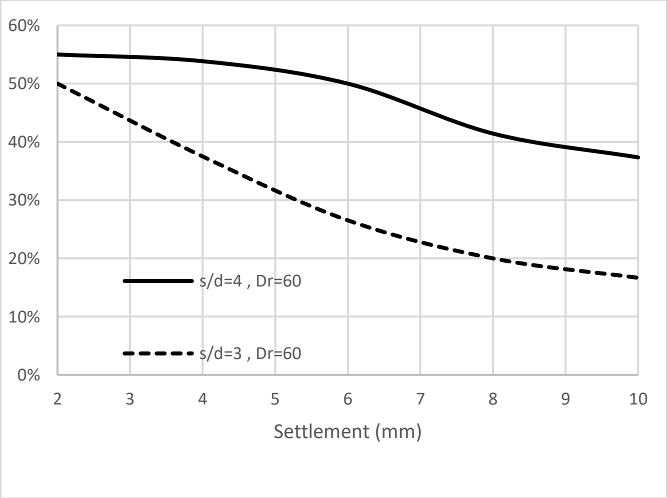

Fig. 4.48-Load share of the raft from the total load applied on the 4 micropiled MPR model (Dr=60%)

Alnauim's research (2014) pointed out the effect of sand bed stiffness on load-sharing behavior. He reports that as the relative density of the soil bed increased, so did the micropile's share of the load leading to a smaller load share for the raft. This is confirmed during our experimental tests (Fig. 4.49).

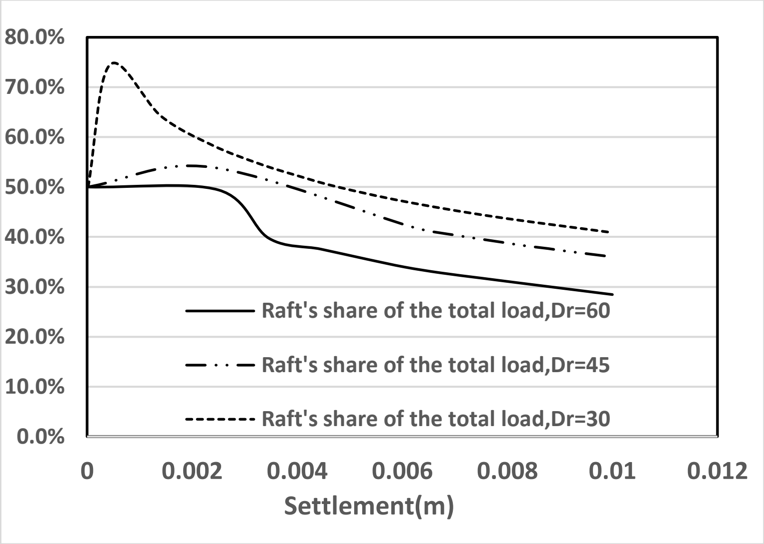

Fig. 4.49- Rafts' share of the total load (s/dmp=3)

CHAPTER 5. NUMERICAL MODELING

5.1.General

A parametric study was carried out using numerical modeling to generalize the data gathered during the experimental tests. During this study, these models were used for evaluating the effects of different parameters, i.e., relative densities, pile spacings, raft stiffness (rigid or semi-flexible) on bearing capacity, overall and differential settlement, as well as the maximum bending moment at the bottom of the raft. As part of the parametric analysis, the PDR method had to be reevaluated for its accuracy in determining the axial stiffness of MPR foundations for preliminary design purposes at the final stage.

Due to the limitations inherent in physical modeling in terms of the model's size and the number of tests that can be conducted in the limited space of the laboratories, it is not always possible to run full-scale tests. During this research, several experimental small-scale tests were carried out. Although these tests may seem enough, they cannot cover all aspects of the possible circumstances and parameters needed to develop an inclusive analytical model.

A numerical model can be used to overcome some of the limitations of laboratory research as there is no limitation for the size of the models and repeatability in FEM modeling. In fact, numerical modeling has been used since 1969, when first used by Brown et al. (1969). Many other researchers, including Hooper (1973), Hain and Lee (1978), Kuwabara F (1989), Randolph M F (1991), and Poulos H G (1993), are only a few to name of those who used numerical modeling.

There are two main types of numerical methods in geotechnical modeling. The continuum mechanics-based approaches, i.e., finite element, finite difference, and boundary element. Discontinuum mechanics-based methods mainly include discrete element modeling. The finite element analysis is just one type of numerical model; it is less restrictive and complementary to the other classes of numerical models.

5.2.Numerical modeling

The numerical modeling was completed in this section by taking several steps. First, the modeling goals were established, and simple models were created on paper. Second, we decided on the theoretical models that would represent the actual condition and behavior of the prototype models. This required an understanding of the core physics and the constitutive behavior, which is noticeable in a model's development through the way the boundary conditions and material properties are introduced. After building the geometry of the models, they were loaded by placing a concentrated constant displacement at the set position, depending on the type of the models (see Fig. 5.4 & Fig. 5.5). Next, the numerical models were analyzed by the numerical analysis software. The output data of the numerical analysis was gathered and fed into the analysis programs to establish the possible relationship between the MPR elements. Finally, the outputs were presented in the next chapter in the form of charts and tabulated data that could be understood easily.

5.3. Building the geometry of the models

PLAXIS 3D (PLAXIS 3D connect edition, Ver 21) was used to create the 3D models using suitable types of elements and mesh sizes. Plaxis is a computer program that performs finite element analyses (FEA) within the field of geotechnical engineering. It includes geometry creation tools and automated settings to allow geotechnical problems to be analyzed. It is a software tool to perform accurate three-dimensional analysis of deformation and stability in geotechnical engineering and rock mechanics. This software has been widely used by many other authors for investigation of a similar structure (Piled-rafts) (Amornfa, et al., 2022) and (Sulaiman, et al., 2021). In the following subsections, the process of building the models and performing the analyses are described.

A. Defining the geometry of the models

Building two types of models were required to understand the effects of placing a point load at different locations on the micropiled-raft foundation performance. The PDR method uses an equation for calculating the raft stiffness that is independent of the raft's thickness. We planned to evaluate the performance of MPRs for the cases where the load applied on the raft is in the form of a concentrated load.

Two cases were assumed for the locations of the concentrated load: case *A* where the load is exerted at the centroid of a micropile group (4 micropiles), an area forming a rectangular with no micropile underneath the load, and case *B* (coaxial loading), in which the load is coaxial with a micropile.

Since the MPR with load A would have created a significant workload for the computers, only a quarter of the models were built. Plaxis can simulate and perform the calculation by using symmetrical properties. Thirty models were built in this category, with the difference being in the thickness of rafts (rigid and semi-flexible), varying relative densities of the sand (Dr=30%,45%, and 60%), and micropiles spacings ratios of 3,4,5,6 and 7. Another thirty identical equivalent unpiled versions were also analyzed to be used as the benchmarks totaling 60 models in this category (Fig. 5.4).

Fig. 5.5 demonstrates a schematic top view of the MPR with a concentric load. Here, unlike in the previous situation, the load sits on the point of the raft supported by a micropile underneath. Due to its location, this micropile is expected to be subjected to the largest proportion of the load taken by all the micropiles. During the analyses, these two models had to be slightly modified for each analysis to accommodate the different values of raft stiffness,sand stiffness, and micropile spacing ratios.

The piled raft was constructed by attaching the micropiles to the bottom surface of the raft, which was modeled as a plate. Sand mass was created as a block, and the defined MPR models were placed on the top surface of the soil block. The software automatically created the boundary condition of the soil mass (Plaxis). On the sides of the soil volume, the lateral movement was restricted in both directions, and at the bottom, it was restricted as it is assumed that the whole model sits on a rock bed.

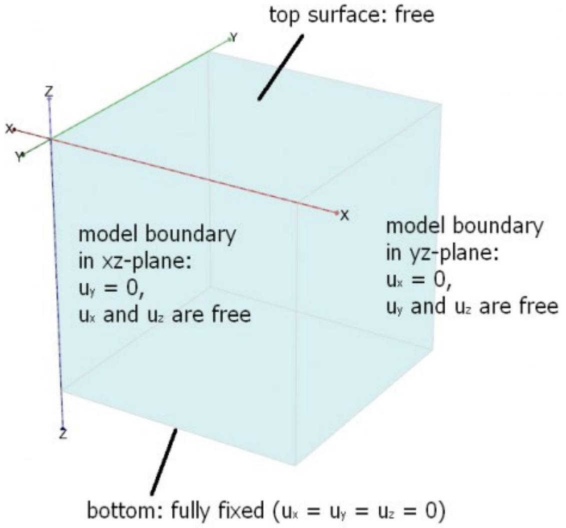

Fig. 5.1-boundary condition of the soil mass

B. Mesh

PLAXIS 3D generates finite element meshes automatically. The soil stratigraphy and all structural objects, loads, and boundary conditions are taken into account during the mesh generation process.

The soil volume in the PLAXIS program is modeled by means of 10-node tetrahedral elements. The interpolation functions, their derivatives, and the numerical integration of this type of element are described in the Plaxis manual. Tetrahedral elements are capable of being unstructured and reshaped to fit arbitrary geometries.

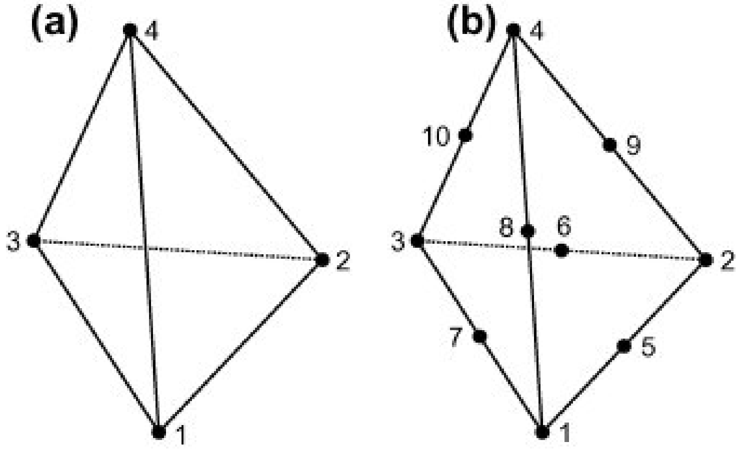

Fig. 5.2-Tetrahedral elements (used in the meshing process)

C. Constitutive model

Numerical methods use constitutive models to represent the behavior of materials. These constitutive models should be able to simulate the soil behavior under loading conditions and the properties of structure models with accuracy.

Although Elasticity constitutive models may seem convenient for modeling most materials, the nonlinearity in soil behavior is usually an indication of plasticity: permanent, irrecoverable changes in the fabric of the soil. There is no generally accepted soil model; however, simplified failure criteria such as Mohr-Coulomb are widely used in practice. This model usually is appropriate, especially when the failure happens in drained conditions. There are other constitutive models available for soils, e.g., Cam Clay, but the Mohr-Coulomb model is suitable for undrained soft soils as indicated by other researchers, e.g., Alnuaim (2014).

The Mohr-Coulomb model is an elastic-perfectly plastic model frequently used to model soil behavior. In the principal stress space, the Mohr-Coulomb yield surface defines three limit functions that form a hexagonal cone. This model is straightforward and applicable to three-dimensional stress space, requiring only two strength parameters to describe plastic behavior.

There are five input parameters in the Linear-Elastic Perfectly-Plastic Mohr-Coulomb model: Young's modulus E and Poisson's ratio ν for soil elasticity; the cohesion c, friction angle phi (φ), and dilatancy angle psi (ψ) for soil plasticity. Table 5.1 and 5.2 list the physical properties of the soil and the PVC and concrete materials representing the laboratory and prototype models (Dr=30,45,60%).

Considering the mechanical properties of concrete, the raft and micropile behavior were simulated using the linear elastic model. Although the Linear Elastic model is unsuitable for modeling soil, it can be used to model stiff volumes like concrete structures or intact rock formations. Other researchers such as Vakili (2015), Alnuaim (2014), and Sinha (2013) have reported that the linear elastic model provided adequate performance for modeling the constitutive behavior of concrete.

Parameter	Sand (D_r=30%)	Sand (D_r=45%)	Sand (D_r=60%)
Unit weight (kN/m3)	*14.81*	*15.03*	*15.9*
Friction angle (φ)	*33°*	*35°*	*37°*
Modulus of elasticity, E	*18e3*	*22e3*	*26.3e3*
Poisson ratio (ν)	*0.25*	*0.27*	*0.3*

Table 5.1-Input soil parameter for FE Analysis (soil)

.

Parameter	PVC models	Prototype models (Concrete)
Unit weight (kN/m3)	*145*	*24.8*
Modulus of elasticity, E	*30e6*	*30e9*
Poisson ratio(ν)	*0.3*	*0.3*

Table 5.2-Input parameter for FE Analysis (Prototype)

.

$$Number\ of\ cases\ (Model\ A - Piled)$$

$$= 5\left(\frac{s}{d_{mp}} = 3{,}4{,}5{,}6{,}7\right) \times 2(Raft\ stiffiness, Rigid\ or\ Flexible)$$

$$\times\ 3(Dr = 30, 45\ and\ 60) = 30$$

$$Number\ of\ cases\ (Model\ A - unPiled)$$

$$= 5\left(\frac{s}{d_{mp}} = 3{,}4{,}5{,}6{,}7\right) \times 2(Raft\ stiffiness, Rigid\ or\ Flexible)$$

$$\times\ 3(Dr = 30, 45\ \&\ 60) = 30$$

$$Number\ of\ cases\ (Model\ B - Piled)$$

$$= 5\left(\frac{s}{d_{mp}} = 3{,}4{,}5{,}6{,}7\right) \times 2(Raft\ stiffiness, Rigid\ or\ Flexible)$$

$$\times\ 3(Dr = 30, 45\ and\ 60) = 30$$

$$Number\ of\ cases\ (Model\ B - unPiled)$$

$$= 5\left(\frac{s}{d_{mp}} = 3{,}4{,}5{,}6{,}7\right) \times 2(Raft\ stiffiness, Rigid\ or\ Flexible)$$

$$\times\ 3(Dr = 30, 45\ \&\ 60) = 30$$

Table 5.3_Number of FEM models built in Plaxis

..

Test code	Dr	Raft size	No of piles	Micropiles (Length/dia)	Micropiles Spacing	Raft thickness		Type of load
		(m)		(m)		Semi-flexible (m)	Rigid (m)	
1	30%	3.15x3.15	9	10/0.15	3	0.10		A
2	45%	3.15x3.15	9	10/0.15	3	0.10		A
3	60%	3.15x3.15	9	10/0.15	3	0.10		A
4	30%	3.15x3.15			unpiled	0.10		A
5	45%	3.15x3.15			unpiled	0.10		A
6	60%	3.15x3.15			unpiled	0.10		A
7	30%	3.15x3.15	9	10/0.15	3		0.3	A
8	45%	3.15x3.15	9	10/0.15	3		0.3	A
9	60%	3.15x3.15	9	10/0.15	3		0.3	A
10	30%	3.15x3.15			unpiled		0.3	A
11	45%	3.15x3.15			unpiled		0.3	A
12	60%	3.15x3.15			unpiled		0.3	A
13	30%	3.15x3.15	9	10/0.15	4	0.15		A
14	45%	3.15x3.15	9	10/0.15	4	0.15		A
15	60%	3.15x3.15	9	10/0.15	4	0.15		A
16	30%	3.15x3.15			unpiled	0.15		A
17	45%	3.15x3.15			unpiled	0.15		A
18	60%	3.15x3.15			unpiled	0.15		A
19	30%	3.15x3.15	9	10/0.15	4		0.35	A
20	45%	3.15x3.15	9	10/0.15	4		0.35	A
21	60%	3.15x3.15	9	10/0.15	4		0.35	A
22	30%	3.15x3.15			unpiled		0.35	A
23	45%	3.15x3.15			unpiled		0.35	A
24	60%	3.15x3.15			unpiled		0.35	A
25	30%	3.15x3.15	9	10/0.15	5	0.20		A
26	45%	3.15x3.15	9	10/0.15	5	0.20		A
27	60%	3.15x3.15	9	10/0.15	5	0.20		A
28	30%	3.15x3.15			unpiled	0.20		A
29	45%	3.15x3.15			unpiled	0.20		A
30	60%	3.15x3.15			unpiled	0.20		A
31	30%	3.15x3.15	9	10/0.15	5		0.45	A
32	45%	3.15x3.15	9	10/0.15	5		0.45	A

Test code	Dr	Raft size (m)	No of piles	Micropiles (Length/dia) (m)	Micropiles Spacing	Raft thickness		Type of load
						Semi-flexible (m)	Rigid (m)	
33	60%	3.15x3.15	9	10/0.15	5		0.45	A
34	30%	3.15x3.15			unpiled		0.45	A
35	45%	3.15x3.15			unpiled		0.45	A
36	60%	3.15x3.15			unpiled		0.45	A
37	30%	3.15x3.15	9	10/0.15	6	0.25		A
38	45%	3.15x3.15	9	10/0.15	6	0.25		A
39	60%	3.15x3.15	9	10/0.15	6	0.25		A
40	30%	3.15x3.15			unpiled	0.25		A
41	45%	3.15x3.15			unpiled	0.25		A
42	60%	3.15x3.15			unpiled	0.25		A
43	30%	3.15x3.15	9	10/0.15	6		0.55	A
44	45%	3.15x3.15	9	10/0.15	6		0.55	A
45	60%	3.15x3.15	9	10/0.15	**6**		0.55	A
46	30%	3.15x3.15			unpiled		0.55	A
47	45%	3.15x3.15			unpiled		0.55	A
48	60%	3.15x3.15			unpiled		0.55	A
49	30%	3.15x3.15	9	10/0.15	7	0.30		A
50	45%	3.15x3.15	9	10/0.15	7	0.30		A
51	60%	3.15x3.15	9	10/0.15	7	0.30		A
52	30%	3.15x3.15			unpiled	0.30		A
53	45%	3.15x3.15			unpiled	0.30		A
54	60%	3.15x3.15			unpiled	0.30		A
55	30%	3.15x3.15	9	10/0.15	7		0.65	A
56	45%	3.15x3.15	9	10/0.15	7		0.65	A
57	60%	3.15x3.15	9	10/0.15	7		0.65	A
58	30%	3.15x3.15			unpiled		0.65	A
59	45%	3.15x3.15			unpiled		0.65	A
60	60%	3.15x3.15			unpiled		0.65	A

Numerical test program (Under load A).

Test code	Dr	Raft size	No of piles	Micropiles (Length/dia)	Micropiles Spacing	Raft thickness		Type of load
		(m)		(m)		flexible	Rigid	
						(m)	(m)	
61	30%	4.2 x 4.2	16	10/0.15	3	0.10		B
62	45%	4.2 x 4.2	16	10/0.15	3	0.10		B
63	60%	4.2 x 4.2	16	10/0.15	3	0.10		B
64	30%	4.2 x 4.2			unpiled	0.10		B
65	45%	4.2 x 4.2			unpiled	0.10		B
66	60%	4.2 x 4.2			unpiled	0.10		B
67	30%	4.2 x 4.2	16	10/0.15	3		0.3	B
68	45%	4.2 x 4.2	16	10/0.15	3		0.3	B
69	60%	4.2 x 4.2	16	10/0.15	3		0.3	B
70	30%	4.2 x 4.2			unpiled		0.3	B
71	45%	4.2 x 4.2			unpiled		0.3	B
72	60%	4.2 x 4.2			unpiled		0.3	B
73	30%	4.2 x 4.2	16	10/0.15	4	0.15		B
74	45%	4.2 x 4.2	16	10/0.15	4	0.15		B
75	60%	4.2 x 4.2	16	10/0.15	4	0.15		B
76	30%	4.2 x 4.2			unpiled	0.15		B
77	45%	4.2 x 4.2			unpiled	0.15		B
78	60%	4.2 x 4.2			unpiled	0.15		B
79	30%	4.2 x 4.2	16	10/0.15	4		0.35	B
80	45%	4.2 x 4.2	16	10/0.15	4		0.35	B
81	60%	4.2 x 4.2	16	10/0.15	4		0.35	B
82	30%	4.2 x 4.2			unpiled		0.35	B
83	45%	4.2 x 4.2			unpiled		0.35	B
84	60%	4.2 x 4.2			unpiled		0.35	B
85	30%	4.2 x 4.2	16	10/0.15	5	0.20		B
86	45%	4.2 x 4.2	16	10/0.15	5	0.20		B
87	60%	4.2 x 4.2	16	10/0.15	5	0.20		B
88	30%	4.2 x 4.2			unpiled	0.20		B
89	45%	4.2 x 4.2			unpiled	0.20		B
90	60%	4.2 x 4.2			unpiled	0.20		B
91	30%	4.2 x 4.2	16	10/0.15	5		0.45	B
92	45%	4.2 x 4.2	16	10/0.15	5		0.45	B
93	60%	4.2 x 4.2	16	10/0.15	5		0.45	B

Test code	Dr	Raft size (m)	No of piles	Micropiles (Length/dia) (m)	Micropiles Spacing	Raft thickness		Type of load
						flexible (m)	Rigid (m)	
94	30%	4.2 x 4.2			unpiled		0.45	B
95	45%	4.2 x 4.2			unpiled		0.45	B
96	60%	4.2 x 4.2			unpiled		0.45	B
97	30%	4.2 x 4.2	16	10/0.15	6	0.25		B
98	45%	4.2 x 4.2	16	10/0.15	6	0.25		B
99	60%	4.2 x 4.2	16	10/0.15	6	0.25		B
100	30%	4.2 x 4.2			unpiled	0.25		B
101	45%	4.2 x 4.2			unpiled	0.25		B
102	60%	4.2 x 4.2			unpiled	0.25		B
103	30%	4.2 x 4.2	16	10/0.15	6		0.55	B
104	45%	4.2 x 4.2	16	10/0.15	6		0.55	B
105	60%	4.2 x 4.2	16	10/0.15	6		0.55	B
106	30%	4.2 x 4.2			unpiled		0.55	B
107	45%	4.2 x 4.2			unpiled		0.55	B
108	60%	4.2 x 4.2			unpiled		0.55	B
109	30%	4.2 x 4.2	16	10/0.15	7	0.30		B
110	45%	4.2 x 4.2	16	10/0.15	7	0.30		B
111	60%	4.2 x 4.2	16	10/0.15	7	0.30		B
112	30%	4.2 x 4.2			unpiled	0.30		B
113	45%	4.2 x 4.2			unpiled	0.30		B
114	60%	4.2 x 4.2			unpiled	0.30		B
115	30%	4.2 x 4.2	16	10/0.15	7		0.65	B
116	45%	4.2 x 4.2	16	10/0.15	7		0.65	B
117	60%	4.2 x 4.2	16	10/0.15	7		0.65	B
118	30%	4.2 x 4.2			unpiled		0.65	B
119	45%	4.2 x 4.2			unpiled		0.65	B
120	60%	4.2 x 4.2			unpiled		0.65	B

Numerical test program (under load B)

5.4.Calibration of the numerical models

The generated numerical models first had to be calibrated against the actual output; otherwise, the output data would not be reliable for extrapolating the data from the experimental tests. Three FEM replica models of the actual PVC models were built in Plaxis, and the output was compared against that of the experimental test. Some adjustments were applied to the parameter, including R_{int}, until the output values were in good agreement with the actual data. *R_{int} is a parameter that controls the behavior of the interface element. To simulate the interaction between a structure and soil, interface elements are used. Without an interface, the structure and the soil are tied together: no relative displacement (slipping/gapping) is possible between the structure and soil* (Plaxis, manual).

By using an interface, node pairs are created at the interface of structure and soil. From a node pair, one node belongs to the structure, and the other node belongs to the soil. The interaction between these two nodes consists of two elastic-perfectly plastic springs. One elastic-perfectly plastic spring to model the gap displacement and one elastic-perfectly plastic spring to model slip displacement (Plaxis, manual). The following chart (Fig. 5.6) demonstrates one of the comparisons made between the outputs from the FEM modeling and the actual data gathered in the experimental tests. It is shown that there is a good agreement between them.

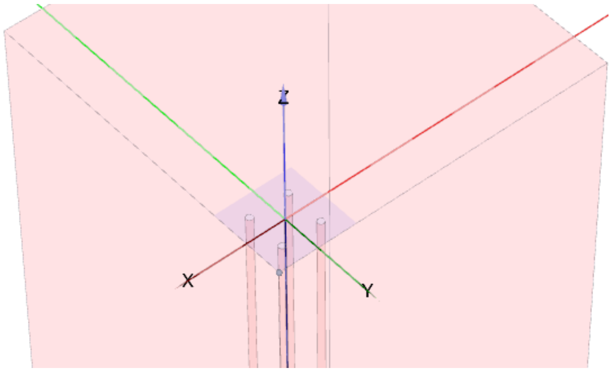

Fig. 5.3- MPR with load type A

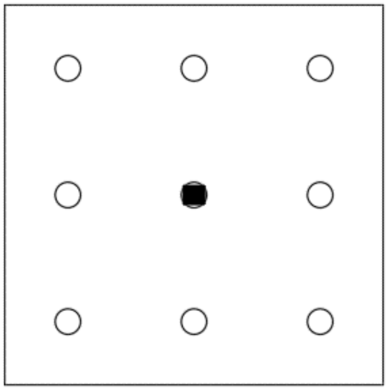

a

Fig. 5.4- MPR with the load at the centroid of a micropile group- Model type A

○ Micropile

□ Load (Constant displacement of 15 cm)

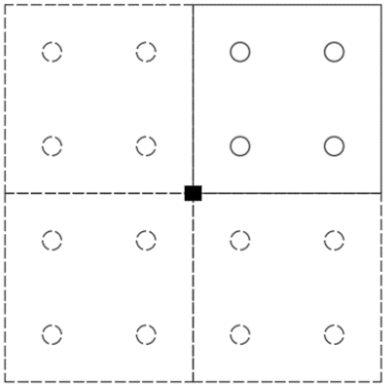

Fig. 5.5- MPR with the coaxial load - Model type B

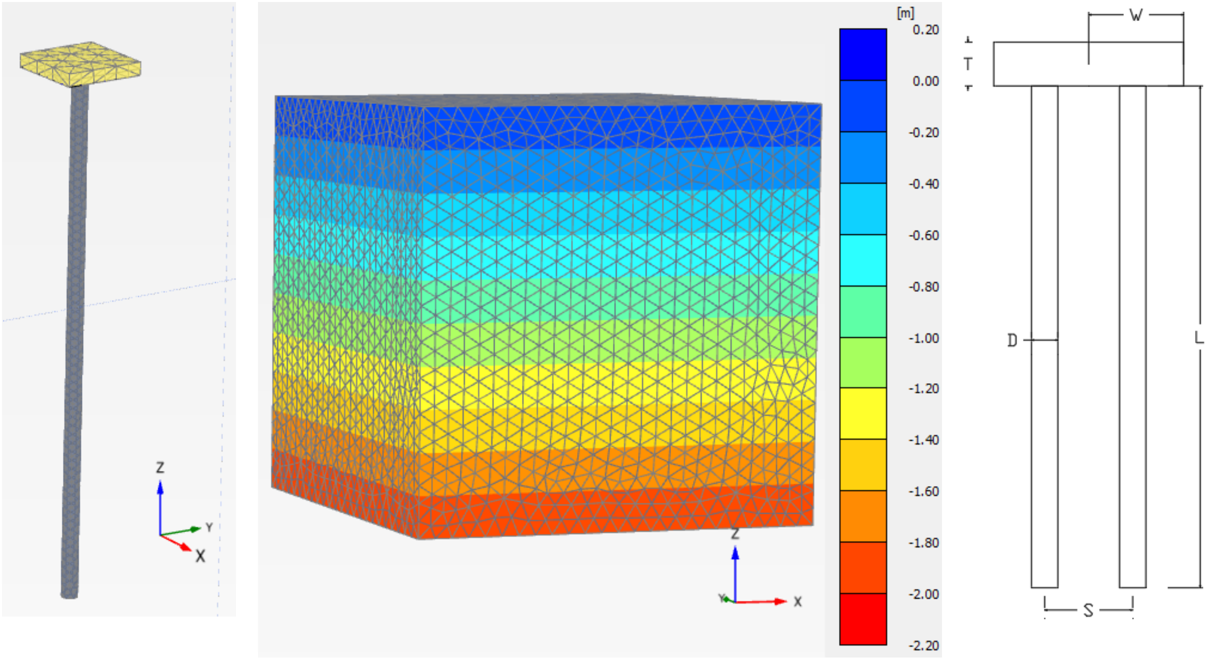

Fig. 5.6-Single-micropiled raft (left) Numerical model and Soil block-FEM duplicate model of the PVC models used in the experimental tests (right)

..

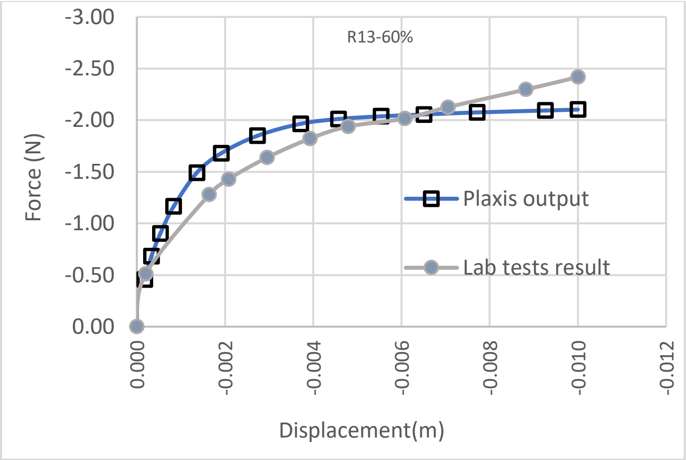

Fig. 5.7-- Comparison between the experimental and numerical models (Unpiled-Raft-13x13cm)-D_r=60%

5.5.Raft thickness (Stiffness)

To investigate the effects of the raft stiffness on the loading-settlement behavior and load-sharing mechanism, two types of rafts were considered in the numerical simulations, i.e., rigid and semi-flexible. In his method (2001), Poulos proposes a series of formulas to evaluate the axial stiffness of a piled-raft foundation. The piled-raft axial stiffness, as demonstrated below, is the function of the stiffness of the raft and the piles along with the soil stiffness.

$$K_{pr} = \frac{K_{pg} + (1 + 2\alpha_{rp})K_r}{1 - (\alpha_{rp}^2(K_r/K_{pg}))}$$

(Equation 5.1)

α is a factor that introduces the interaction between the piles and the raft and is calculated by:

$$\alpha_{rp} = 1 - (\frac{\ln(r_c / r_0)}{\xi})$$

(Equation 5.2)

Where r_c and r_0 are the average radii of pile cap and pile radius, respectively. $\zeta=\ln(r_m/r_0)$;$r_m=2.5\rho(1-\upsilon)L_p$; $\xi=E_{sl}/E_{sb}$; $\rho=Es_{av}/E_{sl}$; $\mu L=[2/(\zeta\lambda)]^{0.5}(L/r_0)$; $\lambda=E_p/G_{sl}$; $\eta=r_b/r_0$; r_b is the radius at pile base; L_p is the pile length; E_{sl} is soil Young's modulus at the pile toe level; E_{sb} is soil Young's modulus below pile tip; E_{sav} is average soil Young's modulus along pile shaft; ν represents soil Poisson's ratio; G_{sl} is soil shear modulus at the pile base level, and E_p is the pile material Young's modulus(Randolph1994). K_{pg} is the stiffness of the pile group and can be calculated using (Fleming et al.,2009).

$$K_{pg} = n^{0.5}k_p$$

(Equation 5.3)

n is the number of piles in the group, and K_p is the stiffness of a single pile and is evaluated using the following equation:

$$K_p := \frac{G_{s1} \cdot r_0 \cdot \left[\frac{4 \cdot \eta}{(1-\nu) \cdot \xi} + \left(\frac{2 \cdot \pi \cdot \rho}{\zeta} \right) \cdot \left(\tanh(\mu L) \cdot \frac{1}{\mu L} \right) \cdot \left(\frac{L}{r_0} \right) \right]}{1 + \left[\left(\frac{4 \cdot \eta}{\pi \cdot \lambda \cdot (1-\nu) \cdot \xi} \right) \cdot \left(\frac{\tanh(\mu L)}{\mu L} \right) \cdot \left(\frac{L}{r_0} \right) \right]}$$

(Equation 5.4)

Raft stiffness can be calculated using the expression suggested by Poulos and Davis in 1974 (Equation 5.5), but this expression does not consider the raft thickness.

$$K_r = 1.05\sqrt{B.W}(\frac{2.G_{sr}}{1-\nu})$$

Equation 5.5

Where: K_r is axial stiffness for the raft foundation; B and W are the width and length of the raft; G_{sr} represents the shear modulus of the soil at a depth of 2B/3, and ν is the soil Poisson's ratio. This equation can be replaced with the following equation, proposed by Horikoshi and Randolph (1997), which takes into account the raft's thickness and produces a more precise output.

$$K_r = 5.57\left(\frac{E_r}{E_s}\right)\frac{(1-\nu_s^2)}{(1-\nu_r^2)}\left(\frac{S_B}{S_L}\right)^{\alpha}\left(\frac{t}{S_L}\right)^3$$

(Equation 5.6)

S_L and S_B are the spacing between micropiles along the length and width of the MPR, respectively. "t" is the thickness of the raft, E_r and ν_r are the modulus of elasticity, and Poisson ratio of the raft, and E_s and ν_s are those of soil.

For the stiffness of the raft (K_r), according to Horikoshi and Randolph (1997), the following classification can be defined: (1) perfectly rigid if $Kr > 1000$; (2) perfectly flexible when $Kr < 0.001$; and (3) semi-flexible if Kr varies between 0.001 and 1000. Our FEM models were built using the following thicknesses of rafts derived from (Equation 5.6).

Spacing	Semi-flexible Raft -Raft thickness (m)	Rigid Raft- Raft thickness (m)
s/d=3	0.10	0.30
s/d=4	0.15	0.35
s/d=5	0.20	0.45
s/d=6	0.25	0.55
s/d=7	0.30	0.65

Table 5.4- Thicknesses of the FEM models

CHAPTER 6. RESULTS OF PARAMETRIC MODELING

6.1.General

The previous chapter explained the process of building the FEM models. As explained two series of models were created, i.e., a model where a 9-micropiled model (A) with a pointed load acting on the raft and coaxial with a micropile. Another model was a non-coaxially loaded model with the point load being applied at the centroid of a micropile group (Model B)consisting of 4 micropiles.

In this chapter, the outputs are presented and discussed. For easier identification of the models, they may be referred to by their code name as defined here:

Loading type (A/B) _Spacing ratio_ flexible or rigid raft_ Relative density of the sand.

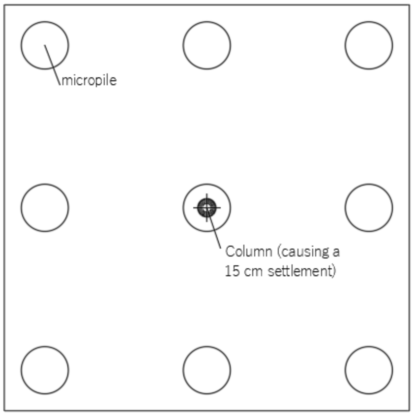

Fig. 6.1- Configuration of the MPs (MPR under a load acting coaxially with a micropile) - Type A

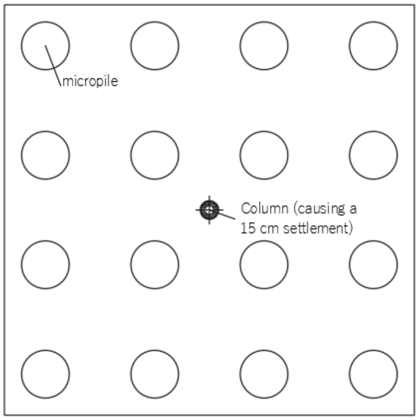

Fig. 6.2- configuration of the MPs (MPR under a load acting at the centroid of 4 micropiles- Type B

6.2.Load-settlement behavior

The load-settlement charts in this section demonstrate the differences in the load-bearing behavior of the micropiled raft models with various specifications in different relative densities of the sand. The effects of different soil stiffness (relative densities of 30%, 45%, and 60%), micropiles spacings of 3d,4d,5d,6d, and 7d, and raft stiffness are explored. The results have been classified according to the micropile spacing to diameter ratios.

A. MPR with load type A

1.MPRs (S/d=3)

Both types of MPRs, with rigid and semi-flexible rafts, exhibit a sudden change in load-settlement curves which is an indication of a local shear failure. Because of the transitional nature of local shear failure, the bearing capacity is defined as the first major nonlinearity in the load-settlement curve or at the point where the settlement rapidly increases (in this case both are located at the same spot). Soils that are medium-dense or firm are more likely to undergo local shear failures.

The following charts show that the bearing capacities of the models with s/d=3 were improved by the added micropiles. The ones with semi-flexible rafts showed a minimum of 117% improvement(Fig. 6.3) while this was about 60% for the ones with rigid rafts(Fig. 6.4).

On average, rigid rafts were able to carry larger loads than semi-flexible ones. In loose sand, the bearing capacity of the MPR with the rigid raft was 26% higher than the one with the semi-flexible raft. This number was 32% in the medium and dense sand beds% (Fig. 6.5).

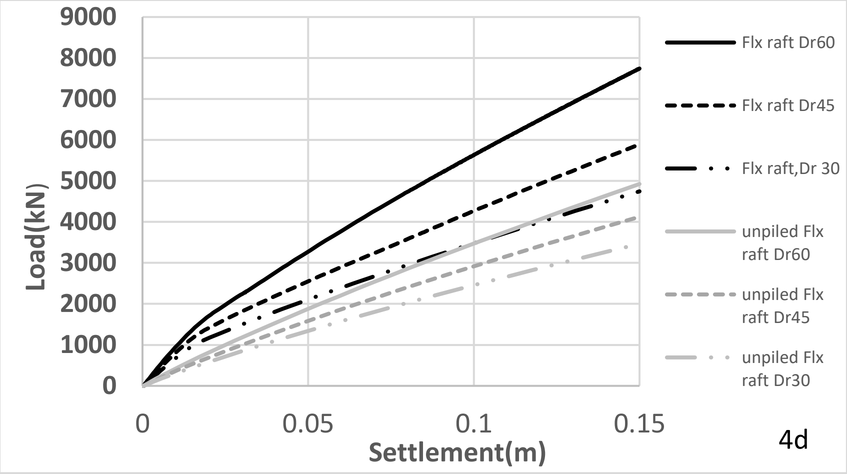

Fig. 6.3- Load-settlement of MPR with semi-flexible rafts vs. unpiled Rafts (s/d=3)

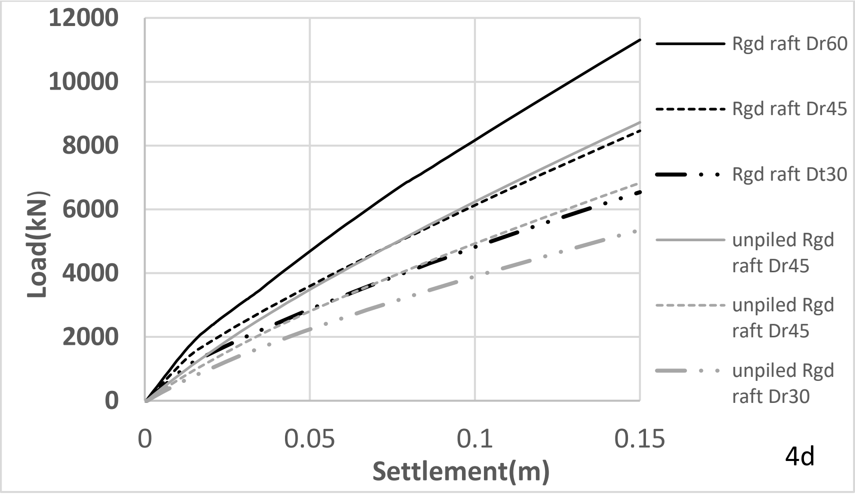

Fig. 6.4-- Load-settlement of MPR with rigid rafts vs. unpiled Rafts (s/d=3)

The ratio of the load carried by the MPR foundations in dense sand to the medium sand was also computed to evaluate the impact of sand bed relative density. The same process was repeated between medium sand and loose sand. The results showed that the greatest improvement (25%) happened for the MPR with the rigid raft when the medium sand bed was replaced by dense sand. The smallest value,19%, belonged to model A-3d-Flx-45% in comparison to A-3d-Flx-30% (Fig. 6.5).

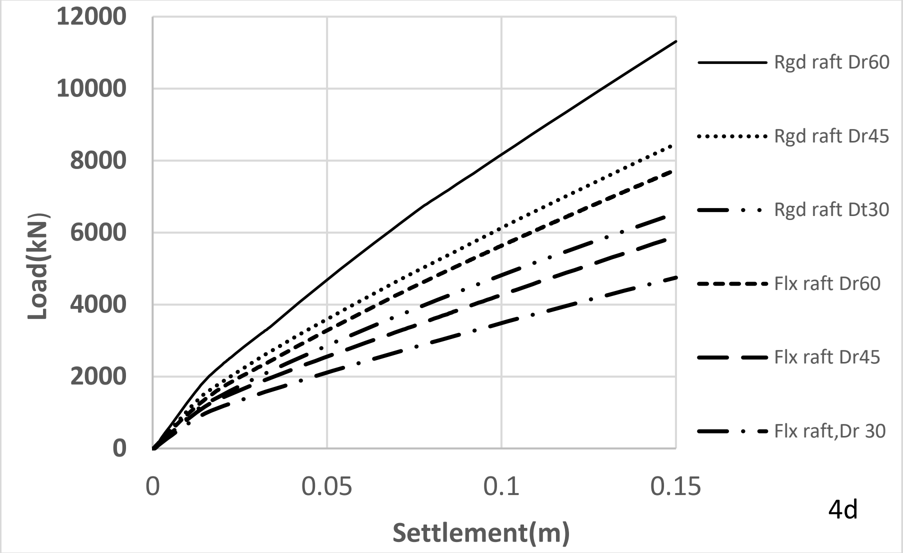

Fig. 6.5-Load-settlement of MPR with semi-flexible rafts vs. rigid Rafts (s/d=3)

2.MPR (s/d=4)

MPRs with rigid and semi-flexible rafts exhibit a sudden change in load-settlement curves which indicates local shearing failure. Because of the transitional nature of local shear failure, the bearing capacity is defined as the first major nonlinearity in the load-settlement curve or at the point where the settlement rapidly increases (in this case both are located at the same spot). Local shear failures are more likely to occur in medium-density or firm soils.

By including micropiles, MPRs were able to increase their bearing capacity. The ones with semi-flexible rafts showed a minimum of 97% improvement (Fig. 6.6) while this was about 79% for the ones with rigid rafts (Fig. 6.7).

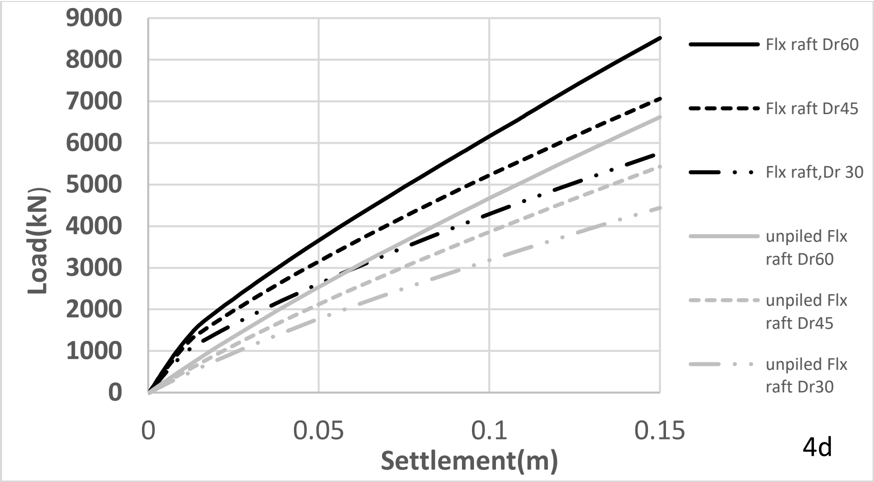

Fig. 6.6-Load-settlement of MPR with semi-flexible rafts vs. unpiled version (s/d=4)

.

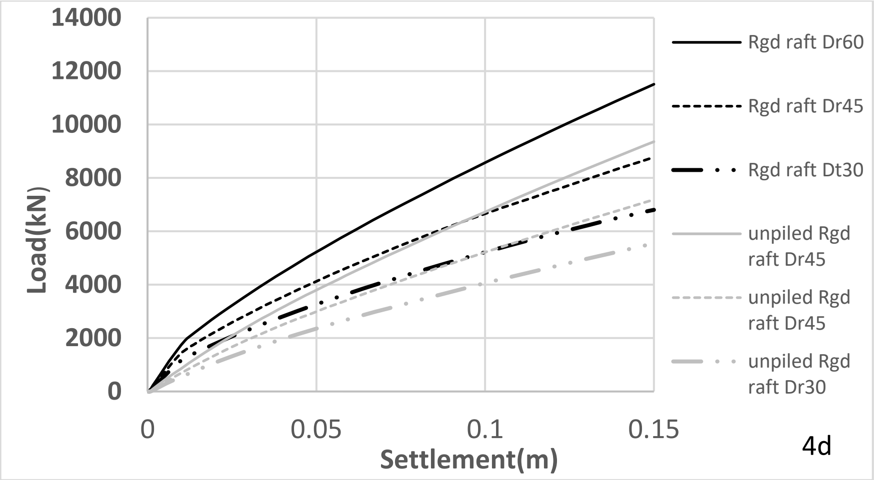

Fig. 6.7---Load-settlement of MPR with rigid rafts vs. unpiled version (s/d=4)

On average, rigid rafts were able to carry larger loads. In loose sand, the bearing capacity of the MPR with the rigid raft was 25% higher than the one with the semi-flexible raft. This number was 30% and 43% in the medium and dense sand beds (Fig. 6.8). The ratio of the load carried by the MPR foundations in dense sand to the medium sand was also computed to evaluate the impact of sand bed relative density. The same process was repeated between medium sand and loose sand. The results showed that the greatest improvement (24%) happened for the MPR with the rigid raft when the medium-dense sand bed was replaced by dense sand. The smallest value,14%, belonged to model A-4d-Flx-60% in comparison to A-4d-Flx-45% (Fig. 6.8).

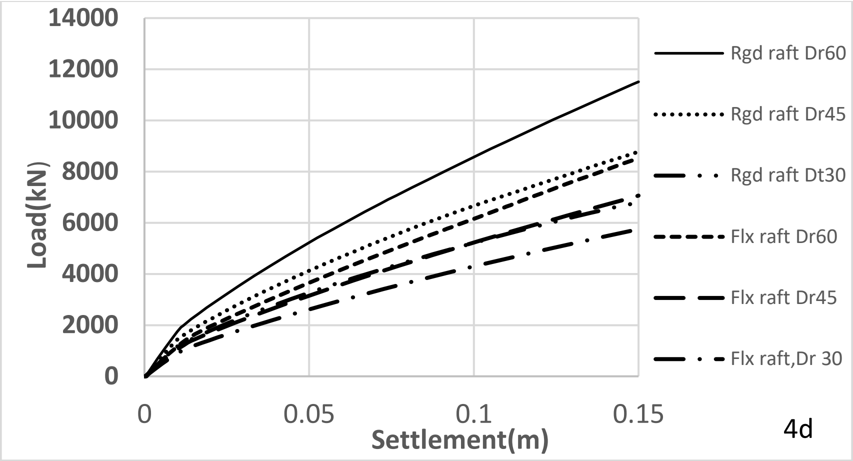

Fig. 6.8-Load-settlement of MPR with semi-flexible rafts vs. rigid Rafts (s/d=4)

3. *MPR (s/d=5)*

MPRs with rigid and semi-flexible rafts exhibit a sudden change in load-settlement curves which indicates local shearing failure. Because of the transitional nature of local shear failure, the bearing capacity is defined as the first major nonlinearity in the load-settlement curve or at the point where the settlement rapidly increases (in this case both are located at the same spot). Soils that are medium-dense or firm are more likely to undergo local shear failures.

The inclusion of micropiles improved the bearing capacity of the MPRs. The ones with semi-flexible rafts showed a minimum of 85% improvement (Fig. 6.9)while this was about 78% for the ones with rigid rafts (Fig. 6.10).

Loads carried by rigid rafts were generally larger, on average. In loose sand, the bearing capacity of the MPR with the rigid raft was 16% higher than the one with the semi-flexible raft. This number was 22% and 27% in the medium and dense sand beds (Fig. 6.11).

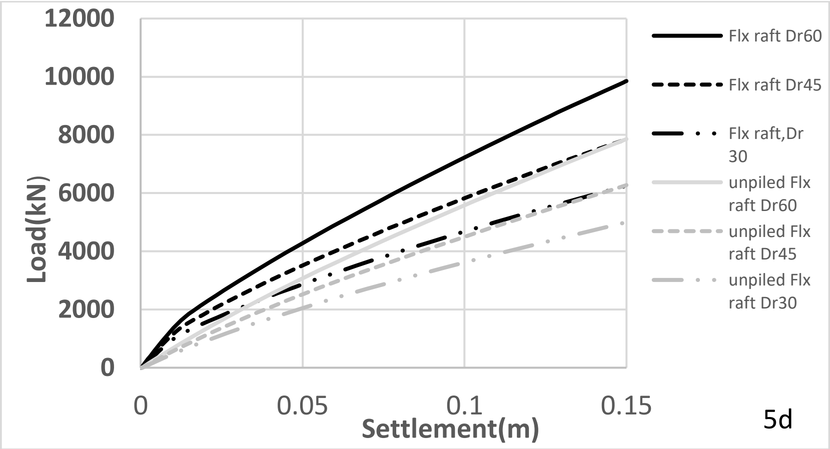

Fig. 6.9-Load-settlement of MPR with semi-flexible rafts vs. unpiled version (s/d=5)

.

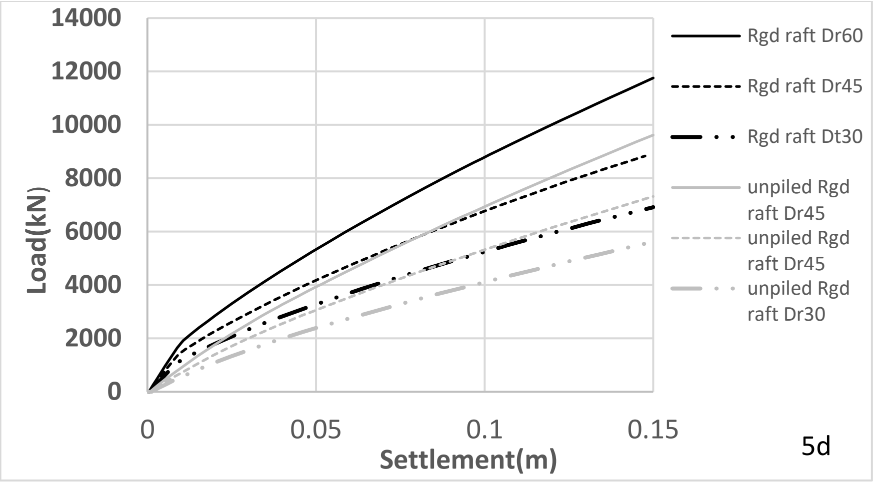

Fig. 6.10-Load-settlement of MPR with rigid rafts vs. unpiled version (s/d=5)

The ratio of the load carried by the MPR foundations in dense sand to the medium sand was also computed to evaluate the impact of sand bed relative density. The same process was repeated between medium sand and loose sand. The results showed that the greatest improvement (26%) happened for the MPR with the rigid raft when the loose sand bed was replaced by medium-dense sand. The smallest value,20%, belonged to model A-5d-F-45% in comparison to A-5d-F-30% (Fig. 6.11).

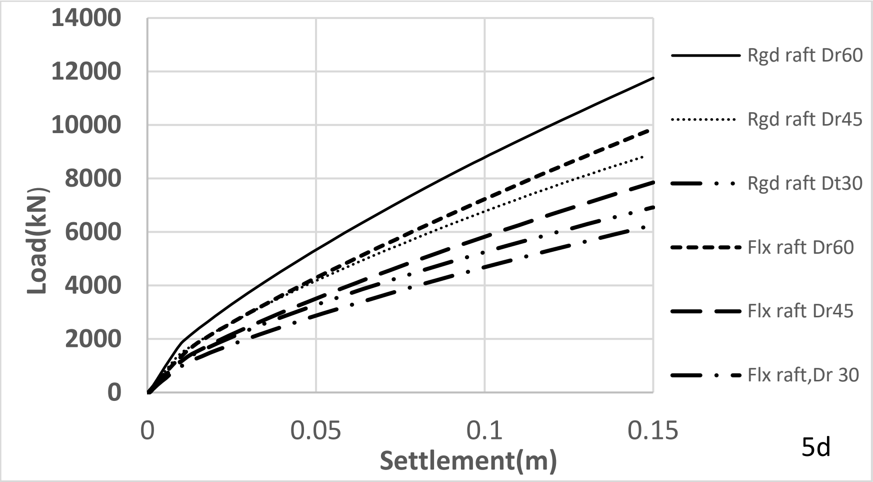

Fig. 6.11-Load-settlement of MPR with semi-flexible rafts vs. rigid Rafts (s/d=5)

4. *MPR (s/d=6)*

MPRs with rigid and semi-flexible rafts exhibit a sudden change in load-settlement curves which indicates local shearing failure. Because of the transitional nature of local shear failure, the bearing capacity is defined as the first major nonlinearity in the load-settlement curve or at the point where the settlement rapidly increases in this case both are located at the same spot). Soils that are medium-dense or firm are more likely to undergo local shear failures.

The inclusion of micropiles improved the bearing capacity of the MPRs. The ones with semi-flexible rafts showed a 79% improvement (Fig. 6.12) while this was about 82% for the ones with rigid rafts (Fig. 6.13).

On average, rigid rafts were able to carry larger loads. In loose sand, the bearing capacity of the MPR with the rigid raft was 10% higher than the one with the semi-flexible raft. This number was 14% and 19% in the medium and dense sand beds (Fig. 6.14).

.

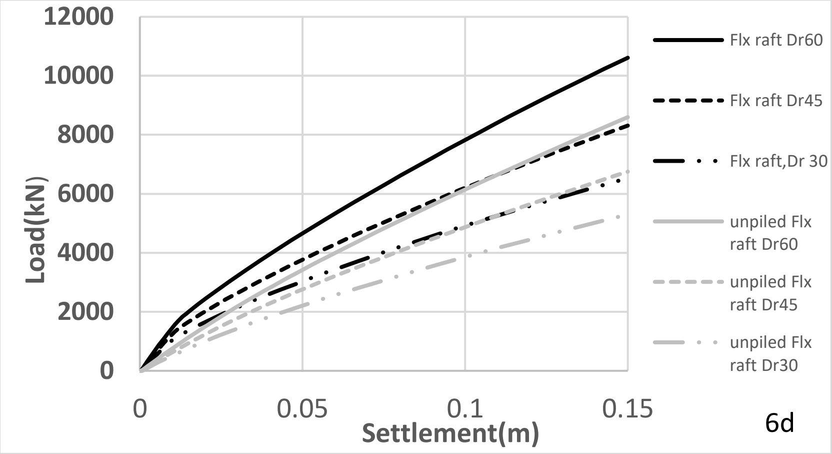

Fig. 6.12-Load-settlement of MPR with semi-flexible rafts vs. unpiled version (s/d=6)

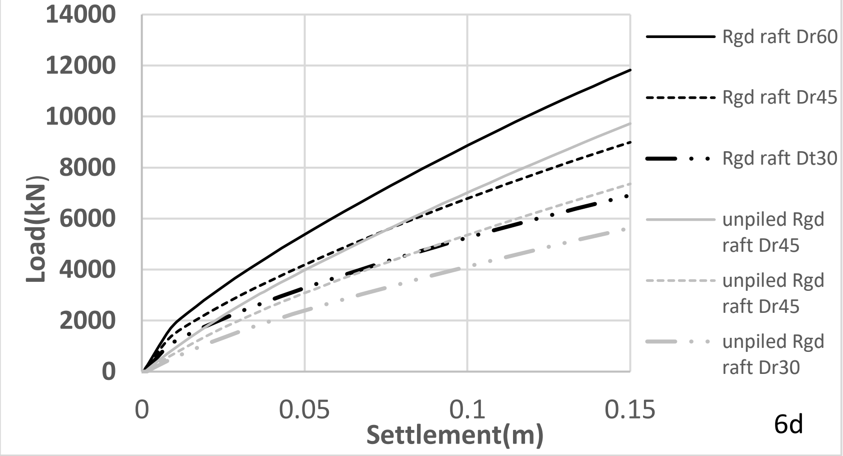

Fig. 6.13-Load-settlement of MPR with rigid rafts vs unpiled (s/d=6)

The ratio of the load carried by the MPR foundations in dense sand to the medium sand was also computed to evaluate the impact of sand bed relative density. The same process was repeated between medium sand and loose sand. The results showed that the greatest improvement (26%) happened for the MPR with the rigid raft when the medium-dense sand bed was replaced by dense sand. The smallest value,21%, belonged to model A-6d-F-45% in comparison to A-6d-F-30% (Fig.

6.14).

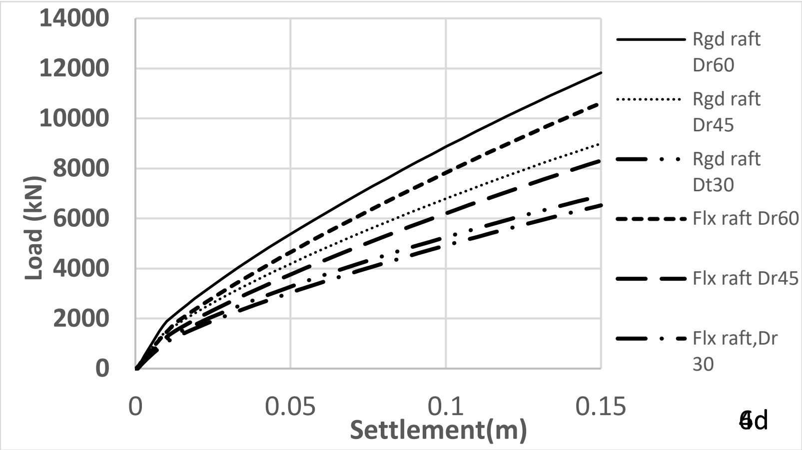

Fig. 6.14-Load-settlement of MPR with semi-flexible rafts vs. rigid Rafts (s/d=6)

5. MPR (s/d=7)

MPRs with rigid and semi-flexible rafts exhibit a sudden change in load-settlement curves which indicates local shearing failure. Because of the transitional nature of local shear failure, the bearing capacity is defined as the first major nonlinearity in the load-settlement curve or at the point where the settlement rapidly increases in this case both are located at the same spot). Soils that are medium-dense or firm are more likely to undergo local shear failures.

The inclusion of micropiles improved the bearing capacity of the MPRs. The ones with semi-flexible rafts showed a maximum improvement of 68% (Fig. 6.15) while this was about 70% for the ones with rigid rafts (Fig. 6.16).

On average, rigid rafts were able to carry larger loads. In loose sand, the bearing capacity of the MPR with the rigid raft was 5% higher than the one with the semi-flexible raft. This number was 9% and 12% in the medium and dense sand beds (Fig. 6.17).

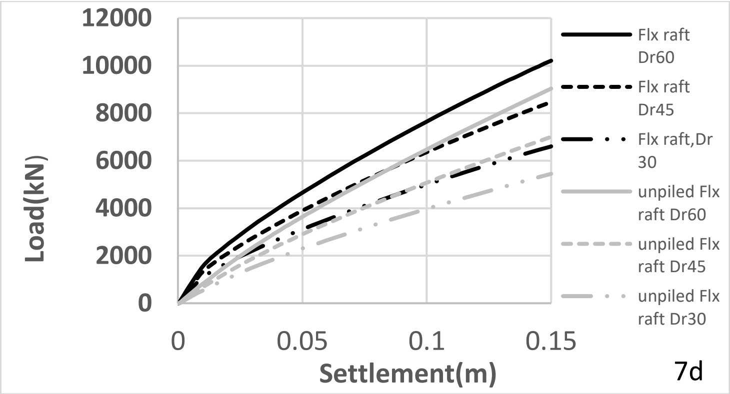

Fig. 6.15-Load-settlement of MPR with semi-flexible rafts vs. unpiled version (s/d=7)

The ratio of the load carried by the MPR foundations in dense sand to the medium sand was also computed to evaluate the impact of sand bed relative density. The same process was repeated between medium sand and loose sand. The results showed that the greatest improvement (27%) happened for the MPR with the rigid raft when the loose sand bed was replaced by medium-dense sand. The smallest value,18%, belonged to model A-7d-R-60% in comparison to A-7d-R-45% (Fig. 6.17).

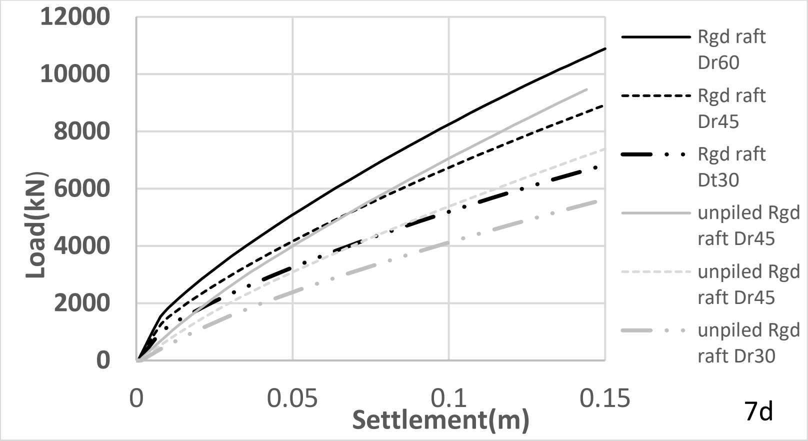

Fig. 6.16-Load-settlement of MPR with rigid rafts vs unpiled (s/d=7

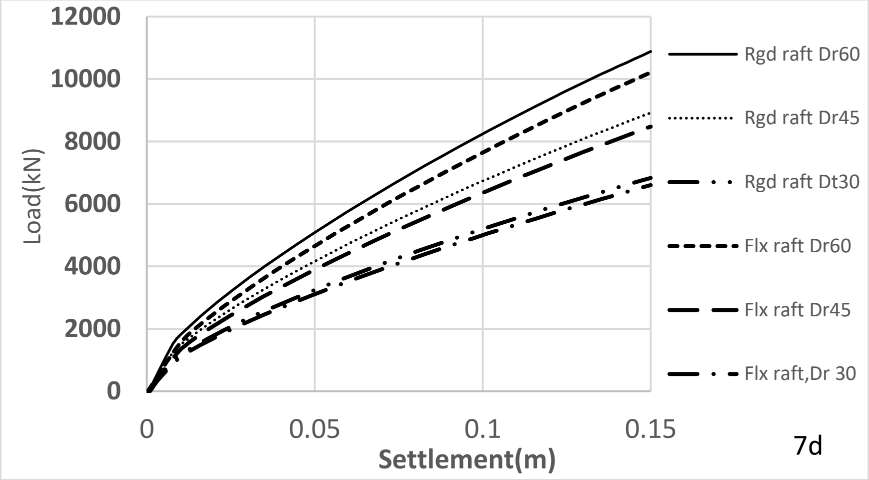

Fig. 6.17-Load-settlement of MPR with semi-flexible rafts vs. rigid Rafts (s/d=7)

B. MPRs with load type B

1. MPR (S/d=3)

MPRs with rigid and semi-flexible rafts exhibit a sudden change in load-settlement curves which indicates local shearing failure. Because of the transitional nature of local shear failure, the bearing capacity is defined as the first major nonlinearity in the load-settlement curve or at the point where the settlement rapidly increases (in this case both are located at the same spot). Soils that are medium-dense or firm are more likely to undergo local shear failures.

The inclusion of micropiles improved the bearing capacity of the MPRs. The ones with semi-flexible rafts showed a maximum improvement of 127% (Fig. 6.18) while this was about 66% for the ones with rigid rafts (Fig. 6.19).

On average, rigid rafts were able to carry larger loads than those with semi-flexible rafts. In loose sand, the bearing capacity of the MPR with the rigid raft was 49% higher than the one with the semi-flexible raft. This number was 52% and 58% in the medium and dense sand beds.

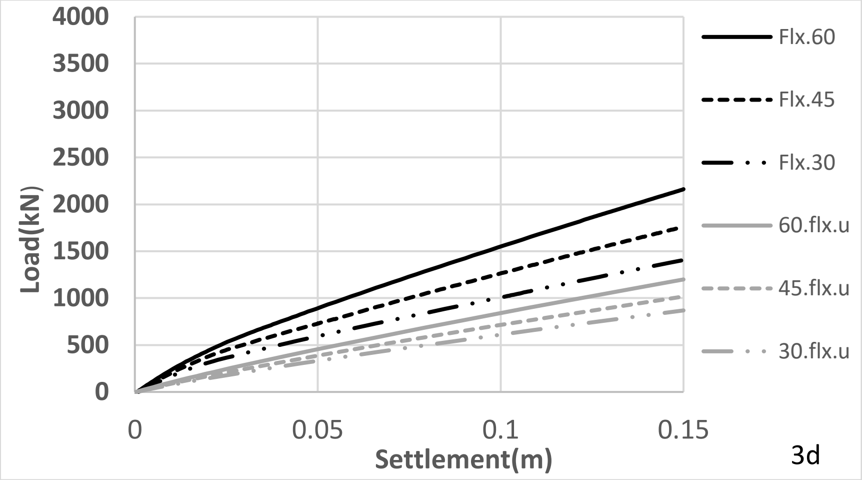

Fig. 6.18--Load-settlement of MPR with semi-flexible rafts vs. unpiled Rafts (s/d=3)

.

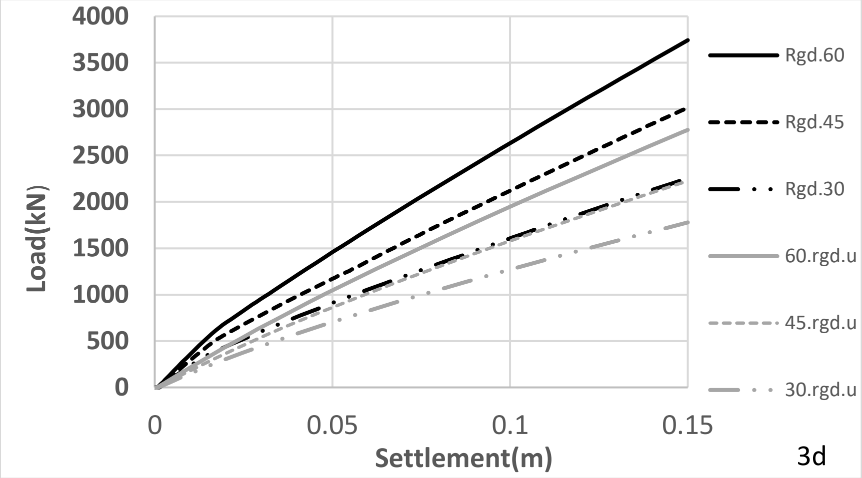

Fig. 6.19-Load-settlement of MPR with rigid rafts vs. unpiled Rafts (s/d=3)

The ratio of the load carried by the MPR foundations in dense sand to the medium sand was also computed to evaluate the impact of sand bed relative density. The same process was repeated for medium and loose sand. The results showed that the greatest improvement (28%) happened for the MPR with the rigid raft when the loose sand bed was replaced by medium-dense sand. The smallest value,17%, belonged to model B-3d-F-60% in comparison to B-3d-F-45% (Fig. 6.20).

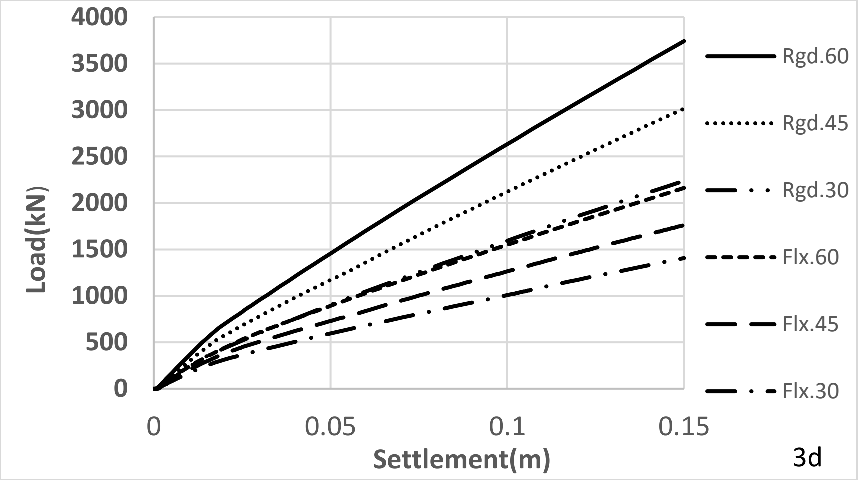

Fig. 6.20---Load-settlement of MPR with semi-flexible rafts vs. rigid Rafts (s/d=3)

2. MPR (s/d=4)

The load-settlement curves of MPRs with rigid and semi-flexible rafts show a sudden change, which indicates local shearing failure. Because of the transitional nature of local shear failure, the bearing capacity is defined as the first major nonlinearity in the load-settlement curve or at the point where the settlement rapidly increases (in this case both are located at the same spot). Local shear failures are more common in medium-dense or firm soils.

The inclusion of micropiles improved the bearing capacity of the MPRs. The ones with semi-flexible rafts showed a maximum improvement of 128% (Fig. 6.21) while this was about 96% for the ones with rigid rafts (Fig. 6.22). In loose sand, the bearing capacity of the MPR with the rigid raft was 49% higher than the one with the semi-flexible raft. This number was 59% and 64% in the medium and dense sand beds.

The ratio of the load carried by the MPR foundations in dense sand to the medium sand was also computed to evaluate the impact of sand bed relative density. The same process was repeated between medium sand and loose sand. The results showed that the greatest improvement (23%) happened for the MPR with the rigid raft when the loose sand bed was replaced by medium-dense sand. The smallest value,14%, belonged to model B-4d-F-60% in comparison to B-4d-F-45% (Fig. 6.23).

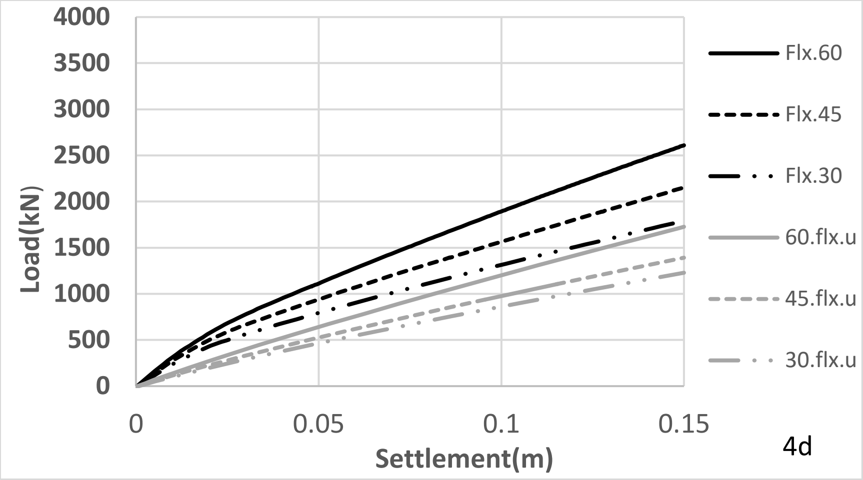

Fig. 6.21--Load-settlement of MPR with rigid rafts vs. unpiled Rafts (s/d=4)

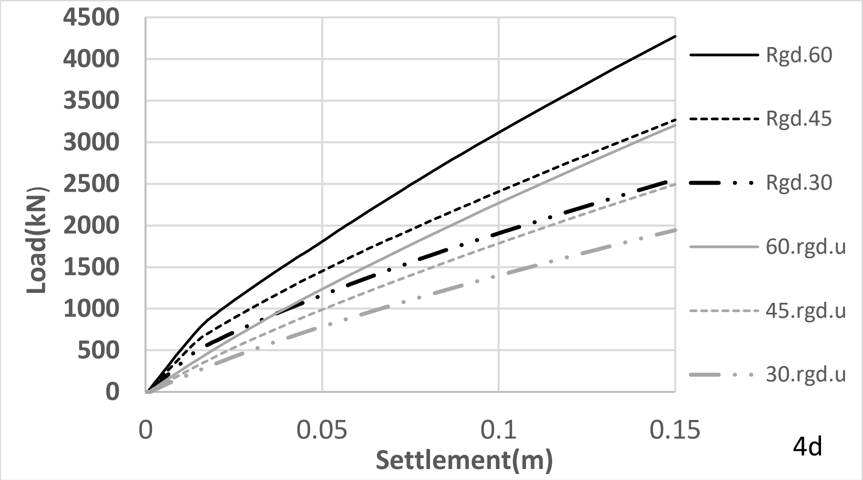

Fig. 6.22--Load-settlement of MPR with semi-flexible rafts vs unpiled Rafts (s/d=4)

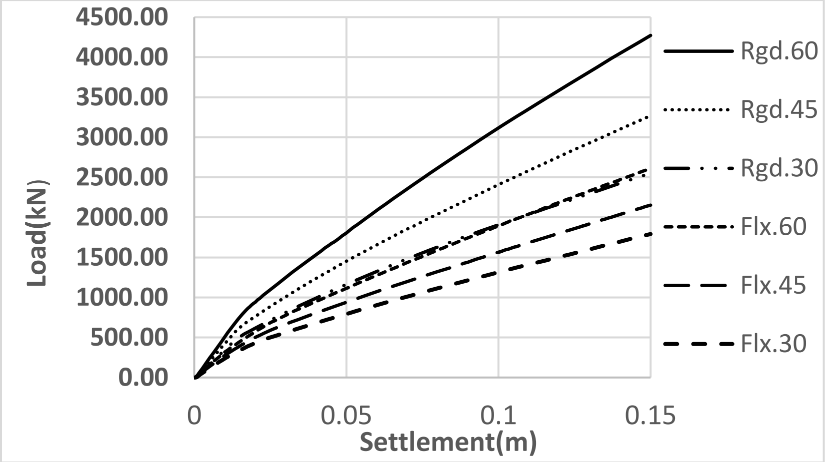

Fig. 6.23---Load-settlement of MPR with semi-flexible rafts vs. rigid Rafts (s/d=4)

3. MPR (s/d=5)

Load-settlement curves for rigid and semi-flexible rafts exhibit a sudden change, indicating local shearing. Because of the transitional nature of local shear failure, the bearing capacity is defined as the first major nonlinearity in the load-settlement curve or at the point where the settlement rapidly increases (in this case both are located at the same spot). Firm or medium-density soils are more prone to local shear failures.

The inclusion of micropiles improved the bearing capacity of the MPRs. The ones with semi-flexible rafts showed a maximum improvement of 100% (Fig. 6.24) while this was about 98% for the ones with rigid rafts (Fig. 6.25).

On average, rigid rafts were able to carry larger loads. In loose sand, the bearing capacity of the MPR with the rigid raft was 39% higher than the one with the semi-flexible raft. This number was 49% and 60% in the medium and dense sand beds.

The ratio of the load carried by the MPR foundations in dense sand to the medium sand was also computed to evaluate the impact of sand bed relative density. The same process was repeated between medium sand and loose sand. The results showed that the greatest improvement (25%) happened for the MPR with the rigid raft when the loose sand bed was replaced by medium-dense sand. The smallest value,16%, belonged to model B-5d-F-60% in comparison to B-5d-F-45% (Fig. 6.26).

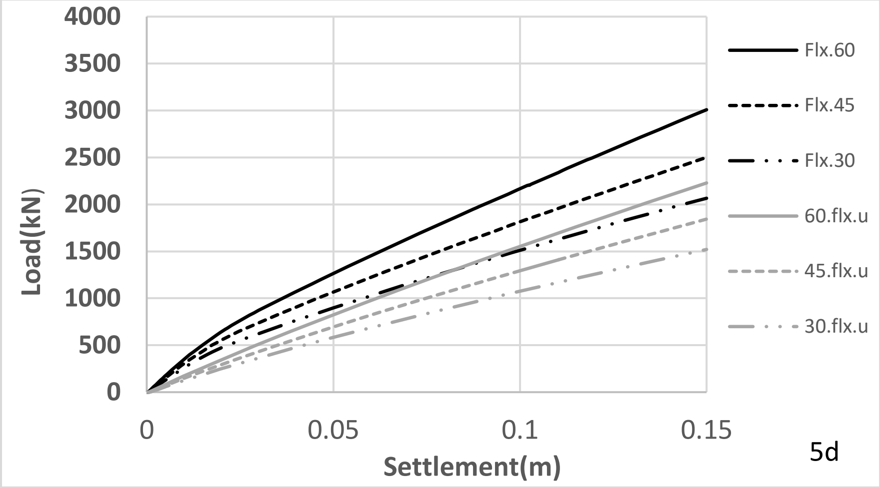

Fig. 6.24--Load-settlement of MPR with semi-flexible rafts vs unpiled Rafts (s/d=5)

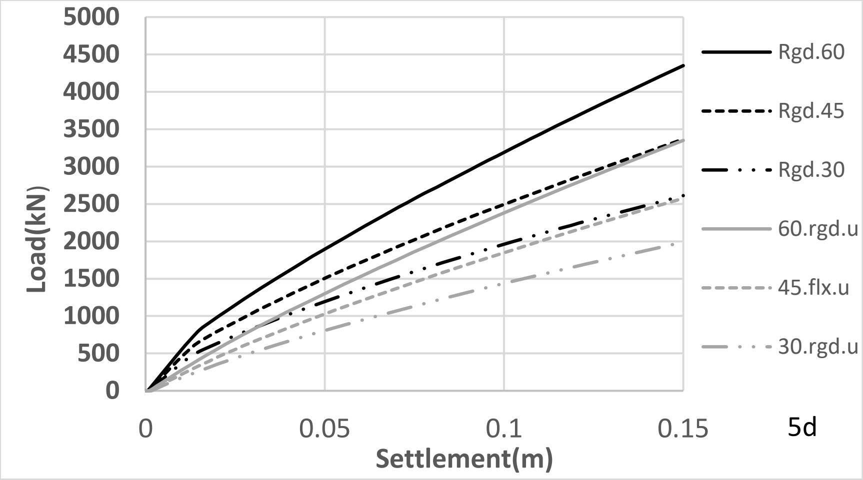

Fig. 6.25--Load-settlement of MPR with rigid rafts vs unpiled Rafts (s/d=5)

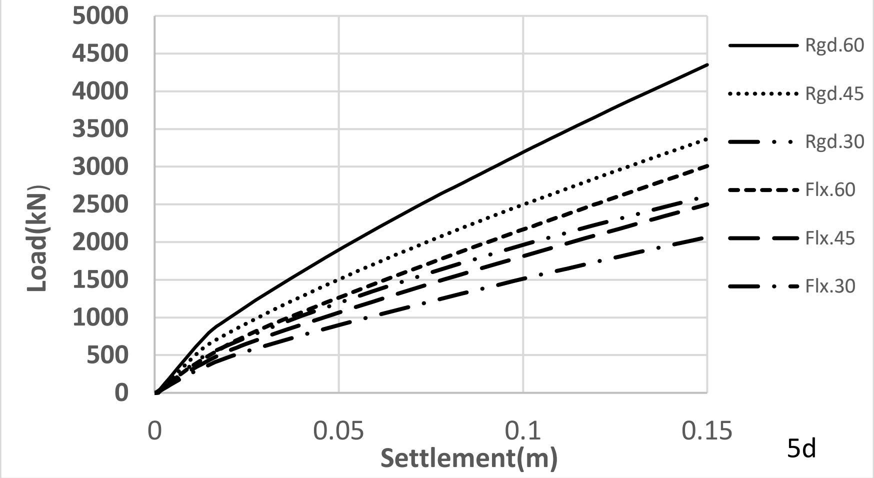

Fig. 6.26-Load-settlement of MPR with semi-flexible rafts vs. rigid Rafts (s/d=5)

4. MPR (S/d=6)

There is a sudden shift in load-settlement curves of rigid and semi-flexible MPRs, which indicates local shearing failure. Because of the transitional nature of local shear failure, the bearing capacity is defined as the first major nonlinearity in the load-settlement curve or at the point where the settlement rapidly increases in this case both are located at the same spot). Soils that are medium-dense or firm are more likely to undergo local shear failures.

The inclusion of micropiles improved the bearing capacity of the MPRs. The ones with semi-flexible rafts showed a maximum improvement of 86% (Fig. 6.27) while this was about 100% for the ones with rigid rafts (Fig. 6.28).

On average, rigid rafts were able to carry larger loads. In loose sand, the bearing capacity of the MPR with the rigid raft was 34% higher than the one with the semi-flexible raft. This number was 44% and 57% in the medium and dense sand beds.

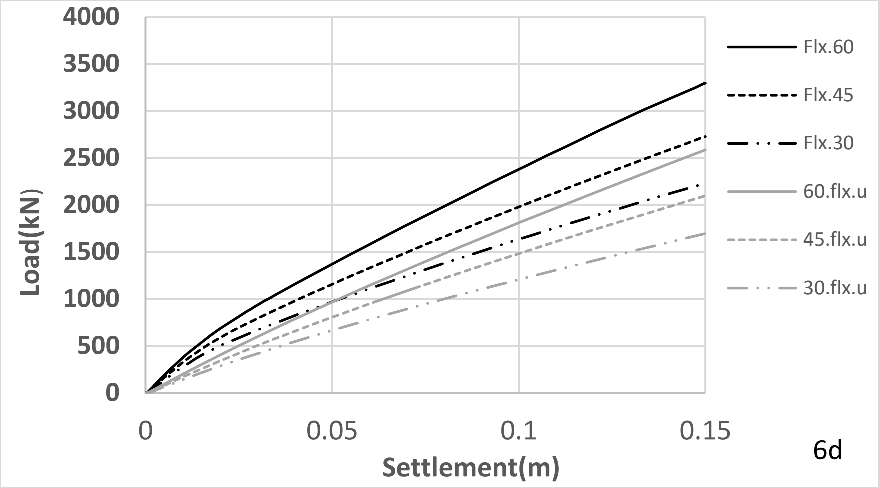

Fig. 6.27-Load-settlement of MPR with semi-flexible rafts vs unpiled Rafts (s/d=6)

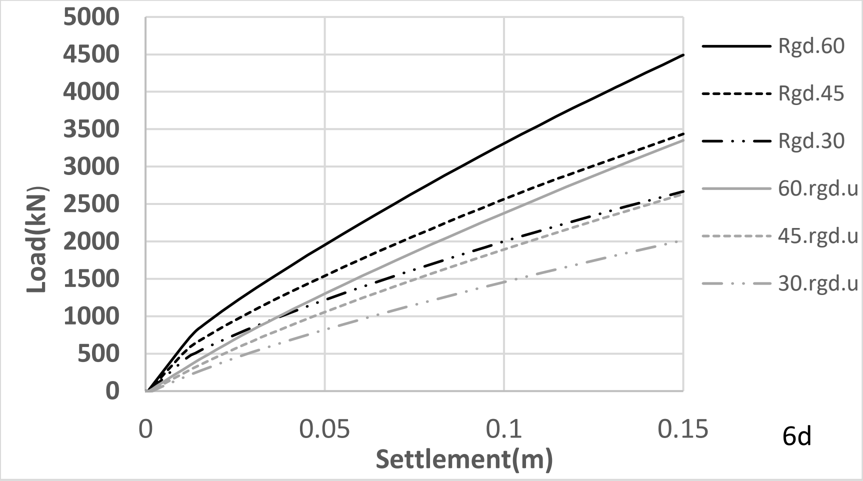

Fig. 6.28-Load-settlement of MPR with rigid rafts vs unpiled Rafts (s/d=6)

To evaluate the impact of sand bed density, the ratio between the MPR foundations carried by dense sand and medium sand was calculated. The same process was repeated between medium sand and loose sand. The results showed that the greatest improvement (26%) happened for the MPR with the rigid raft when the medium-dense sand bed was replaced by dense sand. The smallest value,15%, belonged to model B-6d-F-60% in comparison to B-6d-F-45% (Fig. 6.29).

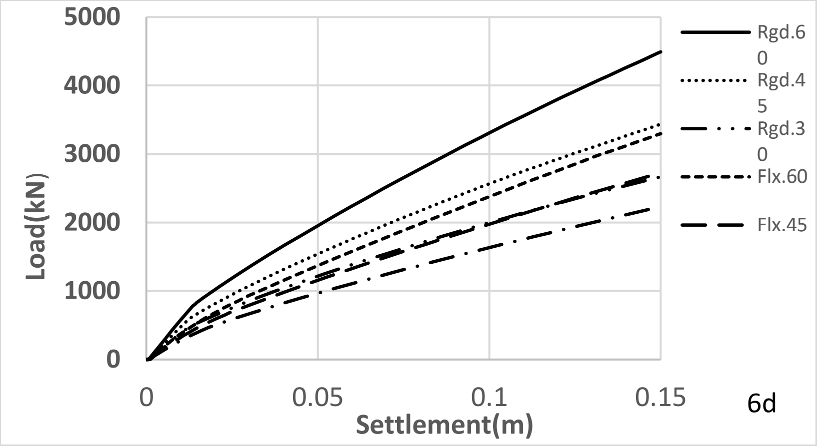

Fig. 6.29-Load-settlement of MPR with semi-flexible rafts vs. rigid Rafts (s/d=6)

5. MPR (S/d=7)

MPRs with rigid and semi-flexible rafts exhibit a sudden change in load-settlement curves which indicates local shearing failure. Because of the transitional nature of local shear failure, the bearing capacity is defined as the first major nonlinearity in the load-settlement curve or at the point where the settlement rapidly increases (in this case both are located at the same spot). Typically, medium-density or firm soils will experience local shear failures.

The inclusion of micropiles improved the bearing capacity of the MPRs. The ones with semi-flexible rafts showed a maximum improvement of 83% (Fig. 6.30)while this was about 105% for the ones with rigid rafts (Fig. 6.31).

On average, rigid rafts were able to carry larger loads. In loose sand, the bearing capacity of the MPR with the rigid raft was 24% higher than the one with the semi-flexible raft. This number was 41% and 46% in the medium and dense sand beds.

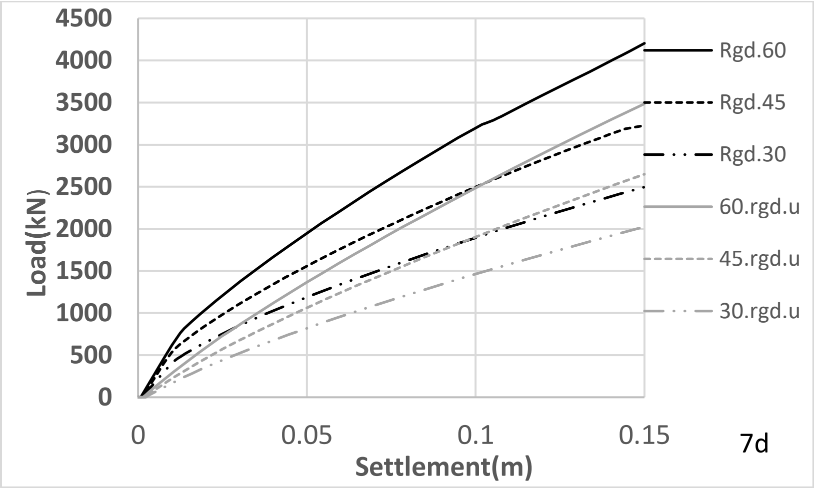

Fig. 6.30-Load-settlement of MPR with semi-flexible rafts vs. unpiled Rafts (s/d=7)

.

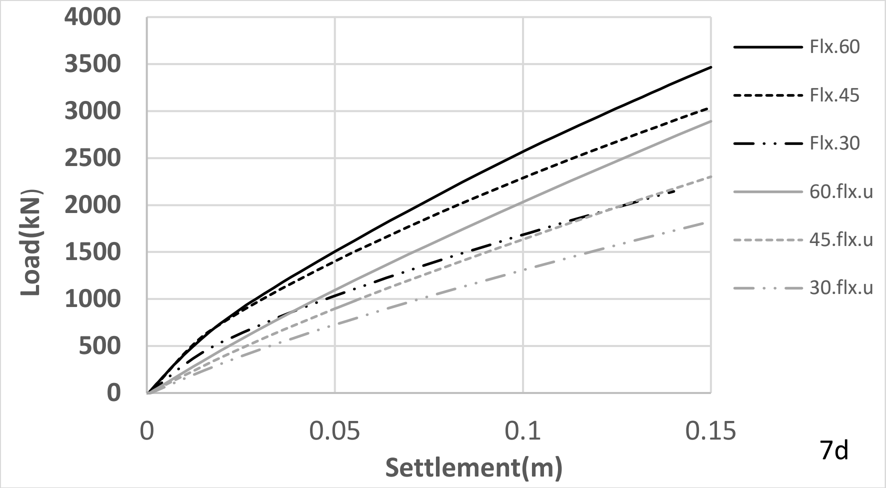

Fig. 6.31-Load-settlement of MPR with rigid rafts vs. unpiled Rafts (s/d=7)

We also evaluated the impact of sand bed density on the load carried by the MPR foundations in dense sand versus medium sand. The same process was repeated between medium sand and loose sand. The results showed that the greatest improvement (33%) happened for the MPR with the semi-flexible raft when the loose sand bed was replaced by medium-dense sand. The smallest value,16%, belonged to model B-7d-F-45% in comparison to B-7d-F-30% (Fig. 6.32).

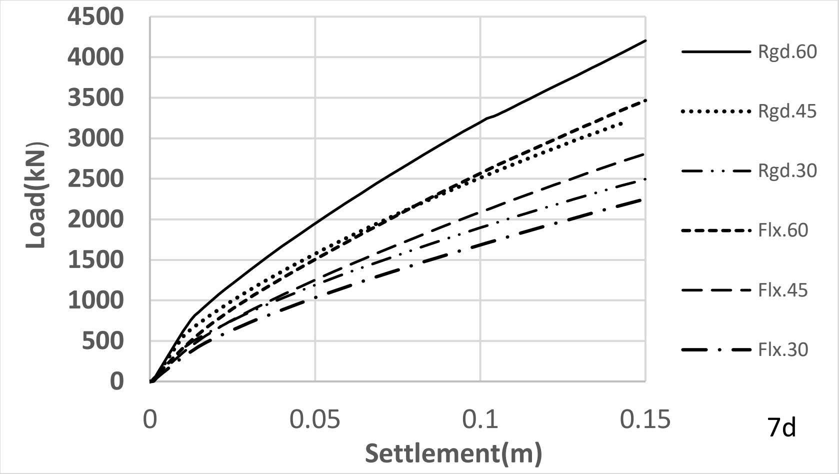

Fig. 6.32-Load-settlement of MPR with semi-flexible rafts vs. rigid Rafts (s/d=7)

6.3.Reduction in the overall settlement

A. MPRs under load type A

At s/d=3, for the MPRs with semi-flexible rafts, the decline in the overall settlement was about

40%. The MPRs with rigid rafts experienced a maximum decline of 30% in the overall settlement
.

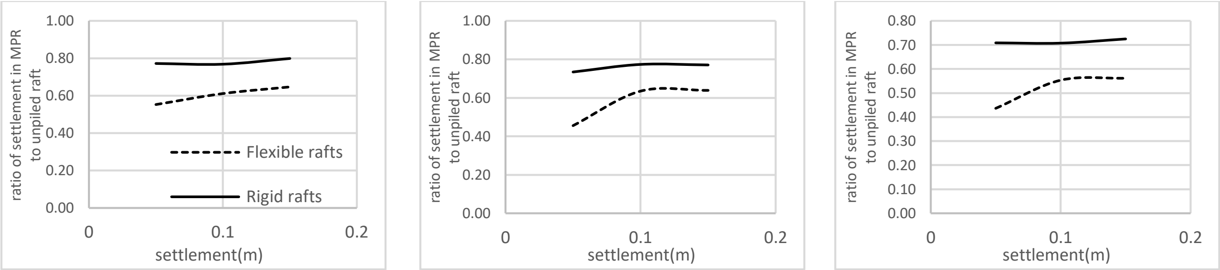

Fig. 6.33-s/d=3, Dr=30%, 45%, and 60% (reduction in overall settlement-load type A)

Our data show that for the MPRs with semi-flexible rafts, the overall settlement declined by approximately 40% at s/d=4. The MPRs with rigid rafts experienced a maximum decline of 30% in the overall settlement.

At s/d=5, for the MPRs with semi-flexible rafts, the maximum decline in the overall settlement was about 30%. The MPRs with rigid rafts experienced the same percentage of decline i.e. 30% in the overall settlement.

At s/d=6, for the MPRs with semi-flexible rafts, the maximum decline in the overall settlement was about 30%. The MPRs with rigid rafts experienced the same percentage of decline i.e. 30% in the overall settlement.

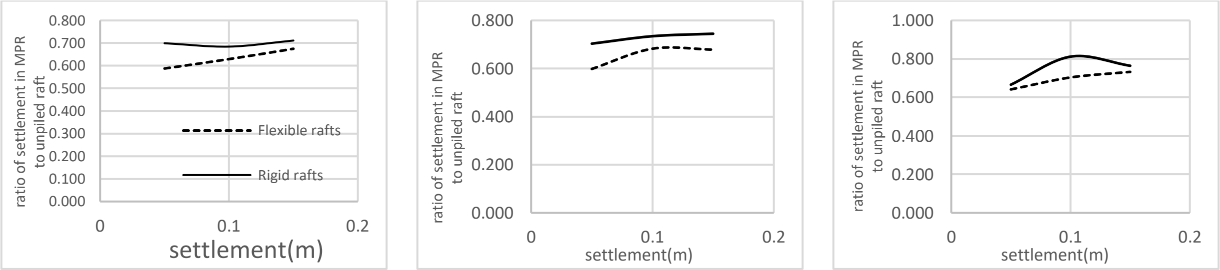

Fig.34-s/d=4, Dr=30%, 45%, and 60% (reduction in overall settlement-load type A)

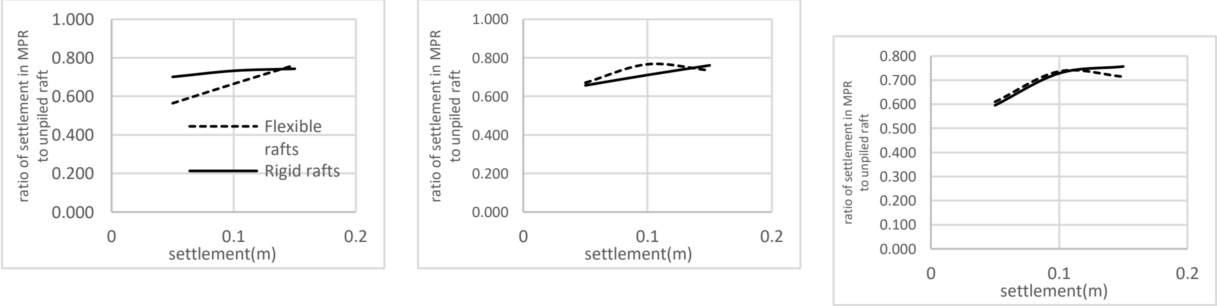

Fig. 6.35-s/d=5, Dr=30%, 45%, and 60% (reduction in overall settlement-load type A)

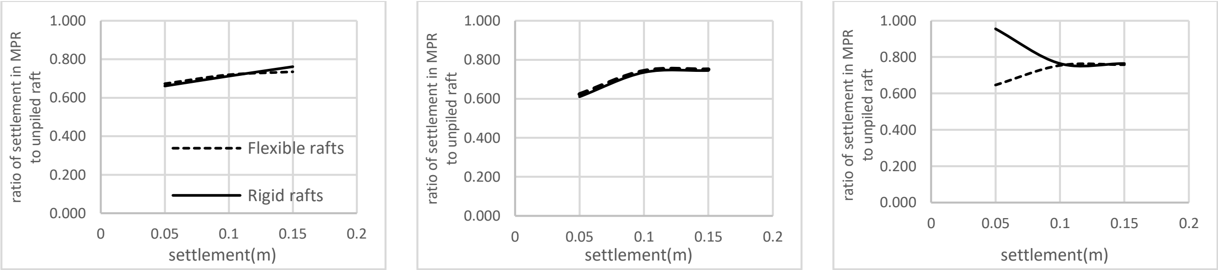

Fig. 6.36-s/d=6, Dr=30%, 45%, and 60% (reduction in overall settlement-load type A)

Adding micropiles to settlements at s/d=7 resulted in a 20% reduction in overall settlement. There was not much difference between the behavior of MPRs with flexible and rigid rafts in this regard.

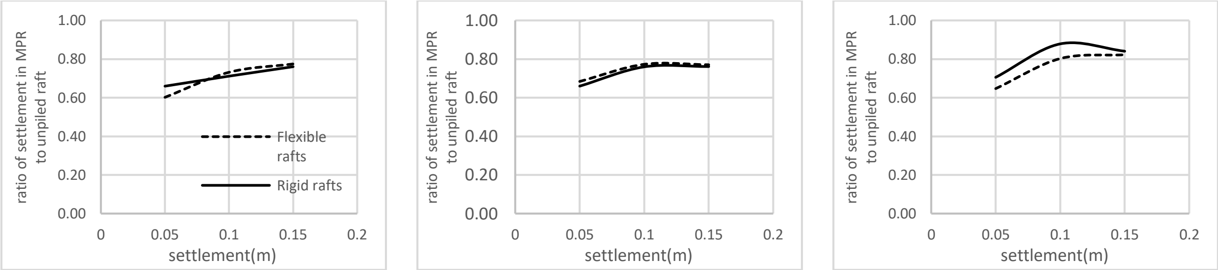

Fig. 6.37-s/d=7, Dr=30%, 45%, and 60% (reduction in overall settlement-load type A)

B. MPRs under load type B

To evaluate the effects of the micropiles in reducing the overall settlement, the ratio of the overall settlement of the micropiled rafts to that of the unpiled counterparts was calculated and given in the form of graphs for MPRs with both the rigid and the semi-flexible rafts.

At s/d=3, for the rigid rafts sitting on the medium-dense and dense sand, the drop of the overall settlement achieved by adding the micropiles is about 30% of the unpiled version except for the loose sands, where this reduction is lower, i.e., 20%. In the case of semi-flexible rafts, this decline in the overall settlement varied between 40% and 50%.

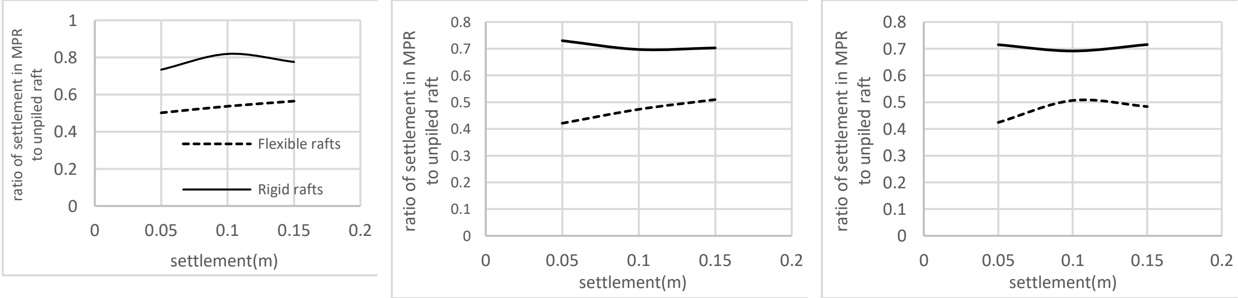

Fig. 6.38- s/d=3, Dr=30%,45%, and 60% (reduction in overall settlement-loading type B)

At s/d=4, for the rigid rafts sitting, the drop in the overall settlement was about 30% of the unpiled version. In the case of semi-flexible rafts, this decline in the overall settlement varied between 40% and 50%.

At micropile spacing to diameter ratios of 5,6, and 7, for both the rigid and semi-flexible rafts, the drop in the overall settlement was about 30% of the overall settlement except for in the loose sand where a minor difference was observed between the MPRs with semi-flexible and rigid rafts.

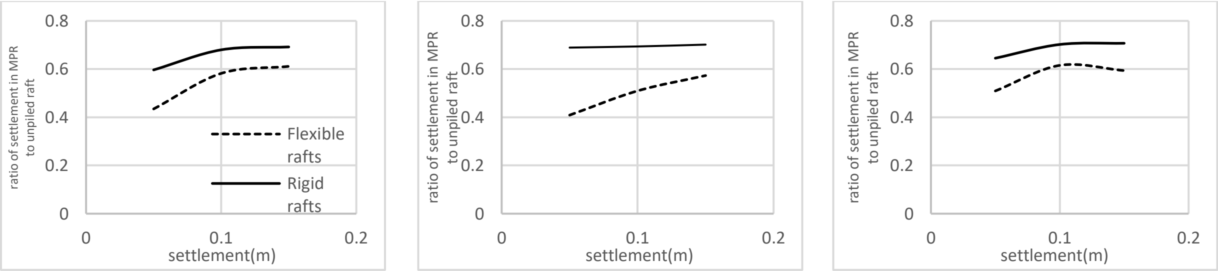

Fig. 6.39- s/d=4, Dr=30%,45%, and 60% (reduction in overall settlement-loading type B)

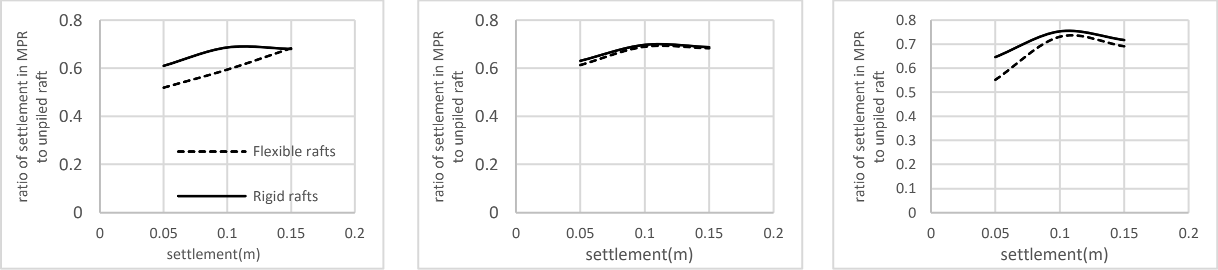

Fig. 6.40- s/d=5, Dr=30%,45%, and 60% (reduction in overall settlement-loading type B)

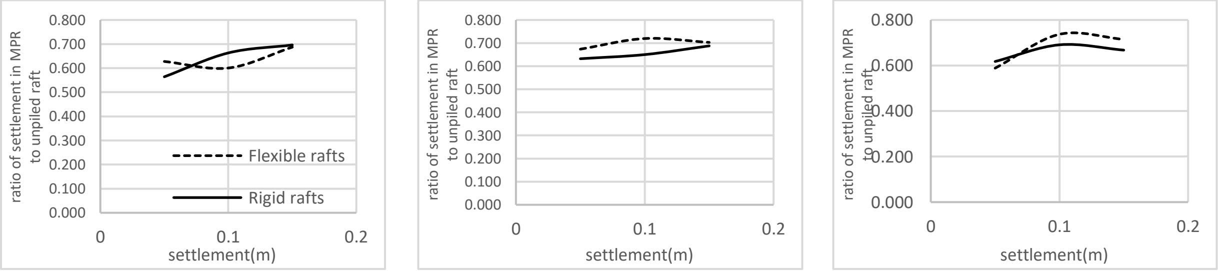

Fig. 6.41- s/d=6, Dr=30%,45%, and 60% (reduction in overall settlement-loading type B)

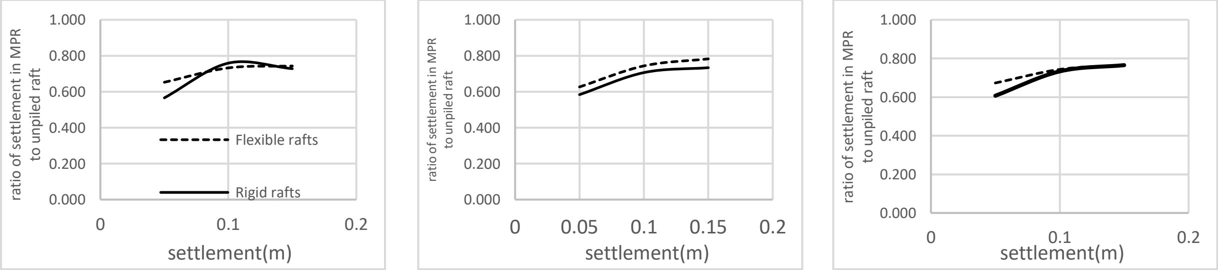

Fig. 6.42- s/d=7, Dr=30%,45%, and 60% (reduction in overall settlement-loading type B)

6.4.Skin friction (shaft resistance)

Skin friction of the micropiles is the main element providing the highest contribution to their overall bearing capacity. This feature is mainly achieved through the pressurized penetrating grout. FHWA, in its guideline for micropile design and construction, suggests the designer use a formula that does not consider the end-bearing capacity. Here, we examine the effects of soil relative density, raft stiffness, micropile spacing ratio, and the location of concentrated loads/displacements on the skin friction of the micropiles. For this purpose, the average skin friction of the micropiles at the settlement of 50,75,100, and 150 mm have been extracted from the simulations' outputs and presented in the following subsections.

A. MPRs under load type A

The average skin frictions of the micropiles are presented in the tables below according to the overall settlement. These values have been sorted by relative densities of the soil (sand), overall settlement, pile spacing between the micropiles, size, and the flexibility of the rafts. Since the MPR's layout and configuration of the micropiles were symmetrical, the central micropile was selected because it absorbed the largest portion of the load.

During the process of settlement, skin friction increases as a consequence of the interaction between the pile, soil, and raft. The data shows that maximum skin friction occurs at the maximum settlement of 150 mm, where the capacity reaches the peak point.

Table 6.1 summarizes the values of the average skin resistance of the central micropile located underneath the MPR with a spacing ratio of 3 based on the overall settlement. It was noted that this particular micropile carried the largest axial load compared to the others due to its location making this micropile carry the largest skin friction. The highest value was recorded at the settlement of 15cm, and as shown, when the sand becomes denser, the number goes up.

skin friction at settlement (kN/m2)			
Sett (cm)	**5cm**	**10cm**	**15cm**
3d.30.f	106	169	224
3d.30.r	77	118	157
3d.45.f	125	208	282
3d.45.r	94	154	207
3d.60.f	172	282	381
3d.60.r	128	211	287

Table 6.1- Skin resistance of micropiles at the center of the raft (s/d=3)

The values in Table 6.2 summarizes the values of the average skin resistance of the central micropile located underneath the MPR with a spacing ratio of 4 based on the overall settlement. It was noted that this particular micropile carried the largest axial load compared to the others due to its location making this micropile carry the largest skin friction. The highest value was recorded at the settlement of 15cm, and as shown, when the sand becomes denser, the number goes up. We can see that for each model, the skin friction is lower than its counterpart with s/d=3.

Skin friction at settlement (kN/m^2)			
Sett (cm)	**5cm**	**10 cm**	**15 cm**
4d.30.f	79	128	167
4d.30.r	57	91	113
4d.45.f	98	157	208
4d.45.r	72	112	149
4d.60.f	117	187	255
4d.60.r	94	147	196

Table 6.2- Skin resistance of micropiles at the center (s/d=4)

As shown in Table 6.3, it summarizes the values of the average skin resistance of the central micropile located underneath the MPR with a spacing ratio of 5 based on the overall settlement. It was noted that this particular micropile carried the largest axial load compared to the others due to its location. Therefore, this micropile has the largest skin friction. The highest value was recorded at the settlement of 15cm, and as shown, when the sand becomes denser, the number goes up. We can see that for each model, the skin friction is lower than its counterpart with s/d=4 &3.

Skin friction at settlement (kN/m^2)			
Sett (cm)	**5cm**	**10 cm**	**15 cm**
5d.30.f	77	116	153
5d.30.r	49	77	98
5d.45.f	89	145	193
5d.45.r	65	97	128
5d.60.f	112	190	244
5d.60.r	81	126	170

Table 6.3- Skin resistance of micropiles at the center (s/d=5)

Table 6.4 shows the values of the average skin resistance of the central micropile located underneath the MPR with a spacing ratio of 6 based on the overall settlement. It was noted that this particular micropile carried the largest axial load compared to the others due to its location. Because of this, this micropile has the highest skin friction. The highest value was recorded at the settlement of 15cm, and as shown, the numbers increased when the sand beds were replaced by another denser one.

Skin friction at settlement (kN/m^2)			
Sett (cm)	**5cm**	**10 cm**	**15 cm**
6d.30.f	82	124	162
6d.30.r	51	75	98
6d.45.f	99	154	208
6d.45.r	65	99	129
6d.60.f	125	197	266
6d.60.r	85	128	172

Table 6.4- Skin resistance of micropiles at the center (s/d=6)

According to the overall settlement of the MPR, Table 6.5 summarizes the values of the average skin resistance of the central micropile located underneath the MPR with a spacing ratio of 7The highest value was recorded at the settlement of 15cm, and as shown, when the sand becomes denser, the number rises.

Skin friction at settlement (kN/m^2)			
Sett (cm)	**5cm**	**10 cm**	**15 cm**
7d.30.f	78	124	162
7d.30.r	50	74	96
7d.45.f	98	158	208
7d.45.r	65	96	128
7d.60.f	122	190	255
7d.60.r	77	122	160

Table 6.5- Skin resistance of micropiles at the center (s/d=7)

1. Micropiles' end-bearing capacity to the total load capacity

In addition to skin resistance, we calculated the toe-top load ratio for each micropile and tabulated it. For the MPR with load type A, the central micropile showed the smallest values of the toe to total load ratio regardless of the micropile spacing ratio, sand relative density, and the overall settlement. The numbers are significantly smaller than in case B because the central micropile herein easily reached its peak point and had the chance to mobilize the skin friction to the fullest.

The ratio of end bearing to total load at settlement (kN/m^2)				The ratio of end bearing to total load at settlement (kN/m^2)			
Sett (cm)	**5cm**	**10 cm**	**15 cm**	***Sett (cm)***	**5cm**	**10 cm**	**15 cm**
3d.30.f	8%	9%	9%	**5d.45.r**	15%	17%	18%
3d.30.r	11%	12%	12%	**5d.60.f**	12%	13%	13%
3d.45.f	8%	9%	10%	**5d.60.r**	15%	17%	19%
3d.45.r	11%	12%	12%	**6d.30.f**	10%	11%	12%
3d.60.f	8%	9%	10%	**6d.30.r**	15%	17%	18%
3d.60.r	9%	11%	12%	**6d.45.f**	11%	11%	12%
4d.30.f	10%	11%	12%	**6d.45.r**	15%	17%	18%
4d.30.r	14%	16%	16%	**6d.60.f**	11%	12%	12%
4d.45.f	11%	12%	12%	**6d.60.r**	15%	17%	18%
4d.45.r	14%	16%	17%	**7d.30.f**	10%	11%	11%
4d.60.f	12%	13%	13%	**7d.30.r**	15%	17%	18%
4d.60.r	14%	16%	17%	**7d.45.f**	10%	11%	11%
5d.30.f	11%	12%	12%	**7d.45.r**	15%	17%	18%
5d.30.r	15%	17%	18%	**7d.60.f**	11%	11%	11%
5d.45.f	11%	12%	13%	**7d.60.r**	15%	17%	17%

Table 6.6- Ratio of end-bearing capacity to the total load

B. MPRs under load type B

The average skin frictions of the micropiles are presented in the tables below according to the overall settlement. These values have been sorted by relative densities of the soil (sand), overall settlement, pile spacing between the micropiles, size, and the flexibility of the rafts. Since the MPR's layout and configuration of the micropiles were symmetrical, the central micropile was selected because it absorbed the largest portion of the load. During the process of settlement, skin friction increases as a consequence of the interaction between the pile, soil, and raft. The data shows that maximum skin friction occurs at the maximum settlement of 150 mm, where the load capacity reaches the peak point.

.

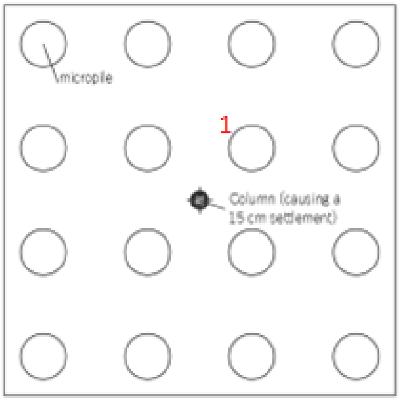

Fig. 6.43- Location of micropile 1

The variation of the skin friction at various stages of settlement shows that the frictional resistance increases with the settlement, which is a consequence of the pile-soil-raft interaction. The data in the table below (Table 6.7) indicates that maximum skin friction occurs at the maximum settlement of 150 mm, where the capacity reaches the peak point. The table also suggests that the average skin friction increases, as the soil (sand) gets denser.

One can observe that some of the computed values from the FEM models are different, mostly smaller, than the skin friction calculated from what has been recommended in the Federal Highway Administration's guide (FHWA). The rest of the computed skin frictions are in fair agreement with FHWA's guide. It should be noted that these numbers are only achieved if the micropiles settle deep enough to mobilize their capacities.

Skin friction at settlement (kN/m^2)				**Skin friction at settlement (kN/m^2)**			
Sett (cm)	**5cm**	**10cm**	**15cm**	***Sett (cm)***	**5cm**	**10cm**	**15cm**
3d.30.f	16.35	22.29	30.57	**5d.45.r**	25.9	57.54	49.26
3d.30.r	15.70	22.51	31.63	**5d.60.f**	34.82	44.8	58.6
3d.45.f	23.78	33.86	46.2	**5d.60.r**	34.18	52.44	68.79
3d.45.r	25.37	33.47	53.84	**6d.30.f**	19.41	24.11	30.15
3d.60.f	36.09	53.29	67.01	**6d.30.r**	19.8	25.58	33.33
3d.60.r	40.44	62.27	80.89	**6d.45.f**	25.23	31.4	39.28
4d.30.f	20.17	24.63	31.42	**6d.45.r**	25.65	35.24	46.71
4d.30.r	20.02	28.03	36.31	**6d.60.f**	32.78	41.4	54.14
4d.45.f	26.54	35.46	44.37	**6d.60.r**	33.55	46.22	63.69
4d.45.r	25.94	40.02	52.02	**7d.30.f**	18.89	24.34	30.57
4d.60.f	38.85	53.08	64.12	**7d.30.r**	19.92	25.71	33.31
4d.60.r	39.67	56.9	70.7	**7d.45.f**	24.42	32.06	40.38
5d.30.f	20.02	25.05	35.07	**7d.45.r**	26.75	35.88	45.56
5d.30.r	19.75	26.54	35.03	**7d.60.f**	31.59	41.06	55.31
5d.45.f	25.69	32.48	41.4	**7d.60.r**	34.01	47.09	62.00

Table 6.7-Average Skin friction of micropile 1 (MPR with load type B)

.

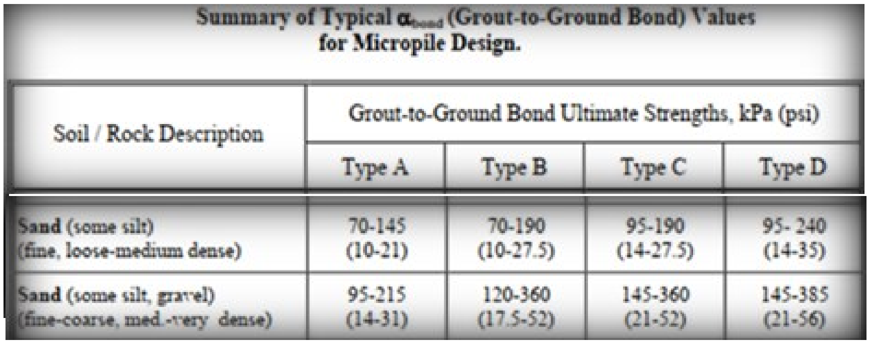

Summary of Typical α_{bond} (Grout-to-Ground Bond) Values for Micropile Design.

Soil / Rock Description	Grout-to-Ground Bond Ultimate Strengths, kPa (psi)			
	Type A	Type B	Type C	Type D
Sand (some silt) (fine, loose-medium dense)	70-145 (10-21)	70-190 (10-27.5)	95-190 (14-27.5)	95- 240 (14-35)
Sand (some silt, gravel) (fine-coarse, med.-very dense)	95-215 (14-31)	120-360 (17.5-52)	145-360 (21-52)	145-385 (21-56)

Table 6.8-Recommended values of skin friction (FHWA)

1. Micropiles’ end-bearing capacity to the total load capacity

On average, micropile toes took about 35% of the total load under this type of loading and no significant changes were observed as the spacing, raft stiffness, or sand relative density changed. However, this parameter was about 20% at the point defined as associated bearing capacity.

The ratio of end bearing to total load at settlement (kN/m^2)				**The ratio of end bearing to total load at settlement (kN/m2)**			
Sett (cm)	**5cm**	**10cm**	**15cm**	***Sett (cm)***	**5cm**	**10cm**	**15cm**
3d.30.f	35%	43%	44%	**5d.45.r**	33%	29%	41%
3d.30.r	38%	43%	43%	**5d.60.f**	31%	39%	41%
3d.45.f	32%	37%	40%	**5d.60.r**	32%	37%	39%
3d.45.r	32%	32%	37%	**6d.30.f**	34%	42%	45%
3d.60.f	26%	33%	36%	**6d.30.r**	35%	42%	44%
3d.60.r	23%	28%	31%	**6d.45.f**	34%	42%	44%
4d.30.f	32%	42%	44%	**6d.45.r**	34%	41%	42%
4d.30.r	33%	40%	42%	**6d.60.f**	32%	41%	43%
4d.45.f	32%	39%	42%	**6d.60.r**	33%	40%	41%
4d.45.r	32%	38%	40%	**7d.30.f**	33%	40%	42%
4d.60.f	27%	35%	40%	**7d.30.r**	34%	40%	41%
4d.60.r	28%	35%	38%	**7d.45.f**	33%	40%	41%
5d.30.f	32%	41%	44%	**7d.45.r**	34%	39%	40%
5d.30.r	34%	41%	43%	**7d.60.f**	32%	39%	40%
5d.45.f	32%	41%	43%	**7d.60.r**	32%	37%	39%

Table 6.9- Ratio of end-bearing capacity to the total load

6.5. Bending moment underneath the raft

The reinforcing system in the raft can be quite significant, with heavy reinforcing bar mats in the bottom, top, or both locations within the raft depth. To evaluate the effect of adding micropiles to a raft on the bearing moment at the bottom of the unpiled rafts, it was recorded at the settlement of 50, 75, 100, and 150 mm along with the values of the corresponding load. Then for the same values of bending moments in the micropiled-rafts, the corresponding bending moments were calculated.

A comparison of the bending moment under load A for the raft case to that of the raft within the MPR with the same geometrical characteristics shows that the micropiles had an untoward effect. In fact, under concentrated loads, the bending moment varied between 15% and 41% higher than that of unpiled rafts.

Even though there is no clear pattern in the rate bending moment changes with properties of the soil and MPR, it is apparent that as the spacing between the micropiles increased from 3d to

7d, the difference between the higher amount of bending moment of micropiled-raft and unpiled rafts decreased. This is probably due to the greater distance between the micropiles, which makes the behavior of micropiled-rafts similar to that of unpiled rafts.

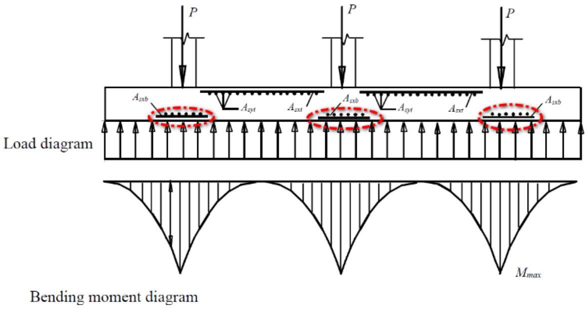

Fig. 6.44- Bending moment diagram underneath a raft

A. MPRs with load type A

The centrically loaded MPRs were different from the models in group B in which there was no micropile immediately below the concentrated load, whereas here, a micropile is located under the load coaxially. Therefore, the bending moment distribution is expected to be dissimilar to the MPR with load type A. In this section, these cases are investigated.

The following graph (Fig. 6.45) compares the ratio of the maximum bending moment underneath the MPRs to their unpiled equivalents (s/d=3). At the settlement of 5cm, the MPRs with rigid rafts showed slightly larger ratios of moment underneath the raft. MPRs with rigid rafts experienced higher percentages, indicating a slightly worse behavior in regard to the bending moment. The smallest value belonged to MPR with the semi-flexible raft tested in loose sand.

Fig. 6.46, for the models with s/d=4, compares the ratio of the maximum bending moment underneath the MPRs to their unpiled equivalents. At the settlement of 5cm, the MPRs with rigid rafts showed slightly larger ratios of moment underneath the raft. MPRs with rigid rafts experienced higher percentages, indicating a slightly worse effect of bending moment. The smallest value belonged to MPR with the semi-flexible raft tested in loose sand.

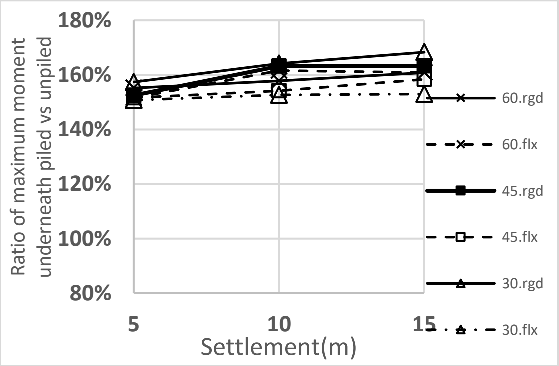

Fig. 6.45- Ratio of the maximum bending moment underneath the MPR to the unpiled equivalent (s/d=3, centric loading, A)

.

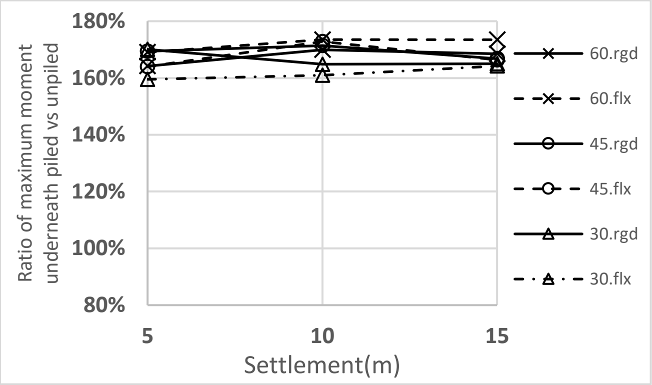

Fig. 6.46- Ratio of the maximum bending moment underneath the MPR to the unpiled equivalent (s/d=4, centric loading, A)

The ratio of the maximum bending moment underneath the MPRs to their unpiled equivalents (s/d=5) is compared in (Fig. 6.47). At the settlement of 5cm, the MPRs with rigid rafts showed slightly larger ratios of moment underneath the raft. Beyond the settlement of 5 cm, MPRs with semi-flexible rafts experienced higher percentages, indicating a slightly worse behavior in regard to the bending moment. Tested in dense sand, MPR with the rigid raft had the lowest value.

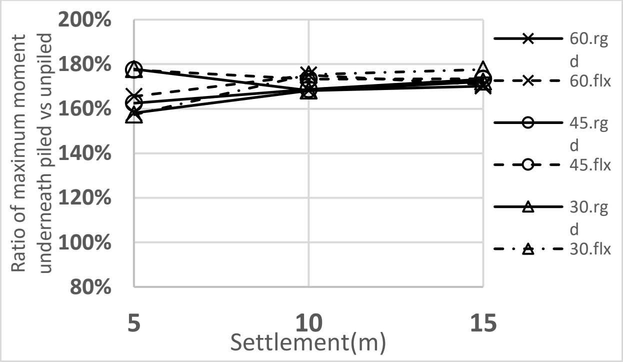

Fig. 6.47- Ratio of the maximum bending moment underneath the MPR to the unpiled equivalent (s/d=5, centric loading, A)

Fig. 6.48 compares the ratio of the maximum bending moment underneath the MPRs to their unpiled equivalents (s/d=6). The difference between the MPRs with different raft and sand bed stiffness in terms of bending moment became less noticeable.

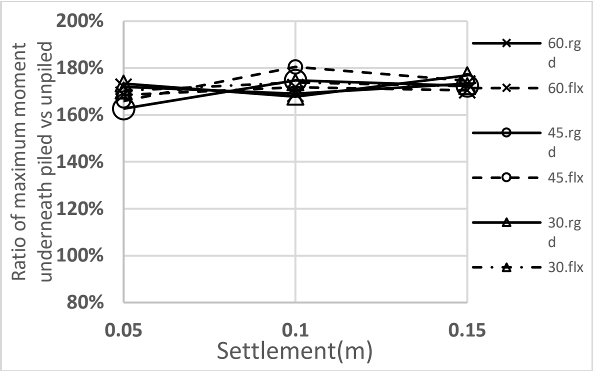

Fig. 6.48- Ratio of the maximum bending moment underneath the MPR to the unpiled equivalent (s/d=6, centric loading, A)

The following graph (Fig. 6.49) compares the ratio of the maximum bending moment underneath the MPRs to their unpiled equivalents (s/d=7). Compared to the MPRs, there was less difference in bending moment between the models.

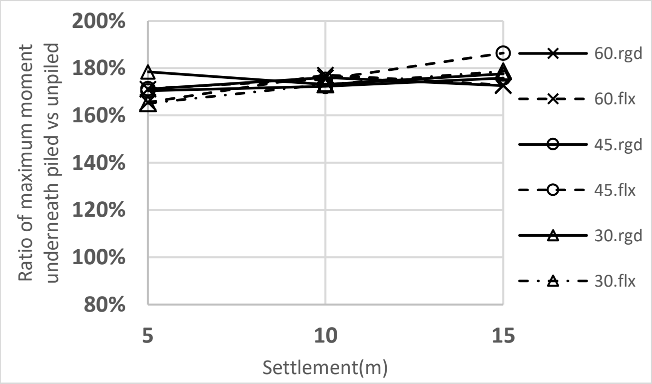

Fig. 6.49- Ratio of the maximum bending moment underneath the MPR to the unpiled equivalent (s/d=7, centric loading, A)

B. MPRs with Load type B

The following graph (Fig. 6.50) compares the ratio of the maximum bending moment underneath the MPRs to their unpiled equivalents (s/d=3). The higher percentage of the MPRs with semi-flexible rafts indicates that they suffer the adverse effect more than the MPRs with rigid rafts. These ratios stayed the same as the settlement increased.

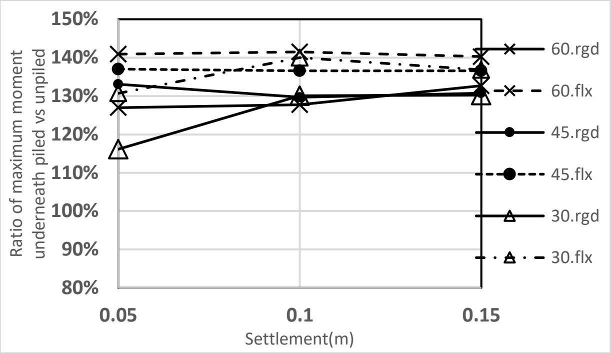

Fig. 6.50- Ratio of the maximum bending moment underneath the MPR to the unpiled equivalent (s/d=3, Loading B)

A graph depicting the ratio of maximum bending moments under MPRs to their unpiled counterparts (s/d=4) can be found in (Fig. 6.51). At the settlement of 5cm, the MPRs with rigid rafts showed larger ratios of moment underneath the raft. However, as the models sank more into the soil (sand), the higher percentage of the MPRs with semi-flexible rafts indicates that they suffer the adverse effect more than the MPRs with rigid rafts. These ratios stay the same as the settlement increases.

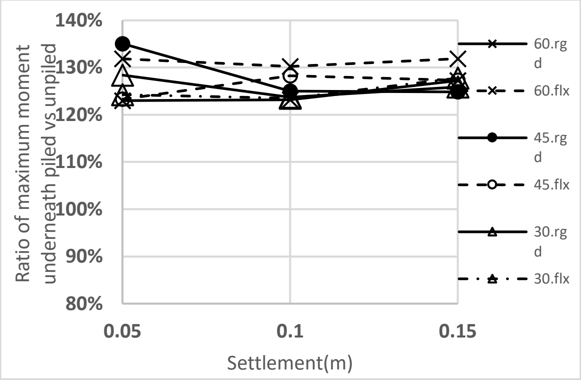

Fig. 6.51- Ratio of the maximum bending moment underneath the MPR to the unpiled equivalent (s/d=4, Loading B)

Below is a graph showing the ratio of the maximum bending moment under MPRs to their unpiled counterparts (s/d = 5). At the settlement of 5cm, the MPRs with rigid rafts showed slightly larger ratios of moment underneath the raft. However, as the models sank more into the soil (sand), the higher percentage of the MPRs with semi-flexible rafts indicates that they suffer the adverse effect more than the MPRs with rigid rafts except for the models in loose sand where the adverse effect of adding micropiles was less noticeable.

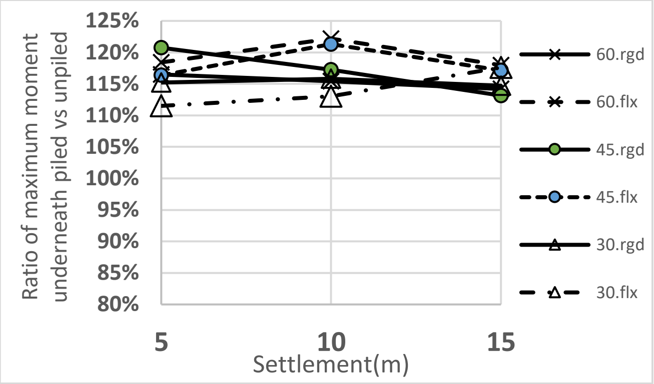

Fig. 6.52- Ratio of the maximum bending moment underneath the MPR to the unpiled equivalent (s/d=5, Loading B)

The following graph compares the ratio of the maximum bending moment underneath the MPRs to their unpiled equivalents (s/d=6). At the settlement of 5cm, the MPRs with rigid rafts showed slightly larger ratios of moment underneath the raft. However, as the models sank more into the soil (sand), the higher percentage of the MPRs with semi-flexible rafts indicates that they suffer the adverse effect more than the MPRs with rigid rafts except for the models in loose sand where the adverse effect of adding micropiles was less noticeable.

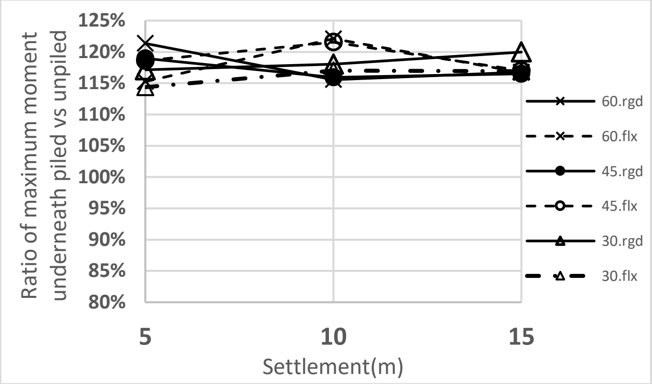

Fig. 6.53- Ratio of the maximum bending moment underneath the MPR to the unpiled equivalent (s/d=6, Loading B)

The following graph (Fig. 6.54) compares the ratio of the maximum bending moment underneath the MPRs to their unpiled equivalents (s/d=7). At the settlement of 5cm, the MPRs with rigid rafts showed slightly larger ratios of moment underneath the raft. However, as the models sank more into the soil (sand), the difference between the MPRs with semi-flexible rafts and rigid rafts was negligible.

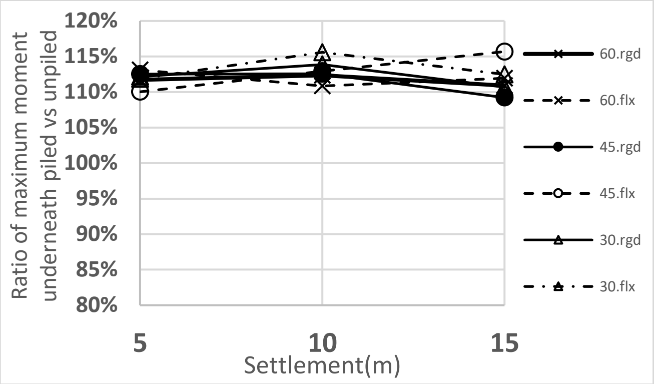

Fig. 6.54- Ratio of the maximum bending moment underneath the MPR to the unpiled equivalent (s/d=7, Loading B)

6.6.Pressure underneath the raft(contact pressure)

A. MPRs under load type A

Depending on the stiffness of a shallow footing, the distribution pattern of the contact pressure may vary. As described by Tharwat, under unfirm loading, the pressure beneath a semi-flexible raft will be uniform; but under rigid rafts, there must be a relatively large pressure under the center of the footing and no pressure at the edge (Tharwat, 2016). It could be safely assumed that the inclusion of micropiles will change the pressure distribution profile since the micropiles create rigid supporting points underneath the raft. To investigate this, a ratio of the maximum pressure under the unpiled raft at the settlement of 50,75,100, and 150 mm to that of the MPR at the same load levels of the unpiled version has been computed and depicted in the following graphs. A parameter (β) is defined as follows for the evaluation of adding micropiles.

$$\beta = 1 - \frac{\text{maximum pressure under the MPR at the settlement of 50,75,100 and 150mm}}{\text{Maximum pressure underneath the unpiled raft at the same loads}}$$

The 9-micro piled-raft (model A -with coaxial loading) is different from the sixteen micropiled (model B) versions because the load, in this case, is not applied in the middle of the raft but instead is coaxial with a micropile that might change the way contact pressure is distributed under the raft.

At s/d of 3, MPRs with semi-flexible rafts show a large percentage of decrease in the contact pressure compared to the unpiled rafts. At the initial stages of settlement, a minimum reduction of 72% is achieved. As the overall settlement rose from 50 mm to 100 and then 150mm, β decreased to 57%. In MPRs with rigid rafts, the foundations experienced a minimum drop of 55% at 150 mm of settlement (A-3d-R-60). However, for a smaller range of settlement, i.e., 50 to 100 mm, which is an acceptable range of overall settlement, this reduction in the contact pressure reached 60% for MPR in dense sand. This was slightly less for the MPR in the loose sand i.e. 55%.

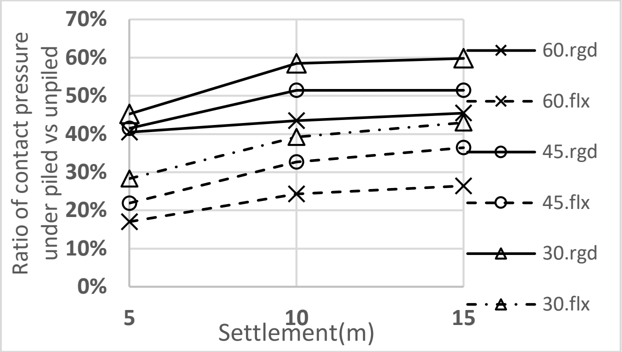

Fig. 6.55- Ratio of the maximum contact pressure underneath the MPR to the unpiled equivalent (s/d=3, Type A)

At s/d of 4, MPRs with semi-flexible rafts show (Fig. 6.56) a large percentage of decrease in the contact pressure compared to the unpiled rafts. At the initial stages of settlement, a maximum reduction of 58% was achieved. As the overall settlement rose from 50 mm to 100 and then 150mm, β decreased to 52%. In MPRs with rigid rafts, the foundations experienced a maximum drop of 31% at 150 mm of settlement (A-4d-R-60). However, for a smaller range of settlement, i.e., 50 to 100 mm, which is an acceptable range of overall settlement, this reduction in the contact pressure reached 45% for MPR in dense sand. This was slightly less for the MPR in the loose sand i.e. 44%.

In the next group, those with s/d of 5, MPRs with semi-flexible rafts show (Fig. 6.57) a large percentage of decrease in the contact pressure compared to the unpiled rafts. At the initial stages of settlement, a maximum reduction of 54% was achieved. As the overall settlement rose from 50 mm to 100 and then 150mm, β decreased to 41%. In MPRs with rigid rafts, the foundations experienced a maximum drop of 33% at 150 mm of settlement (A-5d-R-60). However, for a smaller range of settlement, i.e., 50 to 100 mm, which is an acceptable range of overall settlement, this reduction in the contact pressure reached 41% for MPR in dense sand. This value was lower for the MPR in the loose sand i.e. 35%.

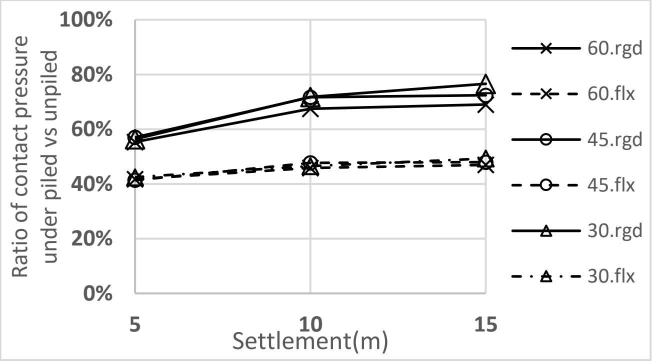

Fig. 6.56- Ratio of the maximum contact pressure underneath the MPR to the unpiled equivalent (s/d=4, Type A)

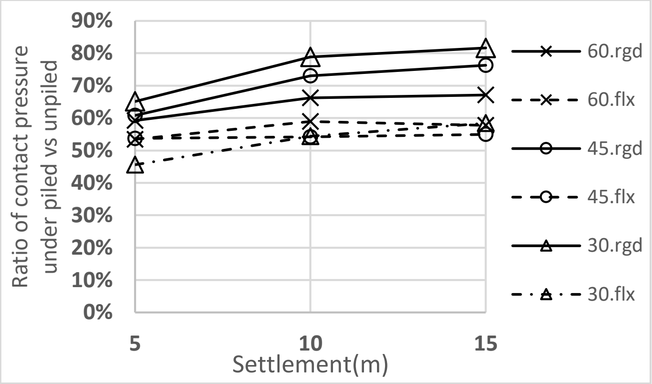

Fig. 6.57- Ratio of the maximum contact pressure underneath the MPR to the unpiled equivalent (s/d=5, Type A)

MPRs with semi-flexible rafts at s/d of 6 show a large percentage of decrease in the contact pressure compared to the unpiled rafts. At the initial stages of settlement, a maximum reduction of 42% was achieved. As the overall settlement rose from 50 mm to 100 and then 150mm, β decreased to 31% for A-6d-F-45 and 12% for A-6d-F-30. In MPRs with rigid rafts, the foundations experienced a maximum drop of 4% at 150 mm of settlement (A-6d-R-60). However, for a smaller range of settlement, i.e., 50 to 100 mm, which is an acceptable range of overall settlement, this reduction in the contact pressure reached the maximum of 36% for MPR in medium-dense sand.

At s/d of 7, MPRs with semi-flexible rafts show a large percentage of decrease in the contact pressure compared to the unpiled rafts. At the initial stages of settlement, a maximum reduction of 40% was achieved. As the overall settlement rose from 50 mm to 100 and then 150mm, β decreased to 23% for B-7d-F-45 and 12% for B-7d-F-30. In MPRs with rigid rafts, the foundations experienced a maximum drop of 4% at 150 mm of settlement (A-7d-R-60). However, for a smaller range of settlement, i.e., 50 to 100 mm, which is an acceptable range of overall settlement, this reduction in the contact pressure reached the maximum of 32% for MPR in medium-dense sand.

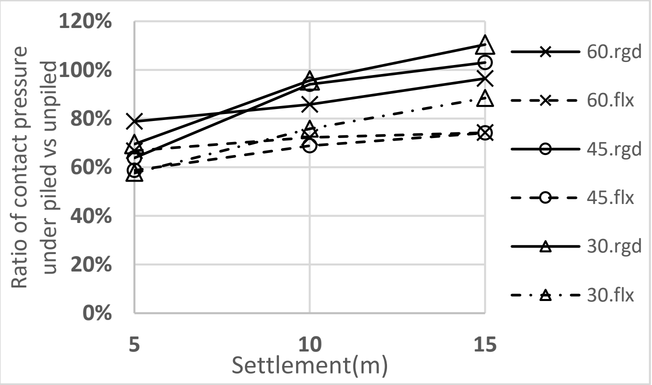

Fig. 6.58- Ratio of the maximum contact pressure underneath the MPR to the unpiled equivalent (s/d=6, Type A)

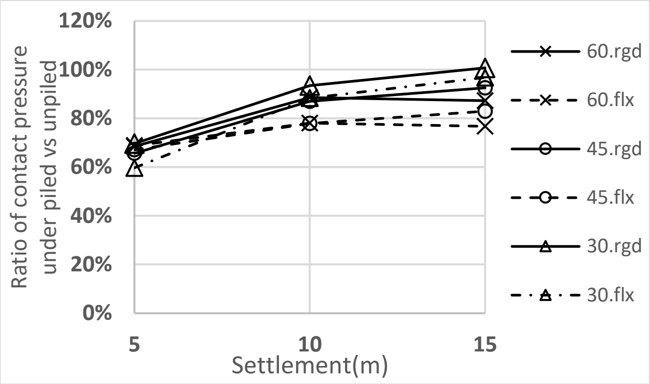

Fig. 6.59- Ratio of the maximum contact pressure underneath the MPR to the unpiled equivalent (s/d=7, Type A)

B. MPRs under load type B

For the MPRs with the micropile spacing ratio of 3, the contact pressure under the raft for the MPRs with semi-flexible rafts varied between 8% and 31% of the unpiled versions. This number for the ones with rigid rafts ranged from 25% to 38%. This means that the ones with semi-flexible rafts benefitted more in terms of reduction in contact pressure. β varied between 62% and 92% for the MPRs with semi-flexible rafts and between 62% and 75% for those with rigid rafts.

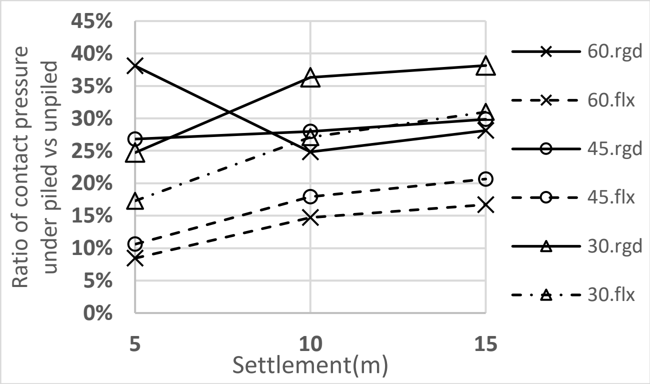

Fig. 6.60- Ratio of the maximum contact pressure underneath the MPR to the unpiled equivalent (s/d=3, loading type B)

For the MPRs with the micropile spacing ratio of 4, the contact pressure under the raft for the MPRs with semi-flexible rafts varied between 19% and 41% of the unpiled versions. This number for the ones with rigid rafts ranged from 45% to 61%. This means that the ones with semi-flexible rafts benefitted more in terms of reduction in contact pressure. β varied between 58% and 81% for the MPRs with semi-flexible rafts and between 39% and 55% for those with rigid rafts.

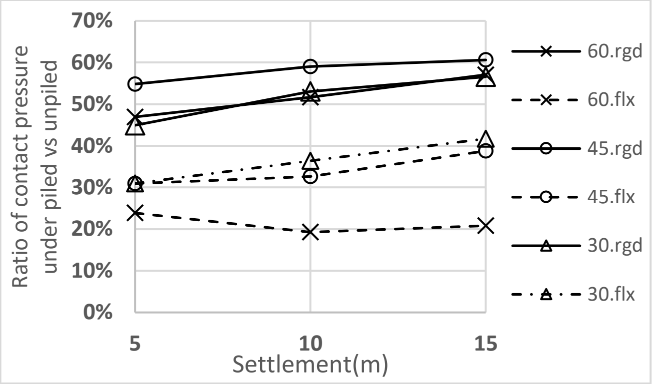

Fig. 6.61- Ratio of the maximum contact pressure underneath the MPR to the unpiled equivalent (s/d=4, loading type B)

At the micropile spacing ratio of 5 the MPRs with the micropile spacing ratio of 5, the contact pressure under the raft for the MPRs with semi-flexible rafts varied between 46% and 66% of the unpiled versions. This number for the ones with rigid rafts ranged from 40% to 56%. Therefore, those with semi-flexible rafts experienced a greater reduction in contact pressure. β varied between 58% and 81% for the MPRs with semi-flexible rafts and between 39% and 48% for those with rigid rafts.

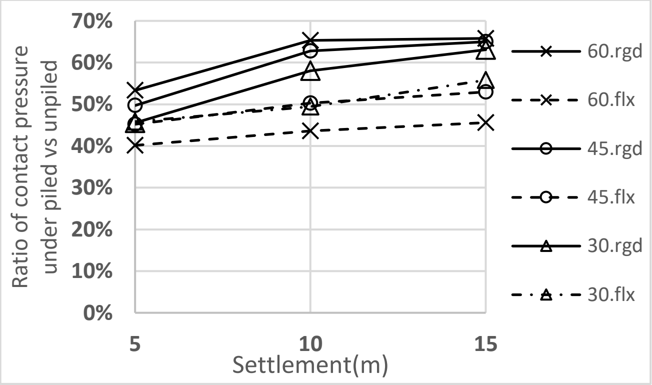

Fig. 6.62- Ratio of the maximum contact pressure underneath the MPR to the unpiled equivalent (s/d=5, loading type B)

For the MPRs with the micropile spacing ratio of 6, the contact pressure under the raft for the MPRs with semi-flexible rafts varied between 46% and 76% of the unpiled versions. This number for the ones with rigid rafts ranged from 45% to 59%. Thus, those with semiflexible rafts benefited more from the reduction in contact pressure. β varied between 58% and 81% for the MPRs with semi-flexible rafts and between 39% and 48% for those with rigid rafts.

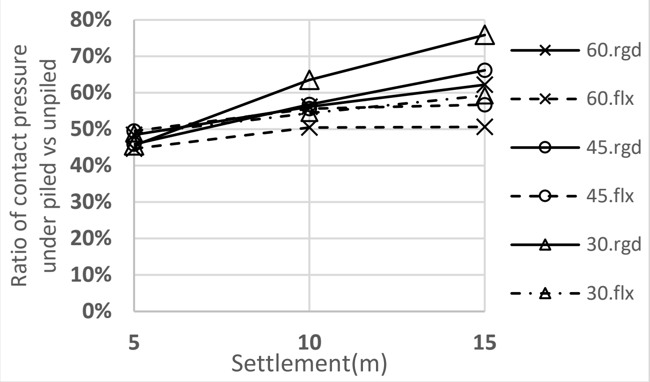

Fig. 6.63- Ratio of the maximum contact pressure underneath the MPR to the unpiled equivalent (s/d=6, loading type B)

For the MPRs with the micropile spacing ratio of 7, the contact pressure under the raft for the MPRs with semi-flexible rafts varied between 44% and 53% of the unpiled versions. This number for the ones with rigid rafts ranged from 44% to 55%. Semi-flexible rafts benefitted more in this regard compared to rigid rafts. β varied between 58% and 81% for the MPRs with semi-flexible rafts and between 39% and 48% for those with rigid rafts.

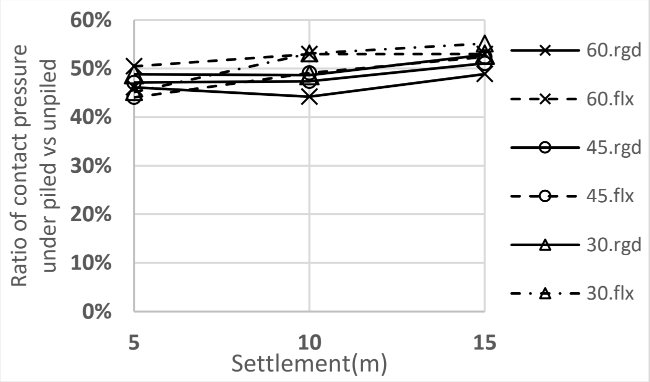

Fig. 6.64- Ratio of the maximum contact pressure underneath the MPR to the unpiled equivalent (s/d=7, loading type B)

6.7. Differential settlement

Uneven settlement of footings is caused by some form of shifting of the soil underneath the footing. It is essential to control the differential settlement in a foundation. This is because an excessive differential settlement will generate severe damage to the superstructure in terms of serviceability and safety. The main reasons that can lead to excessive differential settlement are weak bearing capacity of the soil, insufficient compaction, the existence of vegetation, and soil consolidation. In this section, the improvements in the differential settlement by the introduction of micropiles into the raft footing system are investigated.

To evaluate the effects of micropiles' presence on differential settlement, two series of models i.e., micropiled rafts and their unpiled equivalents were modeled and tested in Plaxis. For each model, the greatest and smallest amounts of the settlement generated in the models were recorded and subtracted from each other to calculate the value of the differential settlement. The ratio of the differential settlement in the piled MPR to the unpiled versions produced a dimensionless number representing the effectiveness of the micropiles.

A. MPRs under load A

To investigate the impact of different micropiles configurations at the overall settlement of 5,10, and 15 cm, the differential settlement values of the unpiled micropiled rafts were recorded. Next, at the equivalent values of the total load, the differential settlement values of the micropiled rafts were measured. And finally, the ratio of the maximum differential settlement in the MPRs to their counterparts was worked out. Results showed that differential settlement can be controlled by micropiles.

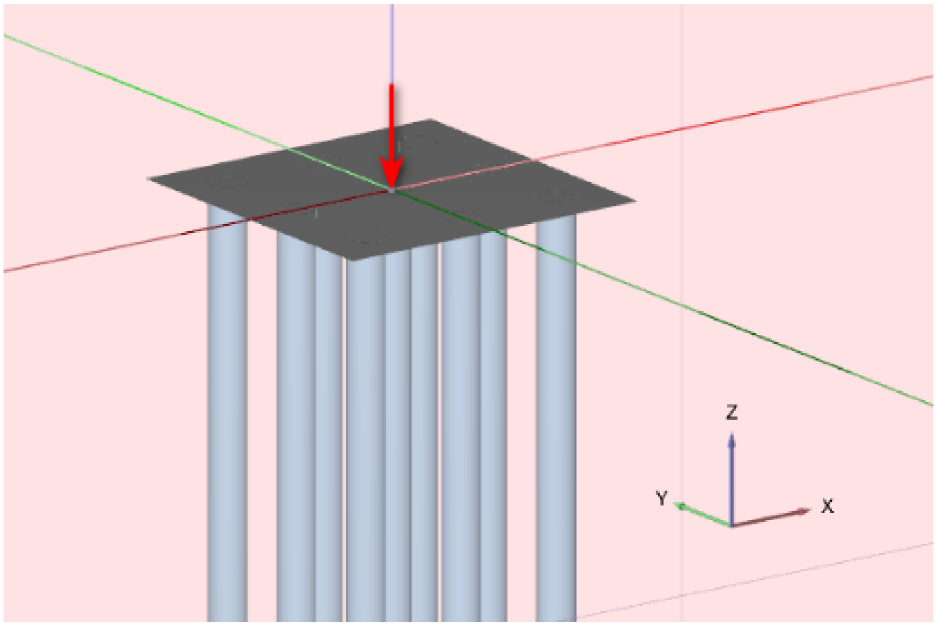

Fig. 6.65- Schematic view of the micropiled raft
(Load type A) with nine micropiles

The graph below (Fig. 6.66) shows the ratio of the maximum differential settlement in the MPRs with s/d=3 to that in the unpiled version. The reduction for the MPRs with semi-flexible rafts experienced a minimum of 41% and a maximum of 65%. This number for the ones with rigid rafts was between 33% and 40%.

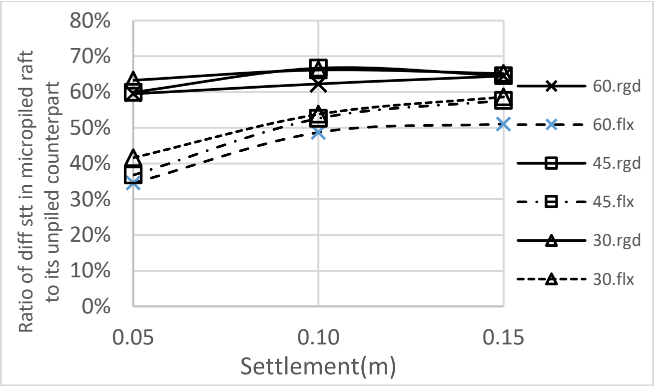

Fig. 6.66- Ratio of the maximum differential settlement of the MPR to the unpiled equivalent (s/d=3, centric loading A)

Fig. 6.67 shows the ratio of the maximum differential settlement in the MPRs with s/d=4 to that in the unpiled version. The reduction for the MPRs with semi-flexible rafts experienced a minimum of 27% and a maximum of 39%. This number for the ones with rigid rafts was between 21% and 40%.

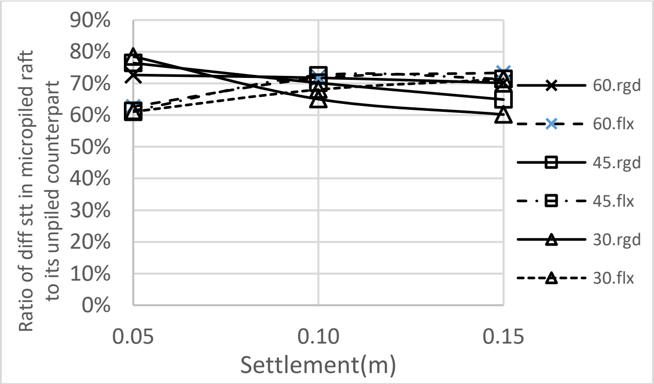

Fig. 6.67- Ratio of the maximum differential settlement of the MPR to the unpiled equivalent (s/d=4, centric loading, A)

This graph shows the ratio of the maximum differential settlement in the piled and unpiled versions of the MPRs (Fig. 6.68). Minimal reductions of 11% and maximum reductions of 32% were experienced by MPRs with semiflexible rafts. For rigid rafts, this number ranged between 26% and 57%.

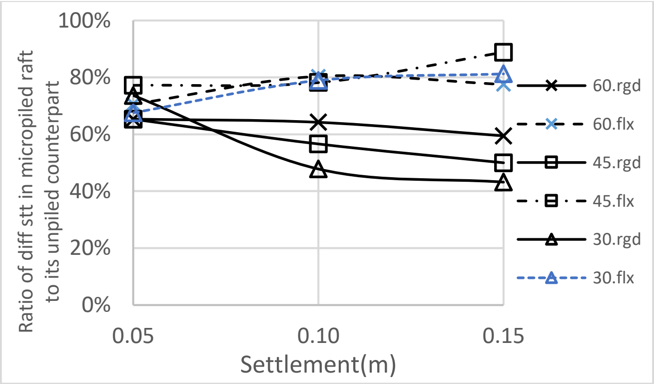

Fig. 6.68- Ratio of the maximum differential settlement of the MPR to the unpiled equivalent (s/d=5, centric loading, A)

The ratio of the maximum differential settlement in the MPRs with s/d=6 to that in the unpiled version is shown in Fig. 6.69. This reduction for the MPRs with semi-flexible rafts experienced a minimum of 15% and a maximum of 24%. This number for the ones with rigid rafts was between 36% and 74%.

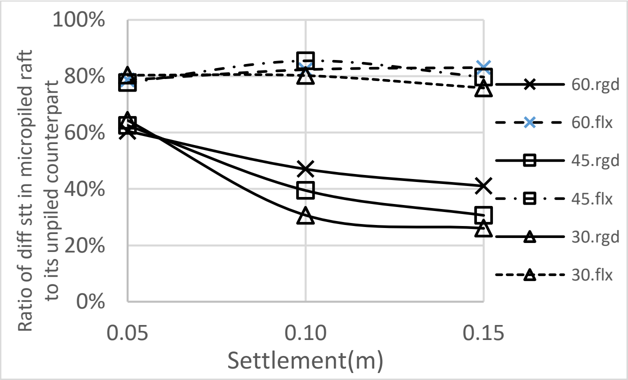

Fig. 6.69- Ratio of the maximum differential settlement of the MPR to the unpiled equivalent (s/d=6, centric loading, A)

The graph below (Fig. 6.70) shows the ratio of the maximum differential settlement in the MPRs with s/d=7 to that in the unpiled version. This reduction for the MPRs with semi-flexible rafts ranged from a minimum of 7% to a maximum of 25%. This number for the ones with rigid rafts was between 45% and 77%.

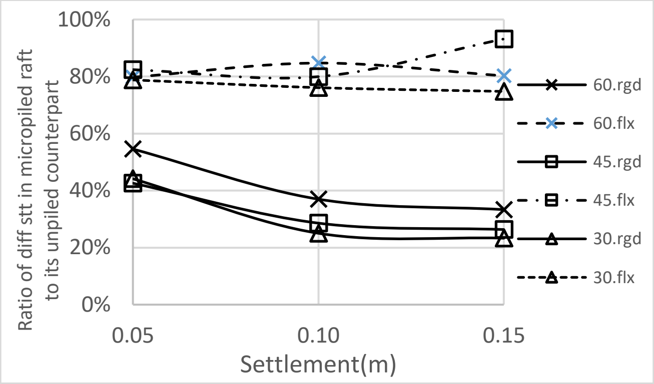

Fig. 6.70- Ratio of the maximum differential settlement of the MPR to the unpiled equivalent (s/d=7, centric loading, A)

B. *MPRs under load B*

In this section, FEM models of unpiled rigid and semi-flexible rafts with five different spacing (3d,4d,5d,6d, and 7d) in soils with different relative densities were compared against the equivalent MPR foundations. The schematic picture below depicts a deformed piled raft after it has undergone a maximum overall settlement of 15 cm at the center.

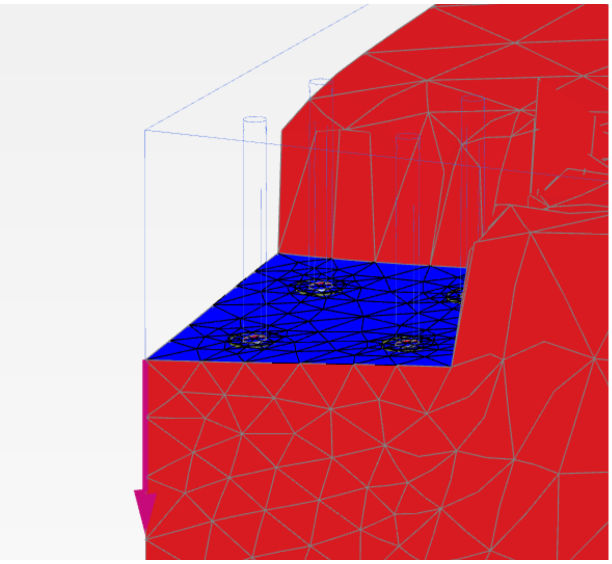

Fig. 6.71- - MPR with load model A, undergone the settlement

The graph below (Fig. 6.72) shows the ratio of the maximum differential settlement in the MPRs with s/d=3 to that in the unpiled version. This reduction for the MPRs with semi-flexible rafts experienced a minimum of 48% and a maximum of 67%. This number for the ones with rigid rafts was between 25% and 43%.

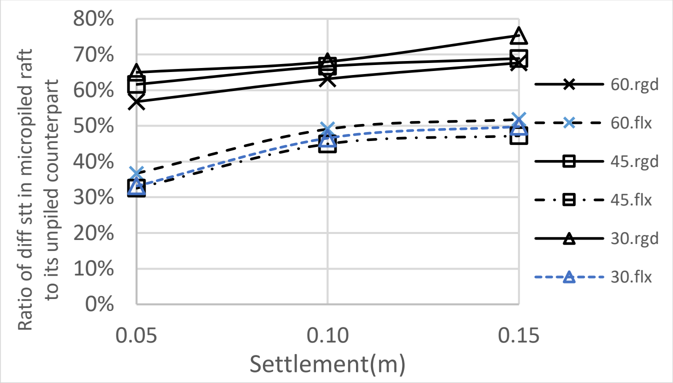

Fig. 6.72- Ratio of the maximum differential settlement of the MPR to the unpiled equivalent (s/d=3, loading type B)

The graph below (Fig. 6.73) shows the ratio of the maximum differential settlement in the MPRs with s/d=4 to that in the unpiled version. This reduction for the MPRs with semi-flexible rafts experienced a minimum of 36% and a maximum of 57%. This number for the ones with rigid rafts was between 24% and 35%.

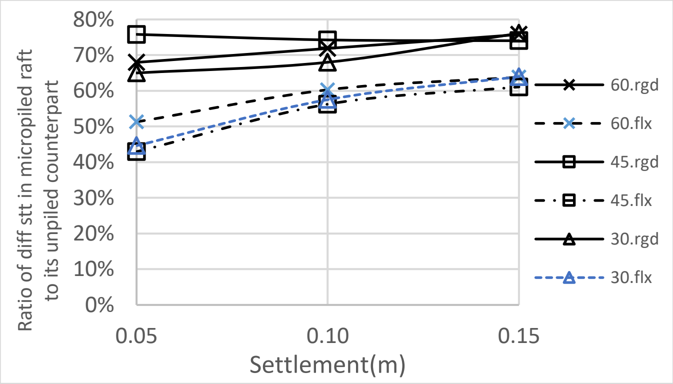

Fig. 6.73- Ratio of the maximum differential settlement of the MPR to the unpiled equivalent (s/d=4, loading type B)

The following graph (Fig. 6.74) shows the ratio of the maximum differential settlement in the MPRs with s/d=5 to that in the unpiled version. This reduction for the MPRs with semi-flexible rafts is between a minimum of 21% and a maximum of 38%. This number for the ones with rigid rafts was between 12% and 30%.

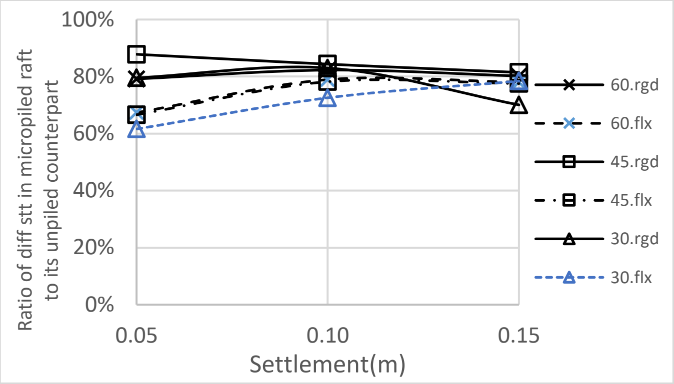

Fig. 6.74- Ratio of the maximum differential settlement of the MPR to the unpiled equivalent (s/d=5, loading type B)

As shown in Fig. 6.75, the maximum differential settlement in the MPRs with s/d=6 is compared to that in the unpiled version. For MPRs with semi-flexible rafts, this reduction ranged from 8% to 21%. This number for the ones with rigid rafts was negligible (no significant reduction in the differential settlement).

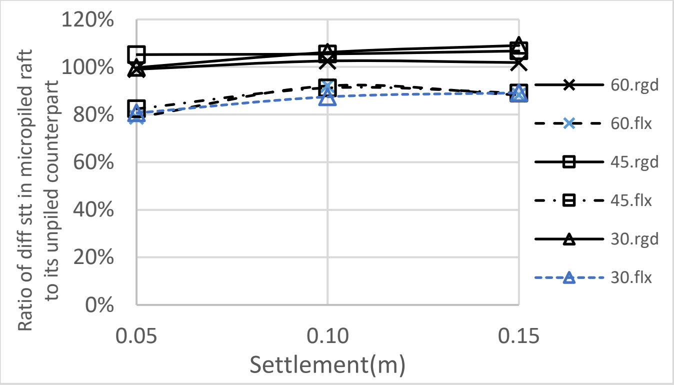

Fig. 6.75- Ratio of the maximum differential settlement of the MPR to the unpiled equivalent (s/d=6, loading type B)

The graph below (Fig. 6.76) shows the ratio of the maximum differential settlement in the MPRs with s/d=7 to that in the unpiled version. This reduction for the MPRs with semi-flexible rafts experienced a maximum of 8%. This number for the ones with rigid rafts was negligible (no significant reduction in the differential settlement).

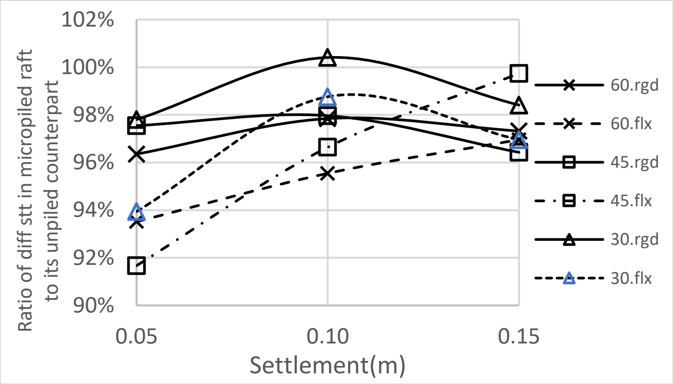

Fig. 6.76- Ratio of the maximum differential settlement of the MPR to the unpiled equivalent (s/d=7, loading type B)

6.8.Comparison between the axial stiffness of FEA models and the PDR method

The concept of axial stiffness of a piled raft foundation which is defined based on the initial part of the load-settlement curve is used for preliminary design purposes. However, generating this curve is a complicated process and needs powerful computers due to the complex nature of the interactions between the components of a micropiled-raft foundation. That is why some researchers have developed analytical models to predict the parameter to be used in the preliminary designs. Among them, the PDR (2001) method by Poulos, Davis, and Randolph is widely known and used. It has proved viable and accurate for the preliminary designs but has not been verified for designing the micropiled-rafts. The PDR method also does not necessarily consider raft thickness in calculating the raft.

To evaluate the suitability of the PDR method, the axial stiffness of all of the MPR models, with 9 and 16 micropiles (load A & load B), were computed from the load-settlement curves produced in Plaxis. The FEM modeling showed that the raft's thickness could change the load-settlement behavior to some degree, something that is not totally addressed in the PDR method (There is no restriction on the type of equation that can be used). To avoid this shortcoming, it is proposed to use other available formulas that consider the raft thickness in the calculations of the raft flexibility. This will be discussed in the next chapter. In the following sections, the outcome of the FEM models is compared against the values found using the PDR method.

A. MPRs with load type A

The results of the numerical models have been summarized in the tables below (Table 6.10& . Table 6.11). One can see the actual axial stiffnesses of the MPRs with semi-flexible rafts are 56% to 21% smaller than the computed stiffness by the PDR method under load A. When the semi-flexible rafts were replaced by rigid rafts, the situation improves slightly. However, for most models, the axial stiffness was still lower than the actual values except for a few models. The ratio indicated by "R" for these models is larger than 0.95 (Table 6.11).

The axial stiffness of the MPR (MN/m)										
Spacing	MPRs with Semi-flexible raft									
		30	Kr	R	45	Kr	R	60	Kr	R
3d	Actual value	75	99	**0.44**	90	99	**0.46**	105	94	**0.49**
	PDR method	170			193			215		
4d	Actual value	101	103	**0.59**	119	103	**0.62**	132	102	**0.61**
	PDR method	170			193			215		
5d	Actual value	110	105	**0.64**	129	105	**0.67**	148	105	**0.69**
	PDR method	170			193			215		
6d	Actual value	118	108	**0.69**	140	108	**0.72**	160	107	**0.74**
	PDR method	170			193			215		
7d	Actual value	125	112	**0.73**	161	112	**0.76**	170	112	**0.79**
	PDR method	170			193			215		
R: Ratio of the actual axial stiffness to the PDR method										

Table 6.10-Actual vs. the Computed stiffness of the MPR (load type A, semi-flexible rafts)

The axial stiffness of the MPR (MN/m)										
Spacing	MPRs with Rigid raft									
		30	Kr	R	45	Kr	R	60	Kr	R
3d	Actual value	92	998	**0.54**	113	978	**0.58**	137	960	**0.63**
	PDR method	170			193			215		
4d	Actual value	132	1023	**0.78**	161	1012	**0.83**	190	993	**0.88**
	PDR method	170			193			215		
5d	Actual value	140	1088	**0.83**	170	1076	**0.88**	203	1056	**0.94**
	PDR method	170			193			215		
6d	Actual value	146	1133	**0.86**	179	1120	**0.93**	214	1099	**0.99**
	PDR method	170			193			215		
7d	Actual value	152	1185	**0.89**	186	1173	**0.96**	222	1151	**1.03**
	PDR method	170			193			215		
R: Ratio of the actual axial stiffness to PDR method										

Table 6.11-Actual vs the Computed stiffness of the MPR (load type A, rigid rafts)

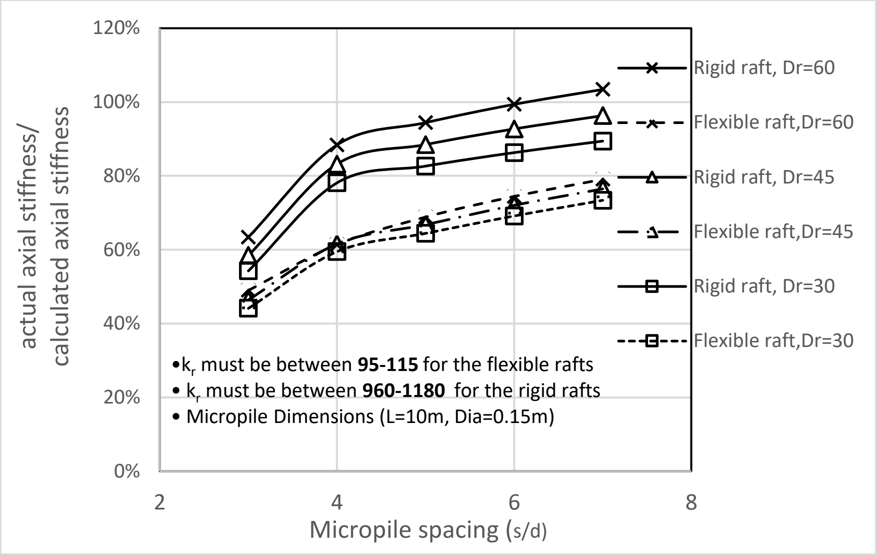

Fig. 6.77- Ratio of the actual stiffness to PDR (Centric loading, A)

B. MPRs with load type B

The same procedure was followed for the case where the concentrated load was acting coaxially with one of the micropiles (Fig. 5.5). The axial stiffness of this model in different densities of the sand and raft dimensions turned out to be more overestimated compared to the previous pattern of loading. It is shown that the actual numbers are 5% to 64% smaller than the computed stiffness by the PDR method.

The axial stiffness of the MPR (MN/m)										
Spacing		Semi-flexible raft								
		30	Kr	R	45	Kr	R	60	Kr	R
3d	Actual value	80.63	100	**0.36**	94	94	**0.37**	109	97	**0.38**
	PDR method	226			257			286		
4d	Actual value	105.23	103.26	**0.47**	122	102	**0.48**	139	100	**0.49**
	PDR method	226			257			286		
5d	Actual value	116.31	105.57	**0.51**	135	104	**0.53**	154	102	**0.54**
	PDR method	226			257			286		
6d	Actual value	123.54	108.71	**0.55**	143	107	**0.56**	164	105	**0.57**
	PDR method	226			257			286		
7d	Actual value	134.6	112.37	**0.60**	155	112	**0.60**	180	109	**0.63**
	PDR method	226			257			286		
R: Ratio of the actual axial stiffness to the PDR method										

Table 6.12_Actual vs. the Computed stiffness of the MPR (Loading type B, semi-flexible rafts).

The axial stiffness of the MPR (MN/m)										
Spacing	Rigid raft									
		30	Kr	R	45	Kr	R	60	Kr	R
3d	Actual value	110	988	**0.49**	133	977	**0.52**	160	960	**056**
	PDR method	226			257			286		
4d	Actual value	153	1023	**0.68**	184	1012	**0.72**	217	993	**0.76**
	PDR method	226			257			286		
5d	Actual value	165	1088	**0.73**	200	1076	**0.78**	237	1057	**0.83**
	PDR method	226			257			286		
6d	Actual value	176	1133	**0.78**	214	1120	**0.83**	254	1100	**0.89**
	PDR method	226			257			286		
7d	Actual value	188	1185	**0.84**	228	1172	**0.89**	272	1151	**0.95**
	PDR method	226			257			286		
R: ratio of the actual axial stiffness to PDR method										

Table 6.13-Actual vs. the Computed stiffness of the MPR (Loading type B, rigid rafts)

A comparison between FEM modeling and PDR methods shows that the axial stiffnesses calculated by PDR methods are all higher than those obtained by FEM methods (Fig. 6.78).

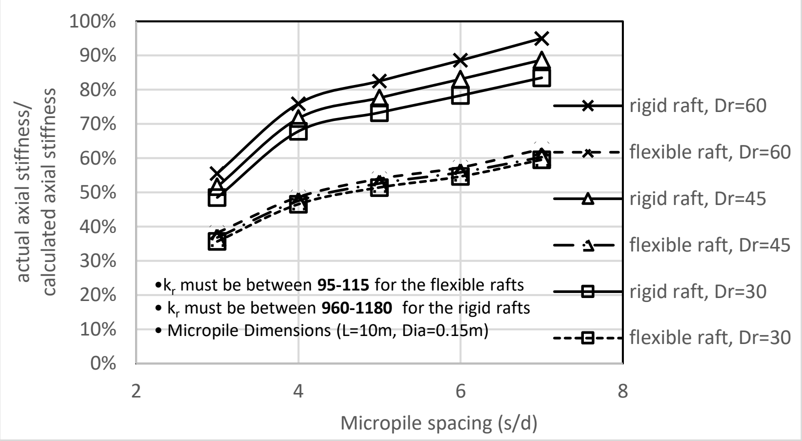

Fig. 6.78- Ratio of the actual stiffness to PDR (Loading B)

.

6.9.Load sharing between the component of the micropiled-raft foundation

During the experimental tests (Chapter 3), the effects of the important parameters, i.e., sand and raft stiffness, as well as micropile spacing ratios on the performance of the MPRs, were explored. In this section, the numerical simulation of different cases has been summarized in the following subsections according to the pile spacings. The effects of pile spacing, sand relative density, and raft stiffness have been examined.

As was the case with the PVC models, it is noted that as the soil (sand) gets stiffer, the micropiles can absorb a larger fraction of the total force thanks to the higher skin friction. As a result, the rafts get smaller shares of the total load. The opposite is true in loose sand because the micropiles could slip more easily within the soil compared to the denser sands, and therefore the rafts are left to carry a larger percentage of the total force. In the following sub-sections, the load-sharing mechanism is described in detail for each micropile spacing ratio.

A. Load sharing in MPRs type A

1. MPR with a concentric load (s/d=3)

Fig. 6.79 shows the behavior of MPRs with different raft flexibility (semi-flexible and rigid) in loose, medium, and dense sand. It is noted that as the foundation settles more into the sand, the micropiles in the MPR with semi-flexible rafts take larger portions of the load as opposed to those with rigid rafts. In model A-3d-Flx-60 functioning in the dense sand, the micropiles had to take 83% of the load at the settlement of 15 cm as compared to 68% for model A-3d-Flx-30. The difference between the MPRs with rigid rafts is however smaller. Model A-3d-R-60 transferred 54% of the total load to the micropiles, whereas model A-3d-Rgd-30 only transferred 46%. Furthermore, as the relative density of the sand increases, the micropile load portion increases, leaving a smaller percentage for the rafts to carry.

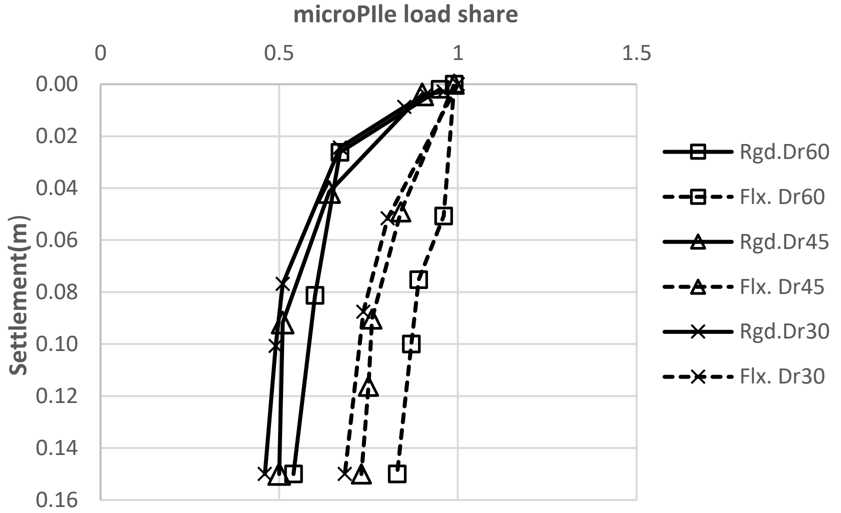

Fig. 6.79- micropiles shares of the total load (MPR with Load type A, s/d=3)

2. MPR with a concentric load (s/d=4)

The graph presented below (Fig. 6.80) shows the behavior of MPRs with different raft flexibility (semi-flexible and rigid) in loose, medium, and dense sand. One can see that as the foundation settles more into the sand, the micropiles in the MPR with semi-flexible rafts take larger portions of the load which is different than those with rigid rafts. In model A-4d-Flx-60 sitting in the dense sand, the micropiles had to take 57% of the load at the settlement of 15 cm as compared to 51% for model A-4d-Flx-30. The difference between the MPRs with rigid rafts is however smaller. Model A-4d-Rgd-60 transferred 45% of the total load to the micropiles, whereas model A-4d-Rgd-30 only transferred 41%. It is also evident that as the relative density of the sand goes up, the load portion of the micropiles increases leaving a smaller percentage for the rafts to carry.

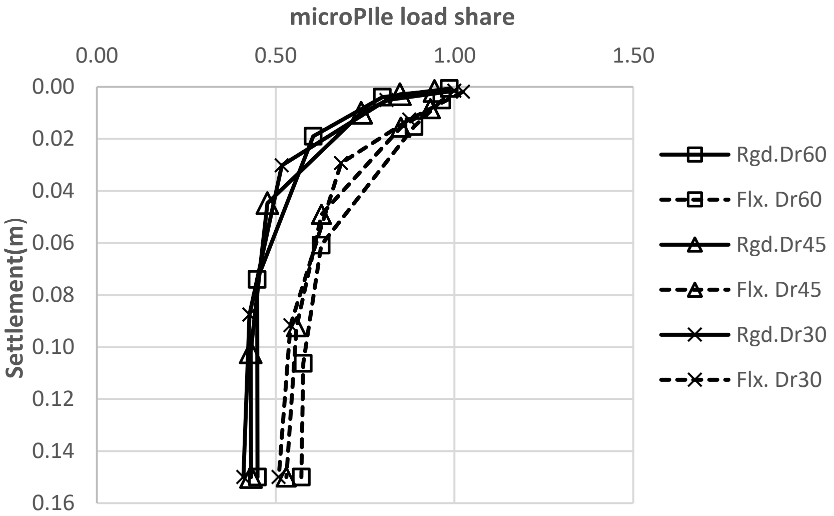

Fig. 6.80- micropiles shares of the total load (MPR with Load type A, s/d=4)

3. *MPR with a concentric load (s/d=5)*

Fig. 6.81 shows the behavior of MPRs with different raft flexibility (semi-flexible and rigid) in loose, medium, and dense sand. We see that as the foundation sinks more into the sand, the micropiles in the MPR with semi-flexible rafts have to carry larger portions of the load as opposed to those with rigid rafts. In model A-5d-Flx-60 functioning in the dense sand, the micropiles had to take 50% of the load at the settlement of 15 cm as compared to 46% for model A-5d-Flx-30. The difference between the MPRs with rigid rafts is however smaller. Model A-5d-Rgd-60 transferred 43% of the total load to the micropiles, whereas model A-5d-Rgd-30 only transferred 39%. Furthermore, as the relative density of the sand increases, the micropile load portion increases, leaving a smaller percentage for the rafts to carry.

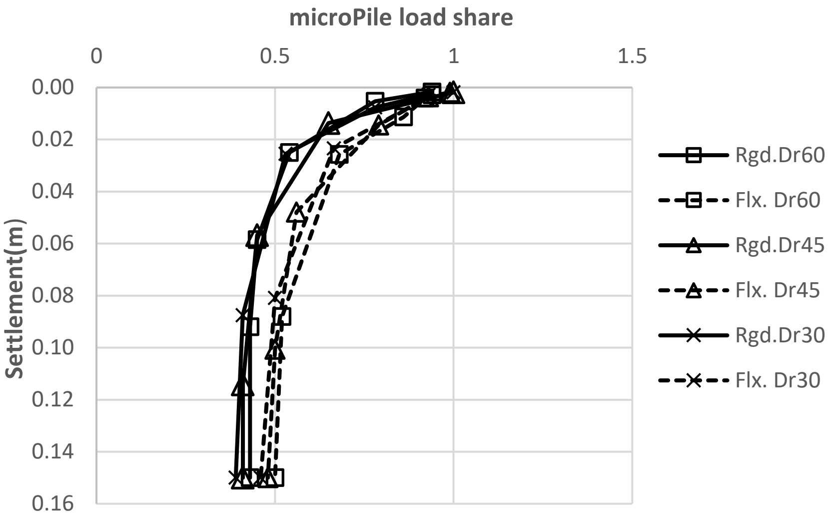

Fig. 6.81- micropiles shares of the total load (MPR with Load type A, s/d=5)

4. MPR with a concentric load (s/d=6 and 7)

The behavior of MPRs with different raft flexibility (semi-flexible and rigid) in loose, medium, and dense sand is shown (Fig. 6.82). It is shown that as the foundation settles more into the sand, the micropiles in the MPR with semi-flexible rafts have to carry larger portions of the load as opposed to those with rigid rafts. In model A-6d-F-60 functioning in the dense sand, the micropiles had to take 48% of the load at the settlement of 15 cm as compared to 46% for model A-6d-F-30. The difference between the MPRs with rigid rafts is however smaller. Model A-6d-R-60 transferred 43% of the total load to the micropiles, whereas model A-6d-R-30 transferred 40% of it. It is also evident that as the relative density of the sand ascends, the load portion of the micropiles increases leaving a smaller percentage for the rafts to carry. However, the rate of increase is slower compared to the MPRs with s/d=5. The graph also shows that there is no significant difference between the load shares of the micropiles of the MPRs with rigid and semi-flexible rafts.

The graph presented below (Fig. 6.83) shows the behavior of MPRs with different raft flexibility (semi-flexible and rigid) in loose, medium, and dense sand. It is noted that as the foundation settles more into the sand, the micropiles in the MPR with semi-flexible rafts have to carry larger portions of the load as opposed to those with rigid rafts. In model A-7d-F-60 functioning in the dense sand, the micropiles had to take 44% of the load at the settlement of 15 cm as compared to 39% for model A-7d-F-30. The difference between the MPRs with rigid rafts is however smaller. Model A-7d-R-60 transferred 48% of the total load to the micropiles, whereas model A-7d-R-30 only transferred 40%. It is also evident that as the relative density of the sand goes up, the load portion of the micropiles increases leaving a smaller percentage for the rafts to carry. However, the graph demonstrates that there is no significant difference between the load shares of the micropiles of the MPRs with rigid and semi-flexible rafts.

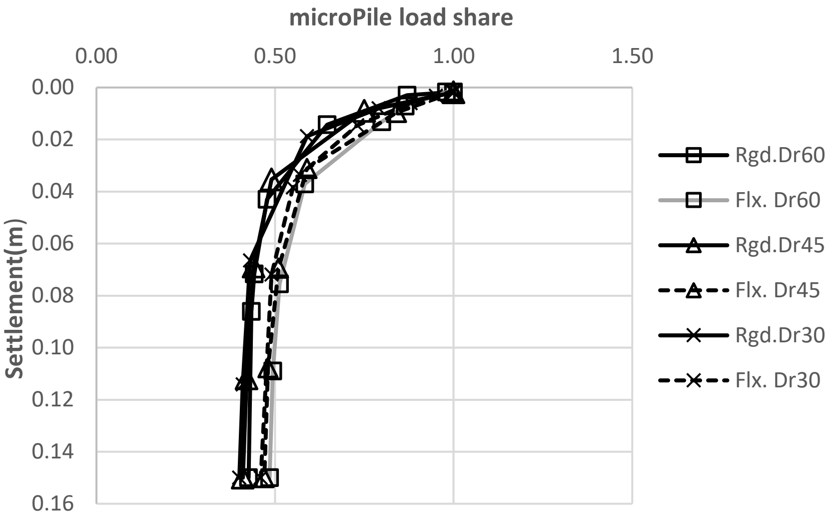

Fig. 6.82- micropiles shares of the total load (MPR with Load type A, s/d=6)

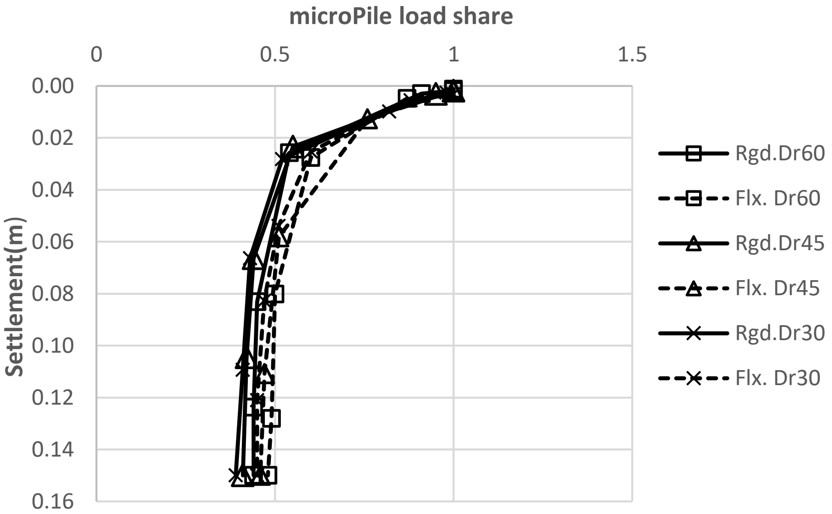

Fig. 6.83- micropiles shares of the total load (MPR with Load type A, s/d=7)

B. Load sharing in MPR type B

1. MPR (Spacing =3 d)

(Fig. 6.84) shows the load-settlement behavior of MPRs with different raft flexibility (semi-flexible and rigid) in loose, medium, and dense sand. It is noted that as the foundation settles more into the sand, the micropiles in the MPR with semi-flexible rafts have to carry larger portions of the load as opposed to those with rigid rafts. In model B-3d-F-60 functioning in the dense sand, the micropiles had to take 76% of the load at the settlement of 15 cm as compared to 61% for model B-3d-F-30. The difference between the MPRs with rigid rafts is however smaller. Model B-3d-R-60 transferred 53% of the total load to the micropiles, whereas model B-7d-R-30 only transferred 44%. It is also evident that as the relative density of the sand goes up, the load portion of the micropiles increases leaving a smaller percentage for the rafts to carry.

2. *MPR (Spacing =4 d)*

The graph presented below (Fig. 6.85) shows the behavior of MPRs with different raft flexibility (semi-flexible and rigid) in loose, medium, and dense sand. It is noted that as the foundation settles more into the sand, the micropiles in the MPR with semi-flexible rafts have to carry larger portions of the load as opposed to those with rigid rafts. In model B-4d-F-60 functioning in the dense sand, the micropiles had to take 74% of the load at the settlement of 15 cm as compared to 61% for model B-4d-F-30. The difference between the MPRs with rigid rafts is however smaller. Model B-4d-R-60 transferred 53% of the total load to the micropiles, whereas model B-4d-R-30 only transferred 44%. In addition, with the increasing density of the sand, the load portion of the micropiles increases, leaving the rafts with a smaller percentage to move.

Fig. 6.84- micropiles shares of the total load (MPR with load B, s/d=3)

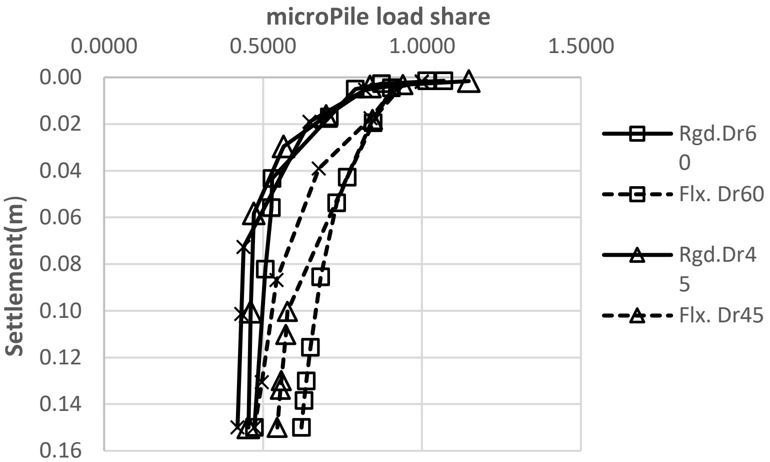

Fig. 6.85- micropiles shares of the total load (MPR with load B, s/d=4)

3. MPR (Spacing =5 d)

(Fig. 6.86) shows the behavior of MPRs with different raft flexibility (semi-flexible and rigid) in loose, medium, and dense sand. It is noted that as the foundation settles more into the sand, the micropiles in the MPR with semi-flexible rafts have to carry larger portions of the load as opposed to those with rigid rafts. In model B-5d-F-60 functioning in the dense sand, the micropiles had to take 53% of the load at the settlement of 15 cm as compared to 44% for model B-5d-F-30. The difference between the MPRs with rigid rafts is however smaller. Model B-5d-R-60 transferred 46% of the total load to the micropiles, whereas model B-5d-R-30 only transferred 41%. It is also evident that as the relative density of the sand goes up, the load portion of the micropiles increases leaving a smaller percentage for the rafts to carry.

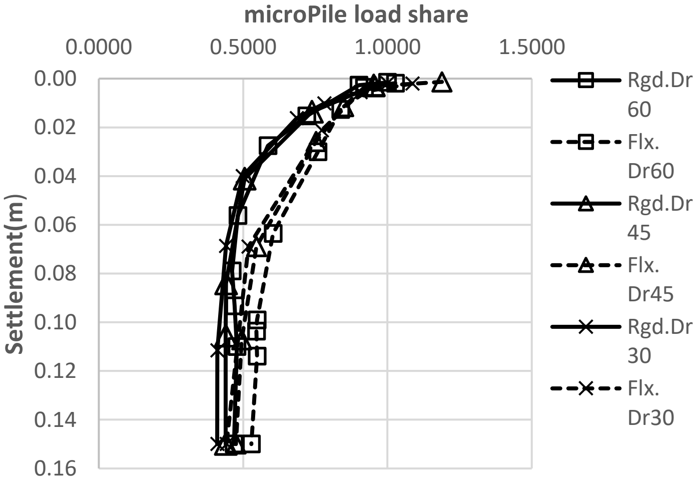

Fig. 6.86-micropiles shares of the total load (MPR with load B, s/d=5)

4. MPR (Spacing =6 d)

The graph presented below (Fig. 6.87) shows the behavior of MPRs with different raft flexibility (semi-flexible and rigid) in loose, medium, and dense sand. It is noted that as the foundation settles more into the sand, the micropiles in the MPR with semi-flexible rafts carry larger portions of the load as opposed to those with rigid rafts. In model B-6d-F-60 functioning in the dense sand, the micropiles had to take 47% of the load at the settlement of 15 cm as compared to 41% for model B-6d-F-30. The difference between the MPRs with rigid rafts is however smaller. Model B-6d-R-60 transferred 44% of the total load to the micropiles, whereas model B-6d-R-30 only transferred 39%. It is also evident that as the relative density of the sand goes up, the load portion of the micropiles increases leaving a smaller percentage for the rafts to carry. However, the graph demonstrates that there is no significant difference between the load shares of the micropiles of the MPRs with rigid and semi-flexible rafts.

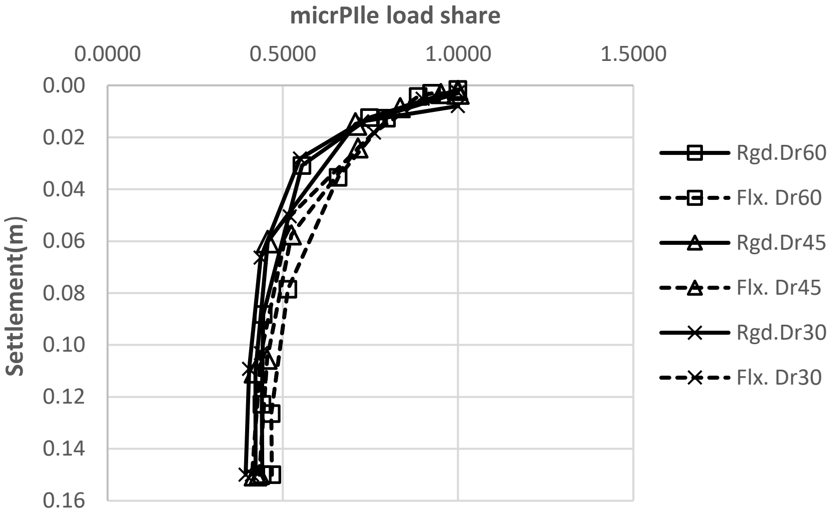

Fig. 6.87- micropiles shares of the total load (MPR with load B, s/d=6)

5. MPR (Spacing =7d)

Fig. 6.88 shows the behavior of MPRs with different raft flexibility (semi-flexible and rigid) in loose, medium, and dense sand. It is noted that as the foundation settles more into the sand, the micropiles in the MPR with semi-flexible rafts must carry larger portions of the load as opposed to those with rigid rafts. In model B-7d-F-60 functioning in the dense sand, the micropiles had to take 45% of the load at the settlement of 15 cm as compared to 39% for model B-7d-F-30. The difference between the MPRs with rigid rafts is very close to those with semi-flexible rafts. Model B-7d-R-60 transferred 44% of the total load to the micropiles, whereas model B-7d-R-30 only transferred 39%. It is also evident that as the relative density of the sand goes up, the load portion of the micropiles increases leaving a smaller percentage for the rafts to carry. However, the graph illustrates that load shares for rigid and semi-flexible rafts are not significantly different.

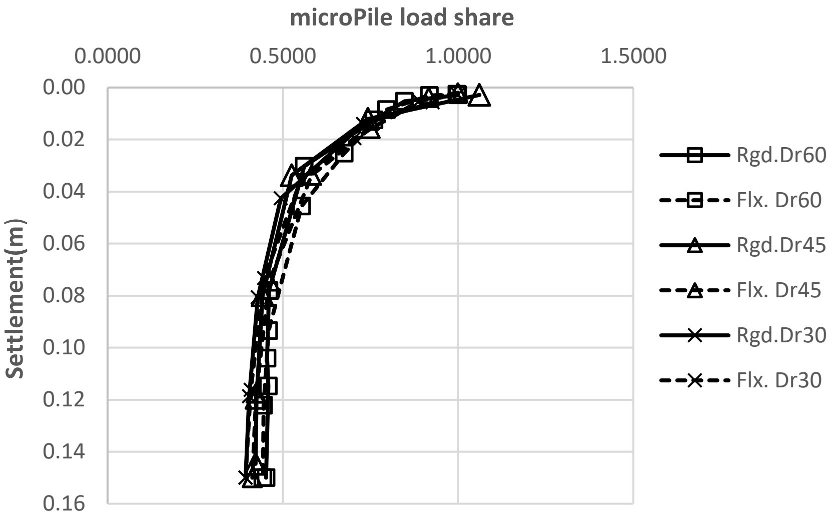

Fig. 6.88- micropiles shares of the total load (MPR with load B, s/d=7)

CHAPTER 7. ANALYTICAL MODEL

7.1.General

In 2001, Poulos. proposed his method for designing piled-raft foundations by combing his method with those of Davis and Randolph. This method offers an efficient way for preliminary design purposes. Designers could use this method to predict the load-settlement behavior of piled rafts based on the stiffness values of the raft and the piles and the specifications of the soil on which the foundation is laid.

For the calculation of the raft stiffness, the PDR method suggests using either of the two equations proposed by Polous and Davis (1974) (Equation 7.3) or Fraser and Wardle (1976)(Equation 7.5). However, it is worth noting that Equation 7.3 leaves out the raft thickness. However, Our study showed that the stiffness of the raft could affect the axial stiffness of the micropiled-raft foundations. Also, this method has been proposed for piled rafts where the piles are larger and the end bearing of the piles plays a large role in the load-bearing behavior.

In the PDR approach, the stiffness of the piled-raft foundation can be estimated from Equation 7.1. In this equation, K_{pr} is the stiffness of piled raft; K_r represents the stiffness of the unpiled raft (raft alone); K_{pg} is the pile group rigidity, and α_{rp} is the pile-raft interaction factor.

$$K_{pr} = \frac{K_{pg}+(1-2\alpha_{rp})K_r}{1-(\alpha_{rp}{}^2(K_r/K_{pg}))} \qquad \textit{Equation 7.1}$$

Where the raft-pile interaction factor, α_{rp}, can be estimated as follows:

$$\alpha_{rp} = 1 - \frac{ln\left(\frac{r_c}{r_0}\right)}{\zeta} \qquad \text{Equation 7.2}$$

The stiffness of the raft (unpiled) can be calculated using the expression developed by Poulos and Davis in 1974 (K_r = Pr /ω =βz√BW(2Gs/1-νs)). In this equation, β_z is the influence factor computed based on the rectangle's proportions. For a square raft, β is equal to 1.05. B and W are the length and width of the raft. ν_s is the soil Poisson ratio, and G_{sr} is the soil shear modulus. P_r is the total load carried by the foundation, and ω denotes the settlement, while ω refers to the settlement.

$$K_r = \mathrm{P_r} / \omega_r = \beta_z \sqrt{BW} (\frac{2G_{sr}}{1-\nu_s})$$

Equation 7.3 – Raft stiffness (Poulos and Davis,1974)

The pile group stiffness can be estimated via elastic theory by approaches such as those described by Poulos & Davis (1980), Fleming et al. (1992), or Poulos (1989). The stiffness of a single pile is computed similarly from elastic theory and then corrected using the group efficiency factor.

$$K_p := \frac{G_{s1} \cdot r_0 \cdot \left(\frac{4 \cdot \eta}{\left(1 - \nu_s\right) \cdot \xi} + \left(\frac{2 \cdot \boldsymbol{\pi} \cdot \rho}{\zeta} \right) \cdot \left(\tanh\left(\mu \cdot L\right) \cdot \frac{1}{\mu \cdot L} \right) \cdot \left(\frac{L}{r_0} \right) \right)}{1 + \left(\left(\frac{4 \cdot \eta}{\boldsymbol{\pi} \cdot \lambda \cdot \left(1 - \nu_s\right) \cdot \xi} \right) \cdot \left(\frac{\tanh\left(\mu \cdot L\right)}{\mu \cdot L} \right) \cdot \left(\frac{L}{r_0} \right) \right)}$$

Equation 7.4-Stiffness of a single pile (Poulos,2001)

Where:

r_b- pile radius at the base

r_0- pile radius at the top

G_b-shear modulus of the level of the pile base

E_p- pile Young's modulus

G_l, ρ, ν – previously defined

Where r_c=average radius of pile cap (corresponding to an area equal to the raft area divided by the number of piles); r_0=radius of the pile; $\zeta=\ln(r_m/r_0)$; $r_m=\{0.25 + \xi\ [2.5\ \rho\ (1-\ \nu_{.s})-0.25]\times L$; $\xi=E_{sl}/E_{sb}$; $\rho=E_{sav}/E_{sl}$; ν=Poisson's ratio of soil; L=pile length; E_{sl}= soil Young's modulus at the level of pile tip; E_{sb}=soil Young's modulus of bearing stratum below pile tip; and E_{sav}=average soil Young's modulus along the pile shaft.

Equation 7.3 can be replaced with the following from Fraser and Wardle (1976), which takes into account the thickness of the raft.

$$K_r = 5.57\ \frac{E_r}{E_s} \frac{(1\text{-}\nu_s^2)}{(1\text{-}\nu_r^2)} \left(\frac{S_B}{S_L}\right)^{\alpha} \left(\frac{t}{S_L}\right)^3$$

Equation 7.5-(Fraser and Wardle (1976))

Where: *E_r = the raft Young's modulus; ν_r= raft Poisson's ratio = 0.2; t_r = raft thickness; and ν_s = soil Poisson's ratio =0.3; E_s = average soil elastic modulus at depth = 2Br/3; and α = optimal value = 0.5.*

As demonstrated in Fig. 6.78 and Fig. 6.77, the PDR method is inclined to overestimate the axial stiffness of the micropiled-raft foundation with different loading patterns. In this section, a correction factor (ψ) has been developed using the best curve fitting technique to adjust the axial stiffness values calculated by the PDR method to estimate the axial stiffness values (Equation 7.6).

These formulas are proposed to calculate the correction factors by considering the raft rigidity. Table 7.1 summarizes the coefficients that can define the corresponding polynomials to produce the final correction factor, i.e., ψ, based on the stiffness of the sands, micropiles spacings, and rafts stiffness.

$$K_{pr} = (\psi)\frac{K_{pg} + (1-2a_{rp})K_r}{1-(a_{rp}{}^2(K_r/K_{pg}))}$$

Equation 7.6_ Modified PDR equation

and

Correction coefficient: $\boldsymbol{\psi = a + b \times ln(\beta) + c \times \ln(Dr)}$ (β=s/d) & (30≤Dr≤60)

(Equation 7.7- Correction factor)

Type of loading	Loading Type, A		Loading type B	
coefficient\Raft stiffness	**95<Kr<120**	**960<Kr<1200**	**95<Kr<120**	**960<Kr<1200**
a	-0.13	-0.45	-0.07	-0.41
b	0.34	0.42	0.27	0.42
c	0.06	0.17	0.04	0.13

Table 7.1-Coefficients of the logarithmic equation (correction factor)

7.2.Load sharing

Previously the effects of different parameters such as the loading pattern, stiffness of the rafts, soil condition, and micropile spacing ratio on the loading process and the way the load is distributed between the MPR elements were explored.

One could see that as the soil got stiffer, the load share of the raft decreased. This can be explained by considering that the stiffer soils provide higher skin friction for the micropiles and, consequently, a higher bearing capacity which means that the raft will take smaller shares of the total load. Also, it was noted that increasing s/d has a meaningful effect on the load-sharing mechanism. We developed a series of curves based on the given data in the parametric study. These curves can be used for estimating the shares of each element in an MPR foundation, provided the condition is similar.

The software Matlab was used to define a set of logarithmic expressions for both of the loading patterns, type A and type B by the 3D curve fitting method. An attempt was made to keep the polynomial as simple as possible with the least number of terms involved (Fig. 7.1).

These polynomials take two variables, the spacing between the micropiles (S) and the settlement ratio (ω), to roughly determine the load share of the micropiles with the MPRs. The percentage of the load taken by the rafts would be the remainder in the subtraction of micropile share from 100%.

$$X = a + b.\ln(s) + c.\ln(\omega)$$

Where ω= settlement ratio; S=the micropile spacing to diameter (3≤S≤7); X: micropiles share of the total load, the coefficients a,b, and c are given in Table 7.2, and Table 7.3 according to the type of loading pattern.

	w Semi-flexible raft, Dr=30%	w Rigid raft, Dr=30%	w Semi-flexible raft, Dr=45%	w Rigid raft, Dr=45%	w Semi-flexible raft, Dr=60%	w Rigida raft, Dr=60%
a	0.97415	0.4591	1.059	0.4926	1.29468	0.5142
b	-0.42470	-0.1986	-0.466	-0.1977	-0.56930	-0.1828
c	-0.12363	-0.1424	-0.123	-0.1312	-0.11150	-0.1168

Table 7.2-Coefficients for the MPRs with load A

	w Semi-flexible raft, Dr=30%	w Rigid raft, Dr=30%	W Semi-flexible raft, Dr=45%	w Rigid raft, Dr=45%	w Semi-flexible raft, Dr=60%	w Rigida raft, Dr=60%
a	0.73564	0.3735	0.8703	0.4346	0.9409	0.49786
b	-0.30585	-0.1541	-0.3543	-0.1732	-0.3397	-0.16908
c	-0.13359	-0.1502	-0.1233	-0.1450	-0.0993	-0.12408

Table 7.3- Coefficients for the MPRs the MPRs with Load B

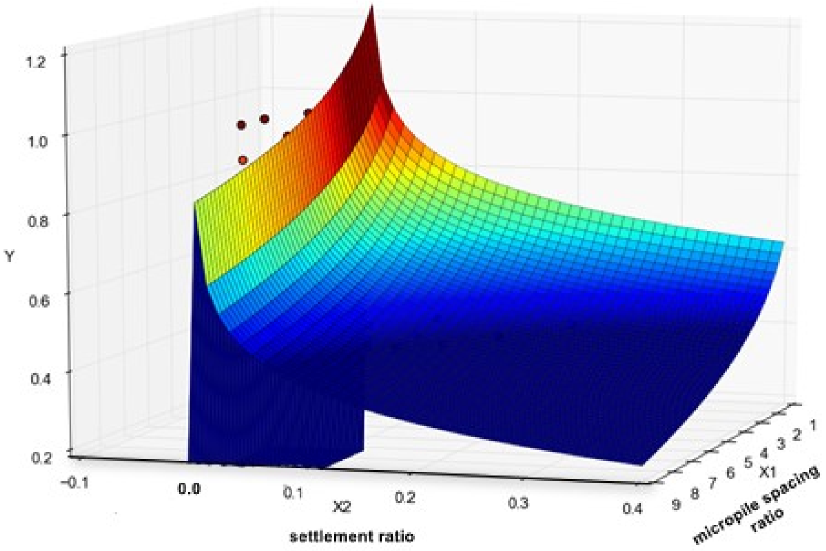

Fig. 7.1-3D best curve fitting (two variables)

7.3. Analytical model validation

In this section, some comparisons are made to verify the validity of the methods proposed for estimating the axial stiffness of MPR foundations.

(Kim, et al., 2018), in their study carried out numerical modeling tests on nine micropiled-rafts models in the sand. A square raft modeled in the FE analyses consists of a width (B_r) of 5 m and nine micropiles with a length (L_p) and diameter (B_p) of 7 and 0.2 meters, respectively. The FE model measured 40 × 40 × 40 m, eight times wider than B_r and five times longer than L_p. Fig. 7.2 shows the types of foundations adopted in the FE analyses. Input soil properties adopted in their FE analysis for different relative densities (D_R) are given in Table 7.5.

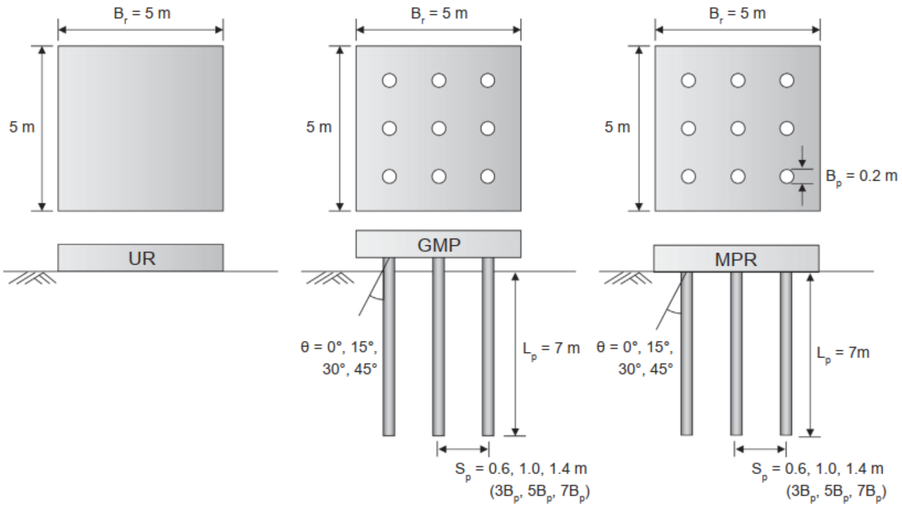

(a) (b) (c)

Fig. 7.2-Type of foundation adopted in FE analysis: (a) unpiled raft, (b) group micropile, and (c) micropiled raft.(Kim et al., 2017)

.

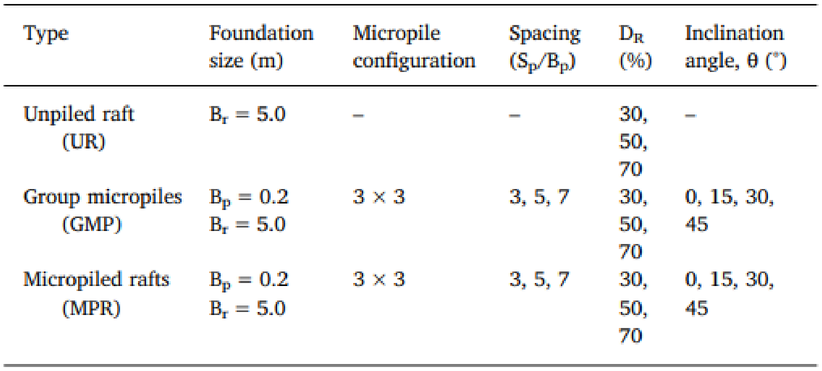

Type	Foundation size (m)	Micropile configuration	Spacing (S_p/B_p)	D_R (%)	Inclination angle, θ (°)
Unpiled raft (UR)	$B_r = 5.0$	–	–	30, 50, 70	–
Group micropiles (GMP)	$B_p = 0.2$ $B_r = 5.0$	3 × 3	3, 5, 7	30, 50, 70	0, 15, 30, 45
Micropiled rafts (MPR)	$B_p = 0.2$ $B_r = 5.0$	3 × 3	3, 5, 7	30, 50, 70	0, 15, 30, 45

Table 7.4-Foundation conditions in FE analysis.(Kim et al., 2017)

.

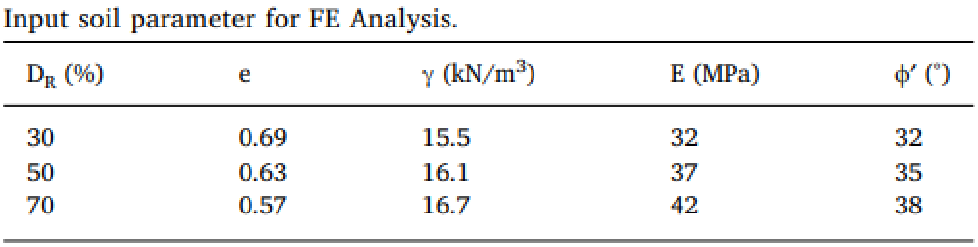

Input soil parameter for FE Analysis.

D_R (%)	e	γ (kN/m^3)	E (MPa)	ϕ' (°)
30	0.69	15.5	32	32
50	0.63	16.1	37	35
70	0.57	16.7	42	38

Table 7.5- Input soil parameter for FE Analysis.

Their study final output was compared against the data gathered from a full-scale test by Kyung (2017). As demonstrated in Fig. 7.3, the accuracy of the results was adequate.

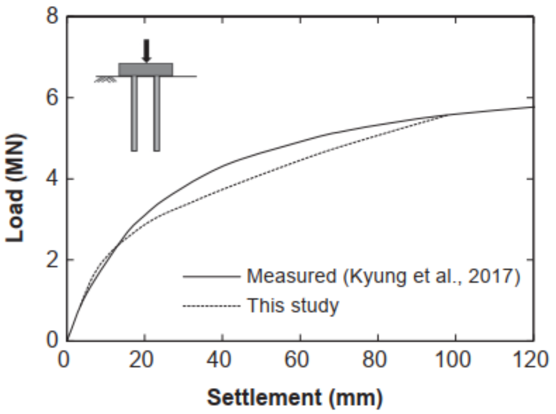

Fig. 7.3-Measured and calculated load-settlement curves of the piled raft. (Kim et al., 2017)

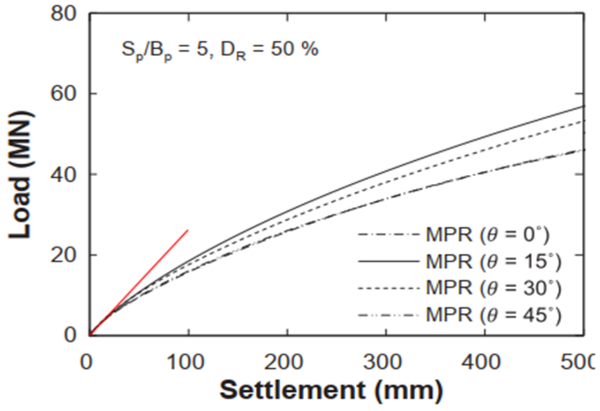

(c)

Fig. 7.4-Load-settlement curves of micropiled raft (Kim et al., 2017)

The graph above can be used to estimate the axial stiffness of one of the MPRs with s/d=5 in the sand with Dr=50% (Fig. 7.4) as follows:

$$Axial\_stiffness = \frac{\text{Maximum load (elastic zone)}}{\text{corresponding settlement}} = \frac{23\times10^{6}}{100\times10^{-3}\times10^{6}} = 230 \text{ MN/m}$$

To investigate the accuracy of our analytical models, the axial stiffness of the above model can be calculated using PDR and by implementing the properties listed above (soil and the models). Based on these calculations, the axial stiffness is calculated as 208 MN/m. From Table 6.11, the value of the proposed correction factor (ψ) is found to be 1.05 (s/d=5, Dr~45%), so the corrected axial stiffness of the model based on the PDR would be 220 (after correction). The error is therefore calculated to be 4%.

(Kyung, et al., 2016) performed some laboratory tests on micropiles and MPRs. They then verified the results from the experimental tests with field testing. The schematic below presents the detailed load test configuration used in the field tests. Accordingly, the following graph demonstrates the load-settlement curves obtained in the tests.

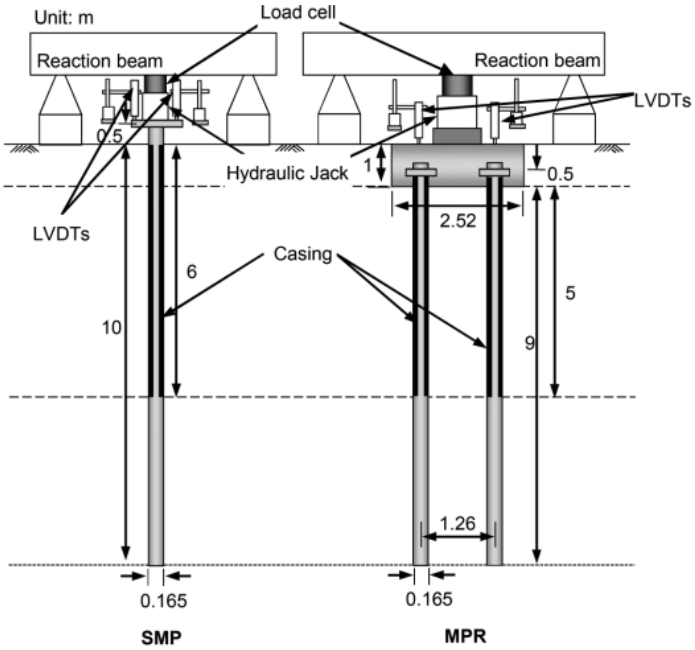

Fig. 7.5-Field test (Kyung, et al., 2016)

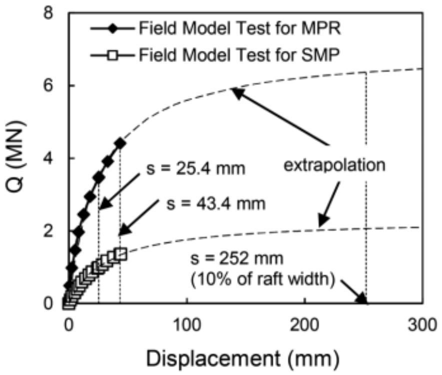

.

Fig. 7.6-comparison between the numerical and experimental models (Kyung, et al., 2016)

From Fig. 7.6 the axial stiffness could be obtained by finding the slope of the initial part of the curve. By doing that, it is found to be 200 MN/m. The PDR method calculates this as 184. The correction factor of ψ=1 (s/d=8) modifies this number into 184, which is close enough to the actual value considering that the soil bed in addition to sand included clay.

The last research used for the verification of the findings of this research belongs to (Ateş, et al., 2021). They performed experimental and numerical investigations on the piled raft foundations. The properties of the sand have been summarized in (Table 7.6).

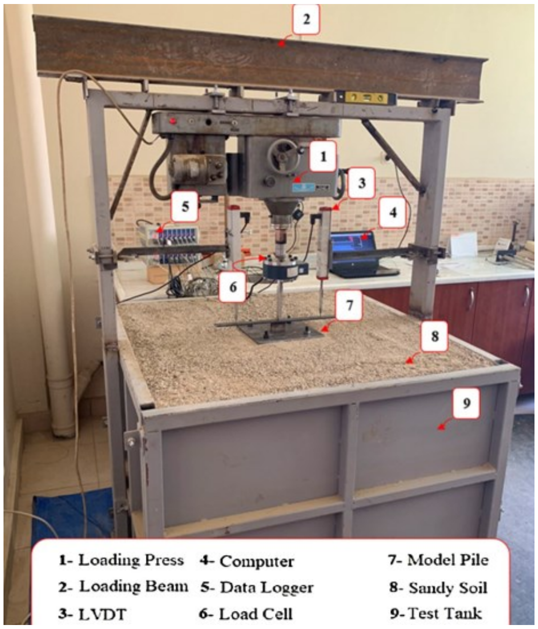

Fig. 7.7- Experimental test setup ((Ateş, et al., 2021))

.

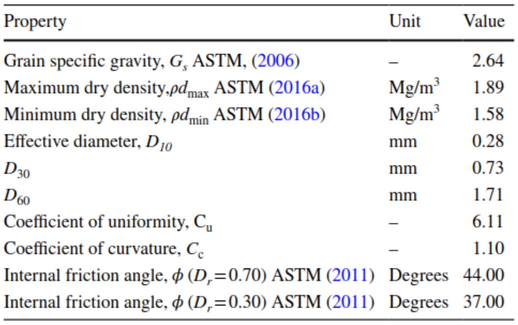

Property	Unit	Value
Grain specific gravity, G_s ASTM, (2006)	–	2.64
Maximum dry density, ρd_{max} ASTM (2016a)	Mg/m^3	1.89
Minimum dry density, ρd_{min} ASTM (2016b)	Mg/m^3	1.58
Effective diameter, D_{10}	mm	0.28
D_{30}	mm	0.73
D_{60}	mm	1.71
Coefficient of uniformity, C_u	–	6.11
Coefficient of curvature, C_c	–	1.10
Internal friction angle, ϕ (D_r=0.70) ASTM (2011)	Degrees	44.00
Internal friction angle, ϕ (D_r=0.30) ASTM (2011)	Degrees	37.00

Table 7.6- properties of sand (Ateş, et al., 2021)

.

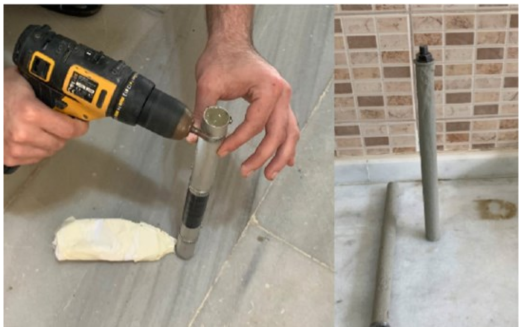

Fig. 7.8-placing concrete in aluminum mold (Left), model pile (Right)- (Ateş, et al., 2021)

.

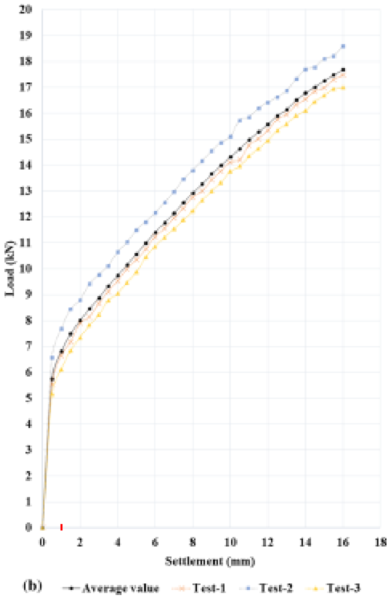

Fig. 7.9-The load-settlement curves for Dr = 70% L = 300 mm (s/d=4) (Ateş, et al., 2021)

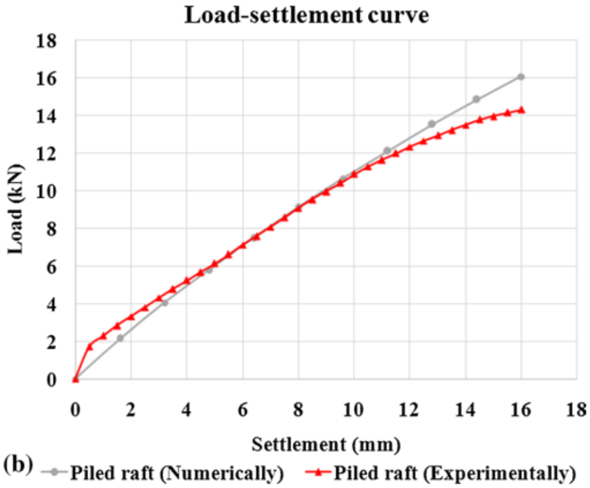

Fig. 7.10-comparison between the numerical and experimental models(Ateş, et al., 2021)

The physical model pile lengths (L) and diameter were given as (200 mm, 300 mm), and 20 mm, respectively. They used aluminum molds to build the model piles. To obtain actual soil-concrete friction behavior between the model pile and sand, concrete and steel bars were used to prepare the composite piles. The numerical analysis was conducted using ABAQUS.

The axial stiffness of this model based on Fig. 7.9 is determined to be ($5.7\times10^{3}\times10^{-6}/0.5\times10^{-3}$) =11.4 MN/m. Using the PDR method, this value is calculated to be 16.41MN/m. Based on the equations defined earlier the correction factor is found: ψ=0.73 (s/d=4, Rigid raft, loading A). The final result would be 11.98 MN/m which agrees with the number found from the actual loading-settlement curve.

Adjusted axial stiffness × correction factor: $16.41\times 0.73 = 11.98$ MN/m

CHAPTER 8. CONCLUSION AND RECOMMENDATION

8.1.General

The purpose of this dissertation was to investigate the behavior of micropiled-raft foundations in the sand and the load settlement mechanism. The effects of different parameters such as sand relative density, micropile to diameter spacings, raft stiffness, and different locations of concentrated loading were studied in experimental and numerical modeling. In this chapter, a summary of the research is presented.

8.2.Thesis summary

Various experimental tests were conducted on unpiled rafts, single micropiles, and MPR models in the geotechnical engineering laboratory. Based on the outcomes of the experimental investigation, additional FEM models were built. The results were then categorized and analyzed to achieve a better understanding of the behavior of MPRs in the sand. The actual axial stiffnesses of the MPR models were compared against the anticipated values obtained from the PDR method. A series of expressions were developed for adjustment of the MPR method when used for MPR cases. The load-sharing mechanism was also investigated and the relationships were established. The following conclusions were drawn from these analyses:

1. Micropiles significantly increased the overall load capacity of the MPR foundations. In the case of prototype models with loading type A (coaxial), this increase in the bearing capacity experienced a minimum of 60%. Load type B had the smallest improvement of 53%.
2. MPRs with rigid rafts take more load than semi-flexible rafts for any given settlement. However, when the pointed load is applied coaxially with a micropile (Case A), the difference between the behavior of MPRs with rigid and semi-flexible rafts is negligible.
3. The differential settlement was not greatly affected by sand bed stiffness. However, a higher relative density of the soil bed resulted in a lower overall settlement of the MPRs.
4. The load-sharing mechanism is affected by all three tested parameters. i.e. relative density, raft thickness, and micropile spacing ratio. Among them, the latter is the most dominant.
5. The micropiles share of the total load decreases as the spacing ratio gets larger. This is due to the lower shaft resistance of the micropiles. Also, it was observed that the micropiles share of the total load increased by the relative density of the sand.
6. The recommended skin friction values by FHWA were in fair agreement with the numbers obtained during the analysis but only under loading A (load applied coaxially with a micropile). However, these values are only achieved at the highest value of the settlement.
7. For loading type A, the ratio of the end-bearing capacity of the micropiles to their total load capacity was found to be about 10%. Under loading type B, this number was around

20%. This shows that the end-bearing capacity can be omitted from the total load capacity of the micropiles.

8. If a raft is thicker, differential settlements are minimized or eliminated. Yet, that may result in an excessive overall settlement as a result of unforeseen loads on the micropiles.
9. Differential settlement can be adequately dealt with by adding micropiles to the rafts at certain locations. According to the data, the differential settlement can be reduced by 77%.
10. Contact pressure underneath the raft of a MPR is lower than the unpiled equivalent at the same load level. The maximum reduction observed was 90% in the MPRs subjected to the load at the centroid of the raft (Type B).
11. The bending moment, on the other hand, is higher in the MPRs. But the affected area is relatively small which makes it easy to apply needed reinforcements.
12. The PDR method tends to overestimate the axial stiffness of the MPRs under concentrated loads. This overestimation was higher for the MPRs with semi-flexible rafts. By applying a correction factor the results can be adjusted.

The proposed empirical and analytical models were validated against the available data from the field and experimental studies. The following assumptions should be considered and the conditions of a potential foundation should be checked against those assumptions. It was assumed that: the micropiles have the same size and behave similarly, the relative density of the soil stays unchanged along the micropiles, and the load is applied vertically.

8.3.Limitations of the current study and Recommendations for future studies

This research focused mainly on MPRs with a particular geometry (constant micropile sizing, different micropile spacing) installed in the sand with a particular relative density. We only tested the performance of MPRs under the vertical load being applied either at the centroid of four micropiles or on top of a micropile. However, studying other configurations of loading could be helpful. It must also be pointed out that the said conclusions were arrived at based on 1-g model tests. Considering that micropiles behavior depends heavily on stress, further investigation, especially with a centrifuge machine that provides better conditions (stress-strain relations) may be utilized to verify the aforementioned conclusions.

In terms of numerical modeling, the effects of meshing type and size need more investigation as they might change the results to some extent. Also, in this study, only the effect of one single load was taken into account, while this is helpful, the more practical conditions where there is more than a pointed load are recommended. And finally, one must bear in mind that only instant load-settlement behavior and load-sharing mechanism were calculated in this research. Studying load settlement in the long term may also prove useful.

References

- **Alharthi Yasir Mohammed** Shaft Resistance of Driven Piles in Overconsolidated Cohesionless Soils [Report]. - 2018.
- **Alnuaim, A M, El Naggar M H and El Naggar H El** Performance of micropiled raft in clay subjected to vertical concentrated load: centrifuge modeling [Journal] // NRC research press. - 2014.
- **Amornfa Kamol, Quang Ha T and Tuan Tran V** 3D Numerical Analysis of Piled Raft Foundation for Ho Chi Minh City Subsoil Conditions [Book]. - [s.l.] : Geomechanics and Engineering, 2022.
- ASTM D3080 / D3080M-11 [Book Section] // Standard Test Method for Direct Shear Test of Soils Under Consolidated Drained Conditions. - [s.l.] : West Conshohocken, 2011.
- ASTM D422-63(2007)e2 [Book Section] // Standard Test Method for Particle-Size Analysis of Soils (Withdrawn 2016). - [s.l.] : West Conshohocken, 2007.
- ASTM D4253-16 [Book Section] // Standard Test Methods for Maximum Index Density and Unit Weight of Soils Using a Vibratory Table. - [s.l.] : West Conshohocken, 2016.
- ASTM D4254-16 [Book Section] // Standard Test Methods for Minimum Index Density and Unit Weight of Soils and Calculation of Relative Density,. - [s.l.] : West Conshohocken, 2016.
- **Ateş Bayram and Şadoglu Erol** Experimental and Numerical Investigation for Vertical Stress increments of Model Piled Raft Foundation in Sandy Soil [Journal]. - Shiraz : [s.n.], 2021.
- **Briaud J L and Jean Jean** Load Settlement Curve Method for Spread Footings on Sand. Vertical and Horizontal [Journal]. - [s.l.] : ASCE. - Vol. 2. - pp. 37-41.
- **Brown P T and Wiesner R J** The behavior of uniformly loaded piled strip footings [Journal] // Soils and Foundations. - 1975.
- **Brown P.T.** Numerical Analyses of Uniformly Loaded Circular Rafts on Deep [Journal]. - [s.l.] : Géotechnique,, 1969. - Vol. 19.
- **Bruce D A and Juran I** [Book Section] // Drilled and Grouted Micropiles, State-of-Practice Review. - 1997.
- **Bruce D A, DiMillio A F and Juran I** Introduction to Micropiles: An International Perspective [Journal] // Geotechnical Special Publication. - 1995. - pp. 1-26.
- **Burland J. B.** Piles as Settlement Reducers. [Journal] // Proceedings of 19th National Italian Geotechnical Conference.. - [s.l.] : Italian Congress on Soil Mechanics, 1995. - pp. 21-34.
- **Chen W F and Baladi Gilbert** Soil Plasticity theory and Implementation [Book]. - [s.l.] : Elsevier Science, 1985. - 1.
- **Clancy P and Randolph M F** Simple design tools for piled raft foundations [Book]. - [s.l.] : Geotechnique, 1996.
- **Davis E H [et al.]** The analysis of Pile Raft System [Journal] // Geomechanics Journal. - 1972.
- **Deka Ripunjoy** A Review on Different Approaches of Piled Raft Analysis [Article]. - 2014.
- **Di Camillo Fabrizio** Effects of Stress History of Sand on the Shaft Resistance of Large Displacement Piles [Report]. - 2014.
- **FHWA** Micropile Design and Construction Guidelines [Journal]. - [s.l.] : National Highway Institute, 2005.
- **Fioravante Vincenzo and Giretti Daniela** Contact versus noncontact piled raft foundations [Journal] // Canadian Geotechnical Journal. - 2010. - 11 : Vol. 47. - pp. 1271-1287.
- **Fleming Ken [et al.]** Piling Engineering [Book]. - [s.l.] : CRC Press, 2014.
- **Gogoi Nihar, Bordoloi Sanandam and Sharma3 Binu** A Model Study of Micropile Group Efficiency under Axial Loading Condition [Journal]. - Guwahati : Research India Publications , 2014.
- **Griffiths D V, Clancy P and Randolph M F** Piled raft foundation analysis by finite elements [Journal]. - 1991.
- **Gupta Sharat Chandra** Raft Foundations Design and Anlysis with a practical approach [Book]. - New Delhi : Thomas, 1997.

- **Hain S J and Lee I K** The analysis of flexible raft-pile systems [Journal] // Geotechnique. - 1978. - 1 : Vol. 28. - pp. 65-83.
- **Han Jie and Ye Shu Lin** A field study on the behavior of a foundation underpinned by micropiles [Journal] // Canadian Geotechnical Journal. - 2006. - 1 : Vol. 43. - pp. 30-42.
- **Hanna A M and Nguyen T Q** An axisymmetric model for of ultimate capacity of a single pile in sand [Journal] // Japanese Geotechnical Society. - 2002. - Vol. 42. - pp. 47-58.
- **Hanna Adel and Nguyen T Q** Shaft Resistance of Single Vertical and Batter Piles Driven in Sand [Book]. - [s.l.] : ASCE, 2001.
- **Hemsley J. A.** Design application of raft foundation [Book]. - [s.l.] : Thomas Telford, 1999.
- **Horikoshi K and Randolph M F** A Contribution to Optimum Design of Piled Rafts [Article]. - [s.l.] : Géotechnique,, 1988. - 48.
- **Hwang T H, Kim H J and Shin J H** Ground Failure Mechanism of Micoropiled-raft [Journal] // The World congress on Advances in Civil, Enviromental, and Materials Research (ACEM16). - Korea : [s.n.], 2016.
- **Katzenbach R, Arslan U and Moormann** Piled Raft Foundation Projects in Germany. [Article]. - 2000.
- **Kim Dongho [et al.]** Assessment of load sharing behavior for micropiled rafts installed with inclined condition [Journal]. - [s.l.] : Elsevier, 2018.
- **Knappett J A and Craig R F** Craig's Soil Mechanics [Book]. - London : Spon Press, 2012. - 8.
- **Kyung Doohyun [et al.]** Vertical load-carrying behavior and design models for micropiles considering foundation configuration conditions [Journal]. - [s.l.] : NRC research press, 2016. - J.54.
- **Lee K M and Xiao Z R** A simplified nonlinear approach for pile group settlement analysis in multilayered soils [Journal]. - [s.l.] : NRC Research Press, 2001. - 5 : Vol. 38.
- **Lei GH [et al.]** Vertical stress under vertical pressure by extended Mindlin's equation [Journal] // Japanese Geotechnical Society Special Publication. - 2016. - 36 : Vol. 2. - p. 1315.
- **Lizzi F.** The Static Restoration of Monuments: Basic Criteria-Case Histories, Strengthening of Buildings Damaged by Earthquakes [Book]. - Genova : Sagep, 1982.
- PLAXIS 3D 2021 Reference Manual. [Article]. - Delft : Plaxis, 2021.
- **Poulos H G** An Approximate Numerical Analysis Of File-raft Interaction [Journal] // International Journal for Numerical and Analytical Methods in Geomechanics. - 1994. - 2 : Vol. 18. - pp. 73-92.
- **Poulos H G** Analysis of piled strip foundations [Journal] // Proceedings of the 7th International Conference on Computer Methods and Advances in Geomechanics. - Australia : [s.n.], 1991. - pp. 183-191.
- **Poulos H G** Methods of analysis of piled raft foundations [Journal] // A Report Prepared on Behalf of Technical Committee TC18 on Piled Foundations, International Society of Soil Mechanics and Geotechnical Engineering. - 2001.
- **Poulos H G** Pile Foundation analysis and design [Book]. - New york : Wiley, 1980.
- **Poulos H G** Practical Design Procedures for Piled Raft Foundations in Germany [Article]. - London : [s.n.].
- **Poulos H. G.** Piled raft foundations: Design and applications [Journal]. - 2000.
- **Randolph M. F.** Design methods for pile groups and piled rafts [Journal]. - 1994.
- **Rao N. S. V. Kameswara** FOUNDATION DESIGN THEORY AND PRACTICE [Book]. - [s.l.] : John Wiley & Sons, 2011.
- **Reul Randolph and Rnadolph Mark F** Design Strategies for Piled Rafts Subjected to Nonuniform Vertical Loading [Journal] // Journal of Geotechnical and Geoenvironmental Engineering,. - 2002. - 1 : Vol. 130.
- **Ripunjoy Deka** A Review on Different Approaches of Piled Raft Analysis [Article]. - 2014.
- **Russo G** Numerical analysis of piled rafts [Journal] // International Journal for Numerical and Analytical Methods in Geomechanics . - 1998. - Vol. 22. - pp. 477-493.
- **Sanctis Luca de [et al.]** Some remarks on the optimum design of piled rafts [Book Section] // Deep Foundations 2002. - [s.l.] : ASCE, 2002.
- **Sinha Anup and Hanna A M** 3D Numerical Model for Piled Raft Foundation [Article].
- **Sinha J** Analysis of piles and piled rafts in swelling and shrinking soils. // PhD Thesis. - Australia : Univ. of

Sydney, 1996.

- **Small John C** Practical solutions to soil-structure interaction problems [Journal] // Progress in Structural Engineering and Materials. - Sydney : John Wiley & Sons, 2001. - 3 : Vol. 3. - pp. 305-314.
- **Sulaiman Rafi M, aimi Al-Ne and Hussain Mohammed S** Numerical Modelling and Parametric Study of Piled Rafts Foundations [Book]. - [s.l.] : Arabian Journal of Geosciences, 2021.
- **Ta L D and Small J C** ANALYSIS OF PILED RAFT SYSTEMS IN LAYERED SOIL [Journal] // International Journal for Numerical and Analytical Methods in Geomechanics. - [s.l.] : John Wiley & Sons, Ltd, 1996. - 1 : Vol. 20. - pp. 57-72.
- **Terzaghi K, Peck R and Mesri G** Soil Mechanics in Engineering Practice. [Article]. - New York : Wiley-Interscience., 1996.
- **Tharwat Baban M** Shallow foundations (discussion and problem solving) [Book]. - [s.l.] : Wiley Blackwell, 2016.
- **Wood David Muid** [Book Section] // Geotechnical modelling. - 2004.